Title
Rhodium Catalysts in the Oxidation of CO by O2 and NO: Shape, Composition, and Hot Electron Generation

Author
Renzas, James Russell

Publication Date
2010

Peer reviewed|Thesis/dissertation

Rhodium Catalysts in the Oxidation of CO by O_2 and NO: Shape, Composition, and Hot Electron Generation

by

James Russell Renzas

A dissertation submitted in partial satisfaction of the

Requirements for the degree of

Doctor of Philosophy

in

Chemistry

in the

Graduate Division

of the

University of California, Berkeley

Committee in charge:

Professor Gabor A. Somorjai, Chair
Professor Stephen R. Leone
Professor Jeffrey Bokor

Spring 2010

Rhodium Catalysts in the Oxidation of CO by O_2 and NO: Shape, Composition, and Hot Electron Generation

by

J. R. Renzas

Abstract

Rhodium Catalysts in the Oxidation of CO by O_2 and NO: Shape, Composition, and Hot Electron Generation

by

James Russell Renzas

Doctor of Philosophy in Chemistry

University of California, Berkeley

Professor Gabor A. Somorjai, Chair
Professor Stephen R. Leone
Professor Jeffrey Bokor

It is well known that the activity, selectivity, and deactivation behavior of heterogeneous catalysts are strongly affected by a wide variety of parameters, including but not limited to nanoparticle size, shape, composition, support, pretreatment conditions, oxidation state, and electronic state. Enormous effort has been expended in an attempt to understand the role of these factors on catalytic behavior, but much still remains to be discovered. In this work, we have focused on deepening the present understanding of the role of nanoparticle shape, nanoparticle composition, and hot electrons on heterogeneous catalysis in the oxidation of carbon monoxide by molecular oxygen and nitric oxide. These reactions were chosen because they are important for environmental applications, such as in the catalytic converter, and because there is a wide range of experimental and theoretical insight from previous single crystal work as well as experimental data on nanoparticles obtained using new state-of-the-art techniques that aid greatly in the interpretation of results on complex nanoparticle systems.

In particular, the studies presented in this work involve three types of samples: ~ 6.5 nm Rh nanoparticles of different shapes, ~ 15 nm $Rh_{1-x}Pd_x$ core-shell bimetallic polyhedra nanoparticles, and Rh ultra-thin film (~ 5 nm) catalytic nanodiodes. The colloidal nanoparticle samples were synthesized using a co-reduction of metal salts in alcohol and supported on silicon wafers using the Langmuir-Blodgett technique. This synthetic strategy enables tremendous control of nanoparticle size, shape, and composition. Nanoparticle shape was controlled through the use of different organic polymer capping layers. Bimetallic core-shell nanoparticles were synthesized by careful choice of metal salt precursors. Rh/TiO_x and Rh/GaN catalytic nanodiodes were fabricated using a variety of thin film device fabrication techniques, including reactive DC magnetron sputtering, electron beam evaporation, and rapid thermal annealing. The combination of these techniques enabled control of catalytic nanodiode morphology, geometry, and electrical properties.

The prepared nanocatalysts and nanodiodes were characterized with a wide variety of modern techniques before and after reaction in order to investigate catalyst size, shape, composition, lattice structure, and electrical properties. In particular, the catalysts were investigated using Scanning Electron Microscopy to determine coverage and morphology, Transmission Electron Microscopy to determine size, shape, and morphology, X-Ray Photoelectron Spectroscopy to determine elemental composition and oxidation state, X-Ray Diffraction to determine crystallinity and lattice parameters, and Current-Voltage analysis to determine nanodiode barrier height and electrical properties. The use of this broad array of analytical techniques enabled thorough understanding of the catalysts and the role their properties play in catalysis.

The catalytic behavior of the catalysts was measured in CO oxidation by O_2 and by NO *in-situ* using Gas Chromatography and, for the catalytic nanodiodes, chemicurrent analysis. Both techniques were performed using the same ultra-high vacuum chamber. Kinetic data gathered using these techniques was analyzed and compared to the body of literature on related catalysts in order to further the understanding of the role of particular catalyst parameters and properties on their behavior during reaction.

Nanoparticle shape dependence in the oxidation of CO by NO was studied on Rhodium nanocubes and nanopolyhedra from 230 - 270°C. The nanoparticles were characterized using Scanning Electron Microscopy, Transmission Electron Microscopy, and X-Ray Diffraction. At 8 Torr of NO and 8 Torr of CO, the nanocubes were found to have increased turnover frequency and decreased activation energy relative to the nanopolyhedra catalysts. The nanopolyhedra were found to behave similarly to Rh (111) single crystal catalysts, whereas the nanocubes were found to have behavior intermediate to that found on Rh (111) and Rh (100) single crystal catalysts.

Bimetallic 15 nm Pd-core Rh-shell $Rh_{1-x}Pd_x$ nanoparticle catalysts with overall compositions of Rh, $Rh_{0.8}Pd_{0.2}$, $Rh_{0.6}Pd_{0.4}$, $Rh_{0.4}Pd_{0.6}$, $Rh_{0.2}Pd_{0.8}$, and Pd were synthesized and supported on p-type Silicon wafers using the Langmuir-Blodgett technique. The nanoparticle catalysts were characterized using Scanning Electron Microscopy, Transmission Electron Microscopy, X-Ray Diffraction, and X-Ray Photoelectron Spectroscopy. In the reaction of 40 Torr CO with 100 Torr O_2, the bimetallic core-shell catalysts were found to exhibit enhanced activity relative to monometallic Rh and Pd nanoparticle catalysts of the same size. This synergetic effect was analyzed in light of the data from characterization, previous work performed by our group (including the present author) using Ambient-Pressure X-Ray Photoelectron Spectroscopy to study the oxidation and surface segregation behavior of identical bimetallic core-shell nanoparticles *in-situ* during reaction at pressures on the order of hundreds of milliTorr, and previous work on related systems. The observed synergy is postulated to be the result of preferential adsorption of CO on Pd surface sites and preferential dissociative adsorption and oxide-formation by O_2 on Rh surface sites during reaction.

Identical bimetallic 15 nm Pd-core Rh-shell $Rh_{1-x}Pd_x$ nanoparticle catalysts were also synthesized, characterized, and studied in the reaction of CO with NO. Due to the increased complexity of the reaction of CO with NO relative to the reaction of CO with O_2, this reaction was studied in a variety of relative pressure conditions, ranging from 8 Torr NO and 8 Torr CO to 120 Torr NO and 8 Torr CO. In equal pressures of NO and CO, the catalysts were found to have no synergetic enhancement of activity. At these conditions, activity scaled roughly linearly with the relative composition of Rh. At relatively high pressures of NO, however, the catalysts demonstrated very different behavior. Initially, the bimetallic catalysts demonstrated extremely high activity relative to monometallic catalysts in the same conditions. Using results from

Ambient-Pressure X-Ray Photoelectron spectroscopy at similar relative pressures of NO and CO, as well as data from related systems, this synergy was deduced to be caused by preferential adsorption of CO on available metallic Pd surface sites on the core-shell catalyst. After many hours of oxidation in these conditions, however, the bimetallic catalysts were found to deactivate such that, as in the case of equal pressures of CO and NO, product formation scaled linearly with Rh molar fraction. This deactivation may be caused by eventual migration of N adatoms onto Pd sites.

In the final study presented in this work, ultra-thin film 5 nm Rh/TiO_x and Rh/GaN catalytic metal-semiconductor Schottky nanodiodes were studied in the reaction of NO with CO and the reaction of CO with O_2. These devices were fabricated using a combination of reactive sputtering, electron beam evaporation, and rapid thermal annealing and characterized using a variety of techniques, including current-voltage analysis for the determination of Schottky barrier height. Barrier heights on the TiO_x-based nanodiodes were found to be very sensitive to local gas composition, whereas barrier heights on GaN-based devices were found to be more stable. The kinetic behavior of the devices was measured using both gas chromatography and chemicurrent analysis. Hot electron chemicurrent was determined through comparison of the measured current in reaction and the measured thermoelectric current at similar barrier height conditions. Similar activation energies were found using both techniques. This indicates that there is a direct correlation between hot electron production and catalytic activity.

For my wife, Becky, and my mother, Ellen.

Table of Contents

List of Figures and Tables

Chapter 1

Chapter 2

Chapter 3

Chapter 4

Chapter 5

Chapter 6

Chapter 7

Chapter 8

Acknowledgements

This work would not be possible without the help of my adviser, Professor Gabor Somorjai. Professor Somorjai provided a positive environment and excellent research group with tremendous resources and gave me room to grow and explore as I learned an entirely new field. He has challenged me when I needed to be challenged and encouraged me when I needed positive reinforcement. Professor Somorjai has been the best adviser a young graduate student could hope to have and I am deeply indebted to him for all of his help.

I would also like to thank my colleagues and the staff at the University of California, Berkeley, and at Lawrence Berkeley National Laboratory. In particular, I would like to thank Eric Granlund and his staff at the machine shop for their help building many of the apparatuses used in my work, Lynn Keithlin for help with academic matters, and Inger Coble for elegantly navigating the waters between the UC system and Lawrence Berkeley National Laboratory. I would also like to thank Xiaofan Meng and the UC Berkeley Microlab for helping with reactive sputtering of TiO_x, Selim Alayaglu for teaching me nanoparticle synthesis, Wenyu Huang for helping with SEM, Katie Bratlie for originally suggesting NO/CO, and George Holinga, Chris Kliewer, Cesar Aliaga, Leonid Belau, Antoine Hervier, Sergey Maximoff, and soon-to-be Professor Frank Tsung for each being an integral part of the exchange of knowledge and ideas that is so integral to the graduate school experience.

Anthony Contreras always has a smile on his face and a joke on his tongue and I thank him for both that and for training me as a beginning graduate student. Yawen Zhang came up with the nanoparticle syntheses described here, taught me the Langmuir-Blodgett Technique, and also treated me to the very best Peking Duck in all of China when I visited him in November 2009. I appreciate both his genius and his humor. Yimin Li has also been very positive and helpful in lending his theoretical perspective to experimental problems. Feng Tao has been a good friend and a great person to work with – he led the Ambient Pressure XPS work and is always in his office for a late night or weekend chat about data analysis, future experiments, the history of China, and anything else that might come up. I have tremendous respect for everything he has done in his life and I am confident that he will make an excellent professor someday soon.

Above all others, however, I must thank Derek Butcher, Michael Grass, and Zhi Liu. I may well have spent more time with Derek since August 2005 than with my own wife. Derek and I started together in the Somorjai Group, along with Chris Kliewer, and have shared much in that time, including ideas, expertise, UHV parts, samples, beamtime, lunch, an office, birthday parties, and a keen interest in professional football. Derek is a brilliant young man, always reading, learning, questioning, and pushing. Derek does not believe in easy answers or half-measures and plays a mean devil's advocate when a new idea needs testing. He is a remarkable individual and I owe him deep thanks. Michael Grass and Zhi Liu have also been instrumental to my completion of this work. Both were and remain mentors. I deeply value my professional and personal relationships with them as well as their selflessness and encouragement.

Many people outside of Berkeley have also contributed to this work. Most importantly, I would like to thank my immediate family: Mom, Dad, Brooke, Erin, Jenny, Calvin the Dog, Biggie the Boxer, and my wife Becky. My extended family has also been very supportive - especially the Palellas, Diane Dietzler, Jo-L Hendrickson, Grandpas George and John, and my in-laws: Jimmy, Pam, and Jeremy. Prior to my time at Berkeley, I was strongly influenced by Professor Sigurd Wagner at Princeton University, Professor Richard Van Duyne at Northwestern

University, and Peter Bogucki, the Dean of Engineering at Princeton University, each of whom played a key role in my original decision to pursue graduate education and is deserving of my appreciation. I would also like to thank the members of West Bay Rhythm and the Cal Alumni Big Band, who have provided my most regular window into the world outside of graduate school, especially Sam Lind, Paul Seibel, Mark Heckman, Lee Cahalan, and Scott Hayes. My time in graduate school has been challenging, stimulating, and unlike anything I have ever experienced before and I am grateful to all of those who played a part in it.

This work was supported by the Director, Office of Science, Office of Basic Energy Sciences, of the U.S. Department of Energy under Contract No. DE-AC02-05CH11231.

Chapter 1. Introduction

Catalysis is defined as a process in which the basic rate of a chemical reaction is increased by the presence of a material or chemical species, the catalyst, which is not produced or consumed during the course of the reaction. In homogeneous catalysis, the catalyst is of the same phase as the reactants and products. This leads to difficulties, however, in separating the catalyst from the products, which can be prohibitively expensive in some cases. When the catalyst is of a different phase than the reactants or products, the process is known as heterogeneous catalysis. Heterogeneous catalysts work by providing a substrate for the reaction to take place on. This substrate serves to confine reactants to the catalyst such that the reactants can diffuse across the surface and easily encounter each other so that reaction may occur readily. The substrate also provides an alternate reaction pathway for which the energy required for reaction, the activation energy, is lower than without the substrate. The exact mechanism by which the process occurs is different for each unique combination of reactants and catalyst and can even vary based on the precise geometry and electronic condition of the catalyst. In our research group, we focus on heterogeneous catalysis in which the reactants and products are both in the gas phase and the catalysts are noble metal solids.

1.1. Heterogeneous Catalysis and the Catalytic Converter

The field of heterogeneous catalysis has been an important area of research since the early 1800s, when Döbereiner discovered the use of platinum to catalyze the reaction of H_2 and O_2[1]. In the nearly two-hundred years which have followed, the field has mushroomed into one of extreme importance both industrially and scientifically. Catalysts are so important in the multi-trillion dollar chemical manufacturing industry that it has been estimated that 90% of all processes in use in the United States use catalysts in at least one step[2]. The three primary goals of catalysis research are: increase reaction rates, such that more product can be produced in less time; improve selectivity, such that only the desired product is produced and there is less by-product waste to be disposed of, which is of particular importance in so-called "Green Chemistry"; and decrease deactivation, deactivation being the process by which catalysts are poisoned by unwanted adsorbates or other means such that the catalyst is no longer capable of peak performance.

Perhaps the most well-known application of heterogeneous catalysis is the catalytic converter, which plays a key role in decreasing the level of unwanted emissions of CO, NO_x, and unburned hydrocarbons in the exhaust of more than 700 million automobiles in use today[3]. Catalytic converters are comprised of a high surface area mixed oxide monolith (often incorporating oxides such as CeO_2, ZrO_2, and Al_2O_3) with noble metal catalysts dispersed into the monolith. The noble metals most often include Rh, Pt, and Pd, which are used to perform seven basic reactions listed in Table 1.1. Two of the most important reactions in the catalytic converter are the oxidation of CO by O_2 to produce CO_2 and the oxidation of CO by NO to produce CO_2 and N_2. Rh, in particular, is recognized as critical to efficient reduction of NO[4].

Oxidation	$2\ CO + O_2 \rightarrow 2\ CO_2$ $HC + O_2 \rightarrow CO_2 + H_2O$
Reduction/three-way	$2\ CO + 2\ NO \rightarrow 2\ CO_2 + N_2$ $HC + NO \rightarrow CO_2 + H_2O + N_2$ $2\ H_2 + 2\ NO \rightarrow 2\ H_2O + N_2$
Water Gas Shift	$CO + H_2O \rightarrow CO_2 + H_2$
Steam Reforming	$HC + H_2O \rightarrow CO_2 + H_2$

Table 1.1 The seven basic reactions used in the catalytic converter. Several of these reactions, including all of the hydrocarbon (HC) reactions, are selective or have variable stoichiometry[3].

Although much effort has been directed towards the understanding of the mechanisms and catalytic properties underlying these reactions, recent advances in catalyst design and experimental capabilities, as well as the need to continue to meet ever more stringent regulatory requirements, have prompted continued scientific inquiry into these systems. This thesis is focused on these two reactions and their activities in the context of new novel Rh-based nanoparticle and thin film catalysts.

1.2. Nanoparticle Catalysis

Perhaps the most fundamental observation to the understanding of approaches to modern heterogeneous catalysis is that, in most cases, reactions occur on surfaces. This basic fact implies that a catalyst with a very high surface area per volume will be a more efficient use of material than a large block of the same amount of material which has a very low surface area to volume ratio. Although single crystals have long been and remain important model catalysts for mechanistic studies, their poor surface-to-volume ratio renders them unsuitable for use as practical catalysts. For many years, however, the inability to develop high surface area catalysts with controlled morphology and coverage made the careful study of industrially relevant catalysts very difficult. This so-called "materials gap" between low surface area model catalysts such as single crystals suitable for detailed study and inhomogeneous high surface area catalysts used in industrial processes has been the focus of much effort by Gabor Somorjai and his colleagues, who have led the push to develop, characterize, and study size and shape controlled monodisperse nanocatalysts[5]. These nanocatalysts are small in size (typically 2 ~ 15 nm) and as a result benefit from a very favorable surface-to-volume ratio, much like industrial catalysts.

The high surface-to-volume ratio of nanoparticle model catalysts does not come without the cost of added complexity. Due to the vanishingly small proportion of the catalyst which comes from the bulk, nanoparticles and, in some cases, thin films can have very different behavior in reactions than single crystals. In bulk metals, valence electron energy levels are so

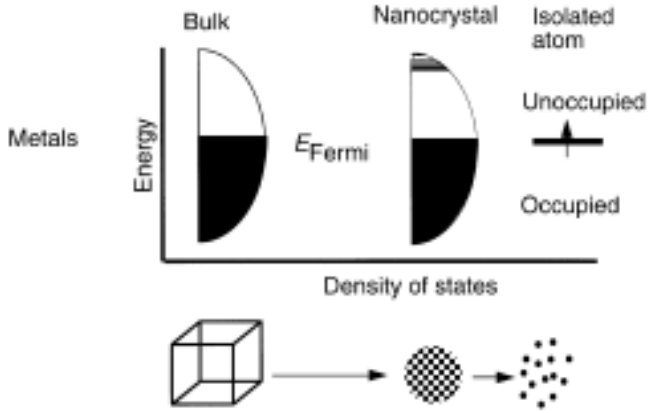

Figure 1.1 Density of states for a metal in bulk form, nanoparticle form, and atomic form. The nanoparticle form is a hybrid between the bulk and atomic states for which *kT* may provide enough energy to overcome electronic energy level spacings at catalytically relevant temperatures[6].

closely spaced as to become effectively continuous. In isolated metal atoms, energy level spacings are discrete, with significant energy gaps between each electronic state. Nanoparticles occupy an intermediate regime, as shown in Figure 1.1. In this intermediate regime, the density of states and the degree to which states are discrete or continuous depends on the precise size of the nanoparticle[6]. When energy, *kT*, is in certain specific regimes, nanoparticles will demonstrate behavior unlike that of either bulk metals or atomic metals. In addition, nanoparticle size can play an important role in determining the geometry of potential adsorption sites. Thus, the binding energy of reactants, the identity of catalytic intermediates and products, and turnover frequency (product molecules per site per second, often abbreviated as TOF) because of the relationship between nanoparticle size and the relative abundance of available surface sites with particular coordination number and geometry (Figure 1.2)[7].

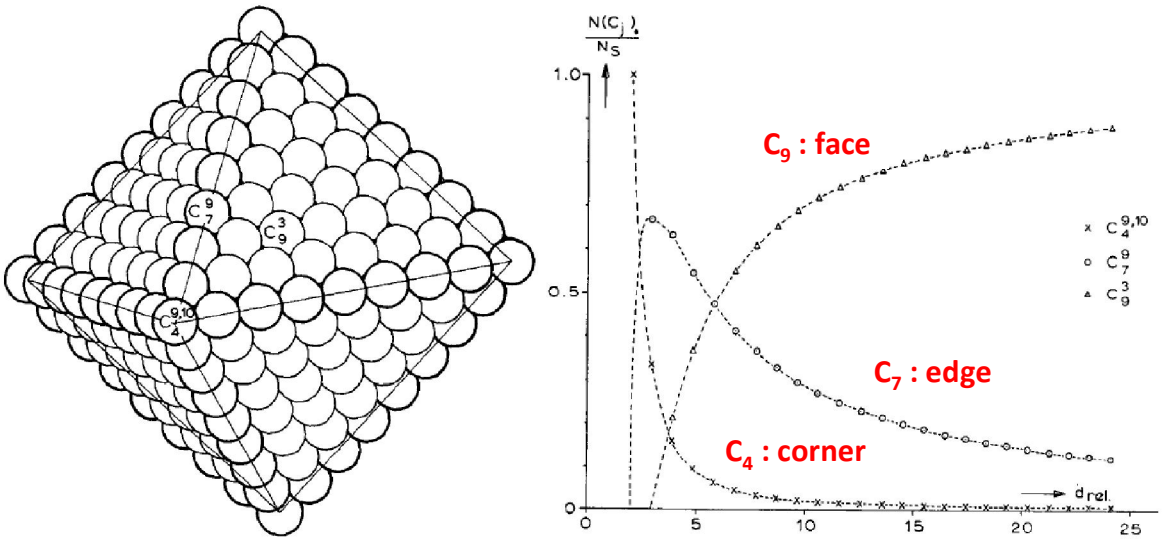

Figure 1.2 Proportion of sites with given coordination number, $N(Cj)/N_s$, as a function of nanoparticle diameter d_{rel} for a f.c.c. octahedron nanoparticle. Adapted from [7].

Another, related, major ramification of the relatively small amount of bulk material present in nanoparticles and thin films is that they tend to oxidize at lower temperatures than bulk metal, as shown for 15 nm bimetallic core-shell $Rh_{0.5}Pd_{0.5}$ nanoparticle catalysts and a bulk bimetallic $Rh_{0.5}Pd_{0.5}$ polycrystalline surface in oxidizing conditions for NO (Figure 1.3) and reducing conditions for CO (Figure 1.4). The effects of reducing the size of a material can lead to significant differences in the catalytic behavior of nanoparticles as compared to bulk materials.

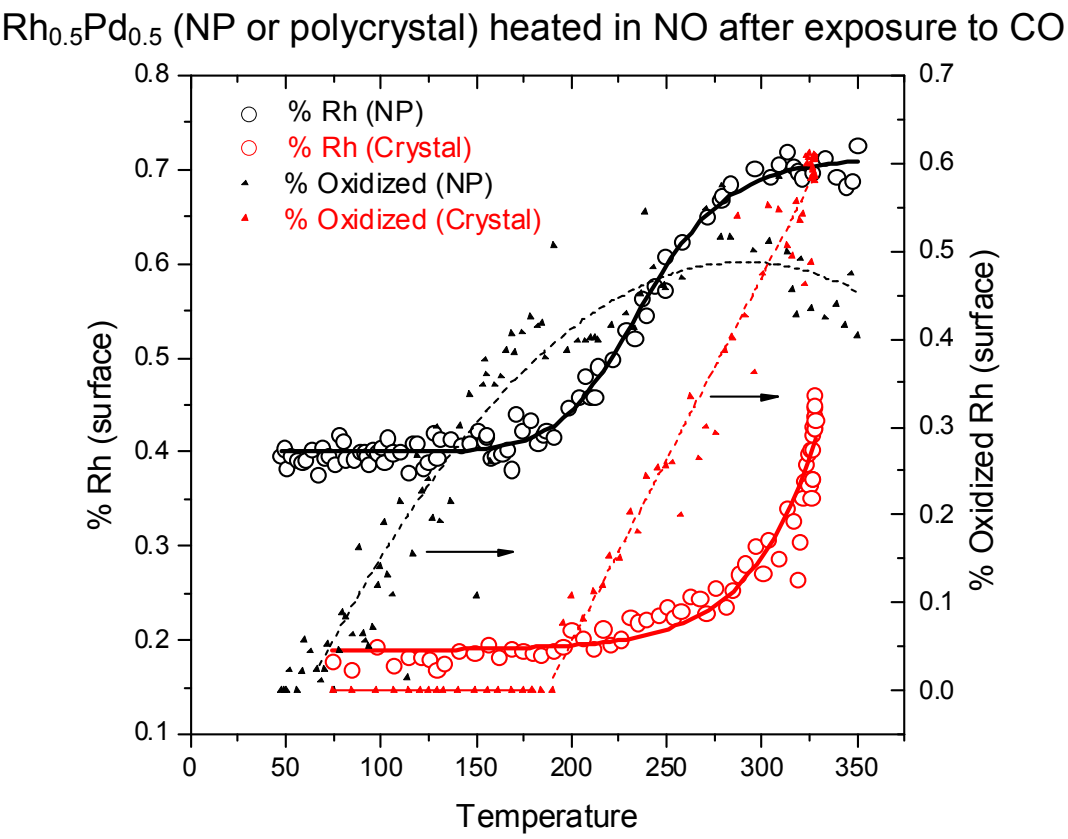

Figure 1.3 Ambient pressure x-ray photoelectron spectroscopy in ~100 mTorr NO on $R_{0.5}Pd_{0.5}$ nanoparticles (NP) and bulk polycrystal showing Rh surface segregation and oxidation versus temperature (in °C). The nanoparticles begin to oxidize at about 50°C, nearly 150°C below the beginning of oxide formation on the polycrystal. The nanoparticles also demonstrate segregation of Rh to the particle surface at lower temperature than is seen in the polycrystal sample. Image courtesy of ME Grass.

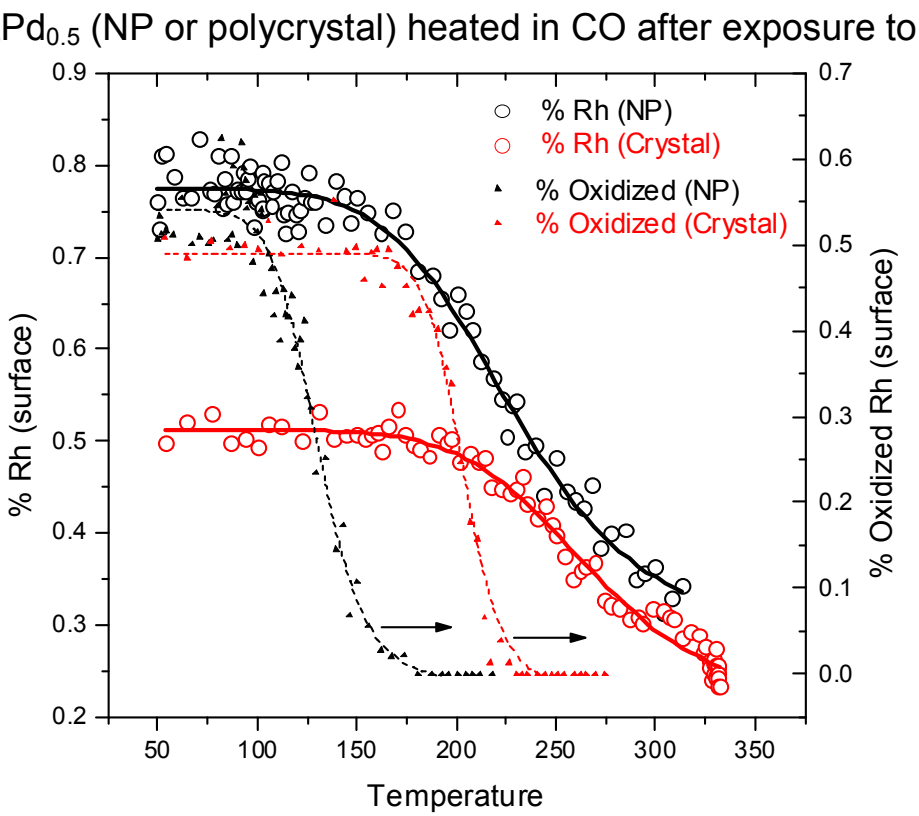

Figure 1.4 Ambient pressure x-ray photoelectron spectroscopy in ~100 mTorr CO on $R_{0.5}Pd_{0.5}$ nanoparticles (NP) and bulk polycrystal showing Rh segregation to the bulk and oxidation state versus temperature (in °C). The nanoparticles begin to reduce at about 100°C, nearly 100°C below the beginning of oxide reduction on the polycrystal. The nanoparticles also demonstrate segregation of Rh to the particle bulk at lower temperature than is seen in the polycrystal sample. Image courtesy of ME Grass.

Much work in the catalytic field has focused on elucidation of the effects of nanoparticle size on catalytic behavior. As early as 1966, Boudart asked fundamental questions about the underlying relationship between particle size and catalysis, such as how catalyst activity is affected by size in the regime between atoms and bulk, whether some minimum bulk-like lattice is required for normal catalytic behavior, and whether an intermediate ideal size exists for which catalyst activity is maximized[8]. The Somorjai Group has studied this issue extensively. For example, one study by our group demonstrated an exponential increase in turnover frequency in CO oxidation on Rh nanoparticles as the nanoparticle size decreased from 7 nm to 2 nm (Figure 1.5)[9]. Our group, including this author, is also currently preparing a manuscript for publication which will demonstrate the opposite trend – an increase in TOF with increasing nanoparticle size – for Ruthenium nanoparticles in similar conditions[10]. This discrepancy in trends for the same reaction on different materials is an indication of the complexity of the effects of nanoparticle size on catalyst activity. Although there is tremendous variation in the relationships between size and

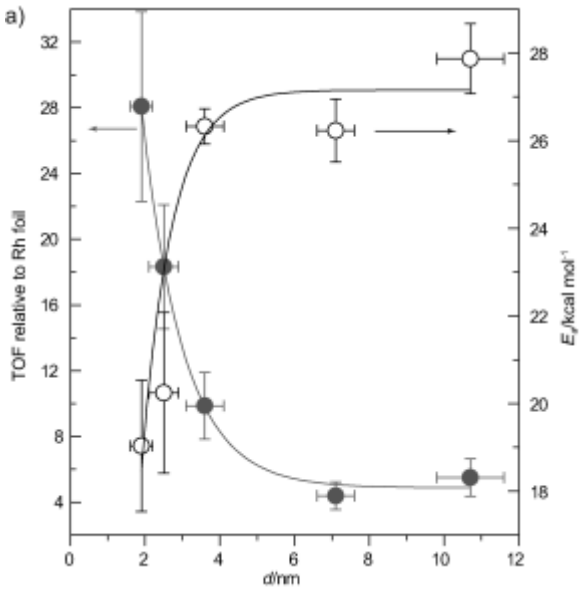

Figure 1.5 Rh nanoparticle size versus turnover frequency (measured at 200°C) and activation energy in 50 Torr O_2 and 20 Torr CO. Activation energy, E_a, decreases and turnover frequency, TOF, increases exponentially as particle size decreases. These exponential trends are consistent with the thermodynamics of oxide stability for nanoparticles as a function of size[9].

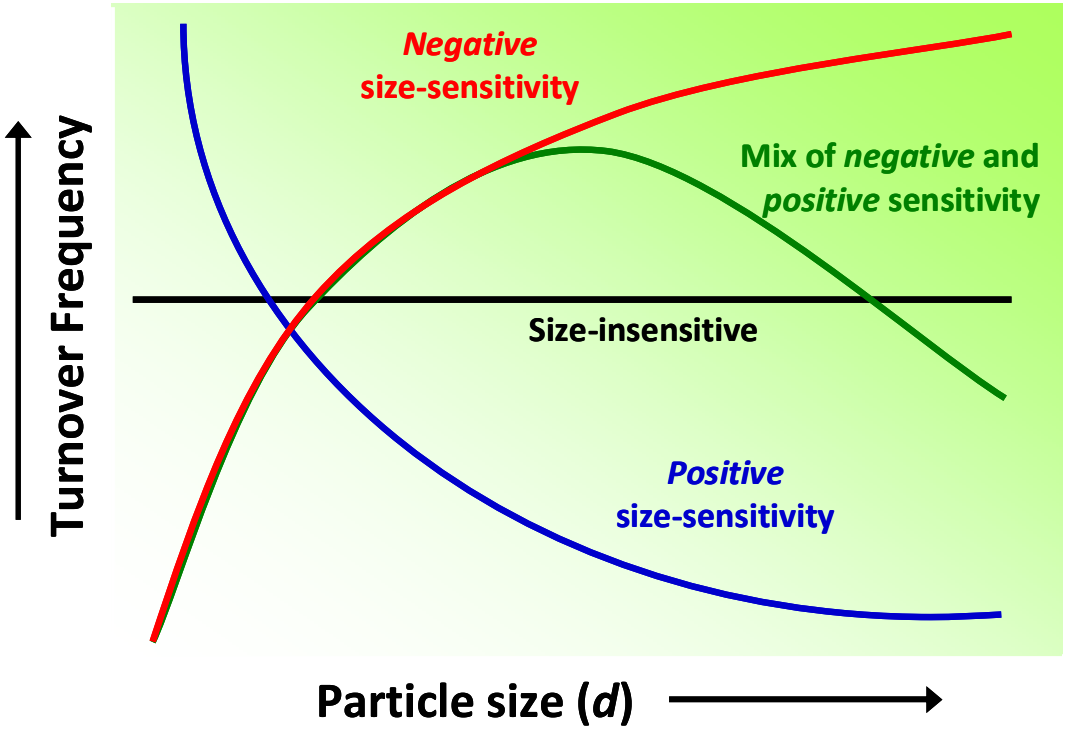

Figure 1.6 There are three major classes of size-sensitivity, which describe the relationships between nanoparticle size and turnover frequency for a given combination of reaction and nanoparticle catalyst. Positive size-sensitivity indicates a decrease in turnover frequency with increasing size, negative size-sensitivity indicates an increase in turnover frequency with increasing size, and mixed size-sensitivity indicates a system with a local minima or maxima in turnover frequency at a particular size. Some catalysts are size-insensitive for particular reactions such that their activity is not affected by the particle size. Image courtesy of SH Joo.

activity depending on the choice of catalyst and choice of reaction, these relationships are often broken into three primary groups: positive size-sensitivity reactions, negative size-sensitivity reactions, and size-insensitive reactions. There is also a fourth category composed of reactions for which a local minima or maxima in activity exists at a particular nanoparticle size (see Figure 1.6)[11]. Positive size-sensitivity reactions are those for which turnover frequency increases with decreasing particle size. The prototypical reaction demonstrating positive size-sensitivity is methane activation. Dissociative bond-cleavage via σ bond activation as the rate limiting step is a common feature in reactions with positive size-sensitivity[12]. Negative size-sensitivity reactions are those for which turnover frequency decreases with decreasing particle size. In this case, formation or dissociation of a π bond is often the rate limiting step. The prototypical reactions for this group are dissociation of CO and N_2 molecules, which each require step-edge sites and contact with multiple atoms. These sites do not always exist on very small nanoparticles, in which step-edges more precisely approximate adatom sites. These reactions also sometimes fall into the fourth category of those with a local maxima in turnover frequency versus particle size because certain particle sizes geometrically favor the formation of these sorts of sites[12]. The third type of reaction is the size-insensitive reaction, for which there is no significant dependence of turnover frequency on nanoparticle diameter. The prototypical size-insensitive reaction is hydrocarbon hydrogenation on transition metal catalysts, for which the rate limiting step is complementary associative σ bond formation[12]. Although these effects are often referred to as structure-sensitivity effects, they are referred to as size-sensitivity effects here in order to further distinguish them from another type of structure-sensitivity which is derived from differences in crystal face and which is discussed below.

Aside from considerations of nanoparticle size, a second major area of inquiry is that of the effect of nanoparticle shape on reaction rate, selectivity, and deactivation. This work is derived from the abundance of research done on single crystal surfaces, which has demonstrated what is known as structure sensitivity in catalysis. Experiments on a wide variety of catalysts have determined that the atomic arrangement of atoms on a surface has a significant effect on catalyst behavior[1]. As demonstrated in Figures 1.7 and 1.8, the type of crystal face dramatically

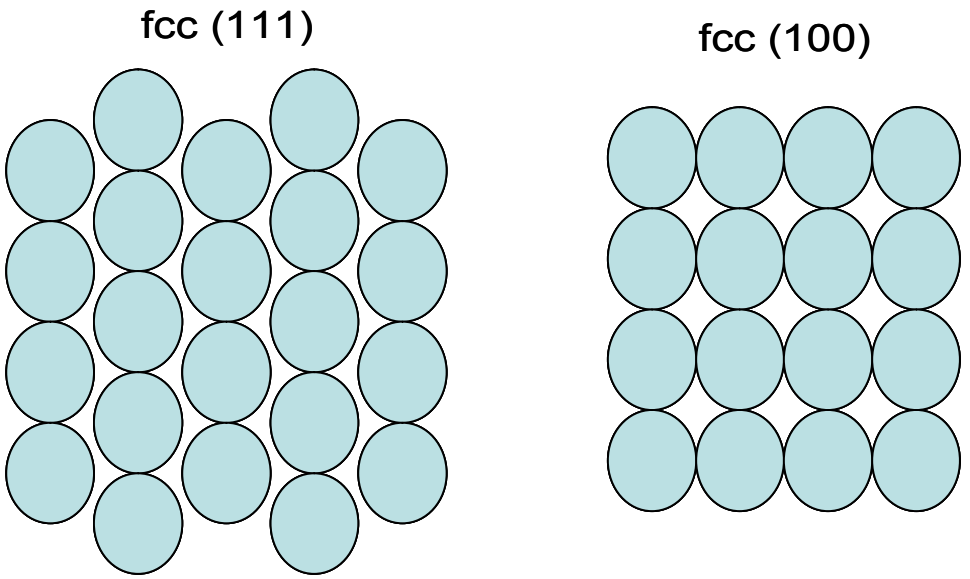

Figure 1.7 Two of the most common fcc crystal faces, (111) (left) and (100) (right).

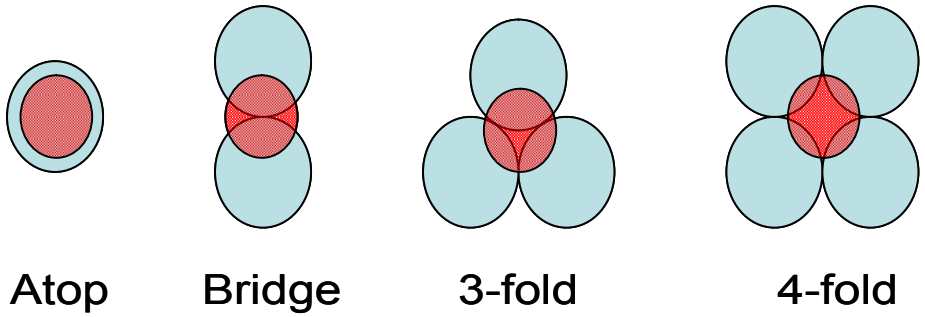

Figure 1.8 Four of the most common adsorption sites found on single crystal terraces.

affects the coordination, number of nearest neighbors, and both two- and three-dimensional geometry of the catalytically active surface atoms. The availability of particular types of adsorption sites can have a large effect on catalysis, as it is common for adsorbates to differ in their affinity for each type of adsorption site. Consequently, the presence or absence of a particular type of site can affect not only reaction rates, but also selectivity. Adsorption can also cause surfaces to reconstruct into different geometries, sometimes to the extent that native surfaces can be broken up into clusters, as is known to happen on *hex*-reconstructed Pt(100) surfaces in the presence of relatively high pressures of CO[13]. The differences in site geometry

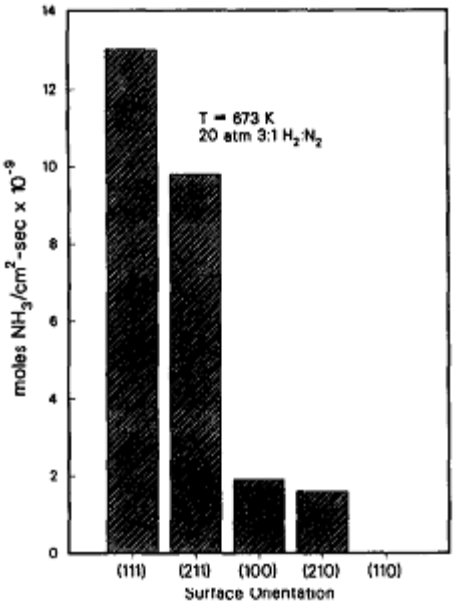

Figure 1.9 The rate of ammonia synthesis on five different Fe single crystal surfaces[14].

and availability can lead to dramatic discrepancies in catalytic activity, as was found on Fe single crystal surfaces for the ammonia synthesis reaction (Figure 1.9)[14]. However, not all reactions are structure sensitive and some reactions are known to be structure sensitive only within a range of specific conditions.

In the case of nanoparticle catalysts, structure-sensitivity is manifested in terms of nanoparticle shape. When little attention is given to shape, most nanoparticles adopt roughly-spherical shapes, often referred to as polyhedra or octahedral, in order to minimize surface energy. These nanoparticles predominately feature (111)-oriented surface atoms, which is the lowest energy crystal face. Under certain conditions, however, nanoparticle catalysts can be synthesized such that the shape, and consequently the surface atom orientation, is kinetically trapped into a non-equilibrium shape, such as a cube, triangle, platelet, or rod[15]. The precise mechanics underlying the synthesis of these shapes are discussed in Section 2.2.1. Nanoparticles of different shape have been shown to have different activity and selectivity in catalytic reactions[16], but have also been shown to melt to a low-energy (111)-oriented roughly-spherical shape at high temperatures and pressures[17]. In spite of their melting behavior, shape-controlled catalysts have been shown to demonstrate structure sensitivity similar to that seen in single-crystal catalysts. For example, a study of Pt nanoparticles in benzene hydrogenation by Bratlie et al. found that (111)-oriented Pt cuboctahedra nanoparticles produce both cyclohexene and cyclohexane, as is also seen in this reaction on Pt (111) single crystals, and that (100)-oriented cubic Pt nanoparticles produce only cyclohexane, as is also the case for Pt (100) single crystal catalysts[18]. This study indicates that shape is a crucial factor in determining and predicting the behavior of real-world industrial nanocatalysts.

Shape-controlled nanoparticles play an important role as model catalysts in furthering the large-scale effort to bridge the "materials gap" between the real-world systems and scientific understanding in catalysis. In Chapter 5 of this work, we discuss kinetic results obtained in the reaction of NO with CO on ~6.5 nm Rh nanoparticles of different shape. We will compare these

results to those obtained on Rh single crystals and other Rh catalysts and discuss insights gained from our analysis.

1.3. Bimetallic Nanoparticle Catalysis

On par with discoveries regarding size and structure effects in catalysis, the development of bimetallic catalysts has been one of the most important innovations in the history of heterogeneous catalysis. In many cases, these materials are known to have significantly different catalytic properties than either parent metal. Although early efforts at understanding the behavior of these systems were focused on modeling the electronic structure of the combined material as a whole, it was determined as early as the 1970s that some degree of independence exists for the individual surface atoms by which catalytic properties can be understood as resulting from a hybrid of the individual behavior of each metal and electronic and geometric effects due to the combination of the two materials[19].

The first well-characterized single crystal bimetallic catalysts with homogeneous surface structure were prepared in the early 1970s[20]. Around this same time period, it was discovered that bimetallic nanoparticles are capable of sustaining phase systems which do not exist in bulk material[3]. The first major breakthrough in this area was Sinfelt's discovery in the 1970s that materials which are completely immiscible in the bulk can be completely miscible and prepared in any relative ratio when the particle or cluster size is small enough[19]. The unique behavior of these systems, in which only one component was typically present at the surface, was described theoretically by Falicov in 1979[21]. Although Sinfelt began using bimetallic particles in ethane hydrogenolysis and cyclohexane dehydrogenation as early as 1973, these experiments were largely carried out in order to help determine whether the particles were, in fact, bimetallic[22].

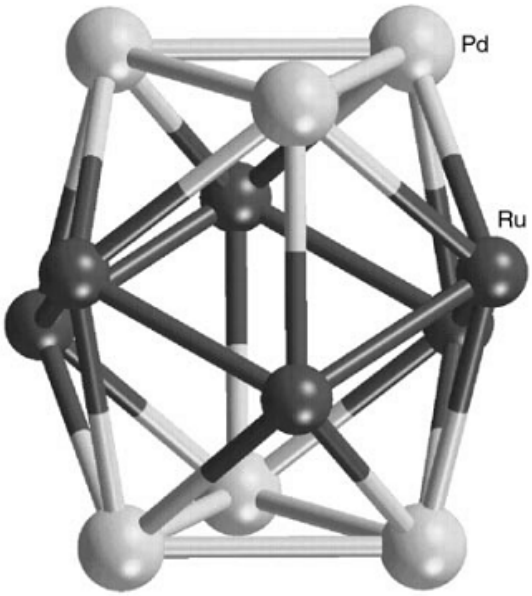

Figure 1.10 Schematic of Pd_6Ru_6 bimetallic cluster catalyst derived from EXAFS analysis[23].

In the more than thirty-five years since Sinfelt's original use of catalysis to confirm bimetallic structure, major advances have been made in synthesis and characterization which have enabled the study of ever-more interesting bimetallic systems. Many of these systems have

now been shown to exhibit "synergy", which is a phenomenon in which the catalyst is, effectively, more than the sum of its parts. In synergetic systems, the activity of the bimetallic nanoparticle towards desired products is greater than the sum of the activities of the two monometallic components. Many examples of this behavior now exist. Examples include Pd_6Ru_6 catalysts characterized with extended x-ray absorption fine structure (EXAFS) and x-ray absorption near edge structure (XANES) that have a ~20-fold enhancement in turnover frequency as compared to the monometallic catalyst constituents in the hydrogenation of Hex-1-ene (Figure 1.10)[23], as well as a Pt_3Ni (111) single crystal surface characterized with low energy electron diffraction (LEED), auger electron spectroscopy (AES), low-energy ion scattering (LEIS), synchrotron-based ultraviolet photoemission spectroscopy (UPS), and surface x-ray scattering (SXS) which was shown to have a 10-fold enhancement over Pt (111) catalysts and a 90-fold enhancement over industrially-relevant Pt/C catalysts in the oxygen reduction reaction (Figure 1.11)[24]. It is worth noting, however, that not all bimetallic catalysts demonstrate synergetic behavior. Some, such as the RhPt system in the oxidation of CO by O_2, simply have reaction rates intermediate to, or in some cases worse than, those of the corresponding monometallic catalysts[25]. It is also worth noting the excellent theoretical work that has been done in this area by Jens Norskov and Thomas Bligaard[26-28].

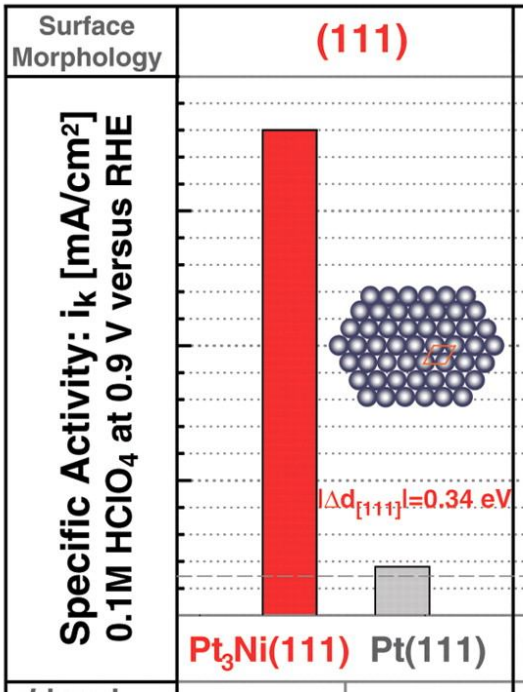

Figure 1.11 The activity of a Pt_3Ni (111) bimetallic catalyst in the oxygen reduction reaction is an order of magnitude greater than the activity of a Pt (111) single crystal in the same reaction. Adapted from [24].

One major complication with most bimetallic catalyst studies, however, is that the individual components are prone to surface segregation at conditions of relatively high temperature and pressure. This type of behavior is known to occur on both single-crystalline[29] and nanoparticle surfaces[30]. This is a problem because many catalytic studies, particularly on single crystals, have been carried out under low pressure conditions because many important analysis techniques, such as AES, LEED, and x-ray photoelectron spectroscopy, require the large mean free path of electrons in vacuum for their basic function. In real catalytic systems, however,

reactants are always kept at high temperature and pressure in order to maximize catalytic efficiency. Although this is a problem in the proper analysis of mono-metallic systems, it is even more important for oxidation reactions, in which various surface and bulk oxide phases may exist at high pressure even though oftentimes only the metallic phase is seen at low pressure[31]. This issue becomes one of profound importance in cases where the very identity, arrangement, and relative concentration of surface elements differs depending on local gas composition and pressure (Figure 1.12). The discrepancy between industrially relevant high pressures and low

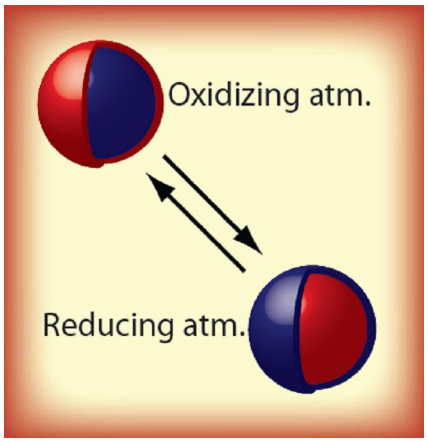

Figure 1.12 Surface segregation behavior in two-component model catalyst system. Image courtesy of F Tao.

pressure systems which are suitable for detailed study is referred to as the "pressure gap". This gap is important because of the entropic contribution to Gibbs Free Energy, $kT \cdot \log P$, which indicates that there is a 0.3 eV difference in energy between low pressure (10^{-8} Torr) and atmospheric conditions (760 Torr)[32]. The energy difference is more than sufficient to alter the behavior of catalyst systems, as demonstrated by the occurrence of Rh surface segregation at pressures of NO above 10 mTorr for $Rh_{0.2}Pd_{0.8}$ Pd-core Rh-shell nanoparticle catalysts (Figure 1.13).

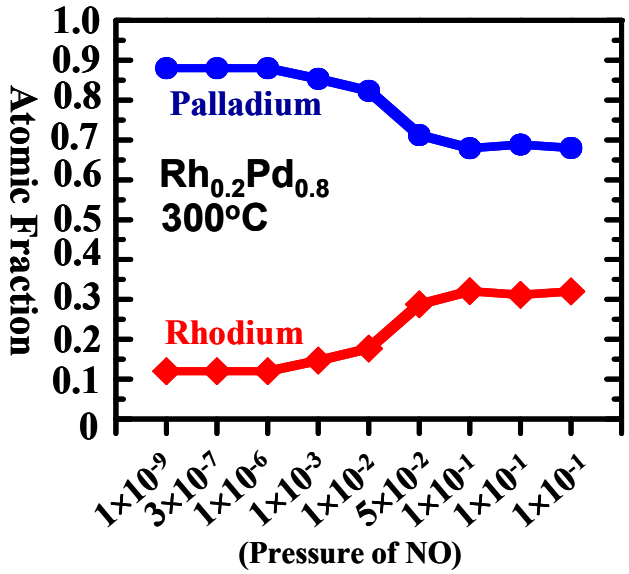

Figure 1.13 Pressure dependence in NO of Rh surface segregation in $Rh_{0.2}Pd_{0.8}$ bimetallic Pd-core Rh-shell nanoparticle catalysts at 300°C

A major step towards resolving the "pressure gap" in heterogeneous catalysis was taken with the recent development of analytical techniques capable of operating at relatively high (hundreds of milliTorr) pressures. At these pressures, the difference in energy drops to less than a tenth of an eV at room temperature, which is less than the thermal energy difference between catalyst systems at room temperature and 300°C. Such a small energy difference can be equalized by heating within a reasonable temperature range. One of these techniques, Ambient Pressure X-Ray Photoelectron Spectroscopy (APXPS), was developed recently at Lawrence Berkeley National Laboratory[32, 33]. This technique uses a nozzle placed very close to the sample (< 1 mm) and a series of differential pumping stages separated by electrostatic lenses in order to enable the sample to remain in locally high pressure yet still enable electrons of relevant kinetic energy (hundreds of eV) to travel successfully into the differentially pumped stages and, eventually, the detector because their mean free path through the gas exceeds the travel distance necessary within the small high pressure cell.

This technique was used by our group, including the present author, recently to study surface segregation and oxidation in Rh-Pd, Pt-Pd, and Rh-Pt bimetallic core-shell nanoparticle systems at relatively high pressures of NO, O_2, CO, H_2, and mixtures thereof[30, 34]. In this study, we clearly demonstrated the relative composition of the core-shell structure of the nanoparticles before (Figure 1.14), during, and after reaction by varying the x-ray photon energy so as to control the kinetic energy of the photoelectrons. Assuming a fixed elemental binding energy and detector work-function, varying the x-ray photon energy directly varies the kinetic energy of emitted photoelectrons. This strategy works because photoelectrons with lower kinetic energy have a lower mean free path through the metal surface layers than photoelectrons with relatively high kinetic energy, which means that the sampling depth can be tuned directly by varying the x-ray photon energy.

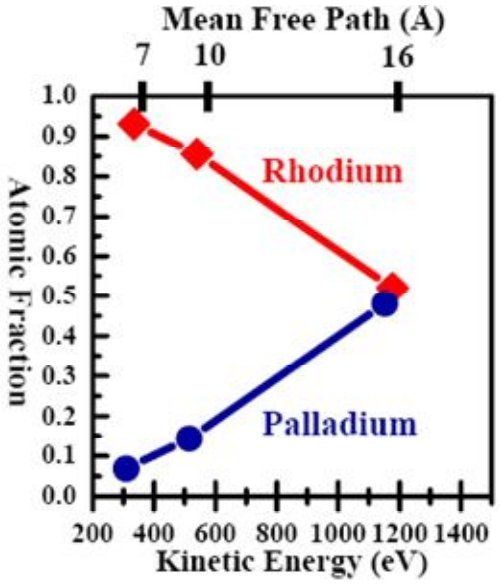

Figure 1.14 Surface composition of $Rh_{0.5}Pd_{0.5}$ Pd-shell Rh-core nanoparticles prior to segregation and oxidation. Varying the incoming x-ray energy enables control over the kinetic energy of electrons at a given binding energy. This means that relative composition can be probed at different depths in the nanoparticle because the electron mean free path is related to kinetic energy[30].

When the RhPd core-shell nanoparticles were treated in different gas compositions, the gas composition dramatically affected the elemental surface composition and the oxidation state of each component. In the RhPd nanoparticles, for example, oxidizing conditions, such as 100 mTorr of NO, caused the Rh component to both oxidize and preferentially segregate to the nanoparticle surface, whereas the Pd component retreated into the bulk but did not undergo significant oxidation. In reducing conditions, including a mixture of 100 mTorr NO and 100 mTorr CO, the Pd component segregated to the surface but again did not oxidize or reduce significantly, while the Rh component was reduced and retreated into the bulk[30]. The behavior of this system is thought to be related to the relative surface energies and oxide formation energies of the components. Pd has a lower surface energy and lower oxide formation energy than Rh. Consequently, in reducing conditions, when both components are metallic, Pd segregates to the surface in order to minimize the overall surface energy. In oxidizing conditions, however, the energy of oxide formation outweighs surface energy considerations and Rh oxide accumulates on the surface and forces Pd into the nanoparticle core.

Although this study overcomes the pressure gap in heterogeneous catalysis, the surface condition of these RhPd core-shell bimetallic nanoparticle catalysts has not previously been correlated to their performance in real catalytic conditions. Real catalytic testing of these nanoparticles is necessary in order to elucidate the role of surface oxidation and segregation in the behavior of core-shell bimetallic catalysts. Chapters 6 and 7 of this work describe the catalytic activity of these particles in the oxidation of CO by O_2 and the oxidation of CO by NO. The activity correlates with the surface properties observed in our APXPS experiments and is compared to previous work on related catalytic systems.

1.4. Hot Electrons and the Catalytic Nanodiode

Another new area in heterogeneous catalysis is the study of the role of hot electrons in catalytic reactions. In this context, hot electrons are electrons in metals excited 1-3 eV above the Fermi level by an adsorption event or other reaction process. Catalytic reactions are well-known to be strongly affected by electronic effects, and the investigation of the role of hot electrons has the potential to lead to significant improvements in the current understanding of catalysis. One of the earliest examples of this type of chemical-to-electrical energy transfer was shown by Kasemo and Walldén in 1974 when they studied Sodium surfaces during Chlorine adsorption[35]. During these experiments, they found that electrons were being ejected from the surface into the vacuum. These exoelectrons had enough energy to overcome the metal work-function because of the large adsorption energy between the electronegative adsorbate and electropositive metal and the low metal work-function. This non-adiabatic phenomenon has also been studied by other groups, both experimentally[36-40] and theoretically[41-43], but was not generally of interest for catalytic metals, such as Pt, Pd, and Rh, because the high work-functions of such metals (generally 4-6 eV) prevented exoelectron emission. Hot electrons are still generated by adsorption processes, but they do not have the necessary energy to escape the bulk of a high work-function metal.

The problem of detecting hot electrons on high work-function metal surfaces was solved by the development of a new method to measure hot electrons emitted into the bulk rather than into the vacuum by Nienhaus and McFarland in 1999[44]. In their work, Nienhaus and McFarland used ultra-thin film Ag/Si and Cu/Si Schottky Diodes to detect hot electrons produced in the metal by the adsorption of atomic hydrogen and atomic deuterium. Using this method, low energy thermally-excited electrons are prevented from traveling across the metal-semiconductor interface by the presence of the Schottky barrier. If the exothermic chemical adsorption event provides enough energy (typically > 1 eV), individual hot electrons can become energetic enough to scatter ballistically through the very thin metal film and cross over into the

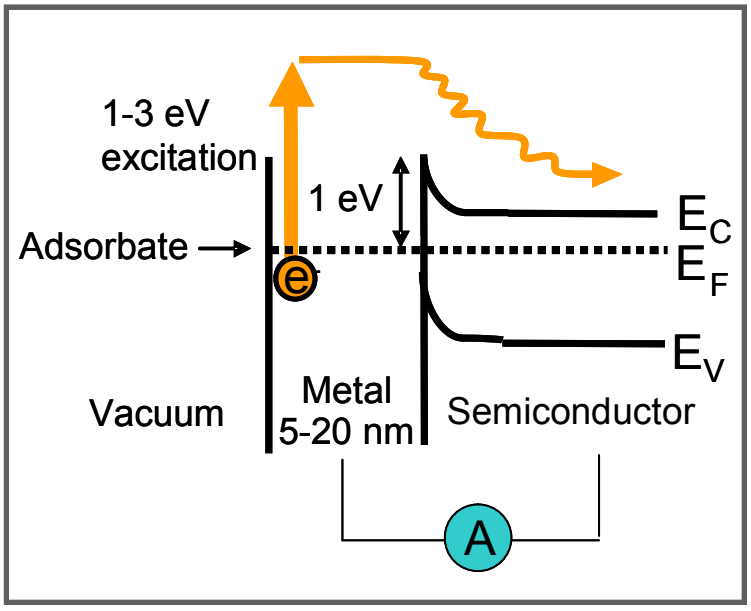

Figure 1.15 Schematic of measurement of adsorbate-induced hot electron excitation. A hot electron is excited to 1-3 eV above the Fermi level by exothermic adsorption onto a metal site, scatters ballistically through 5 – 20 nm metal and over the metal-semiconductor 1 eV Schottky barrier interface, and is measured by a picoammeter before returning to the original metal.

semiconductor, where the electrons relax. The amount of current generated can be measured with an ammeter placed along a circuit leading back to the metal. This method, also shown in Figure 1.15, is expected to work so long as the metal thickness between the reaction site and the Schottky interface is short enough and the hot electron energy is great enough that the hot electron can be transmitted over the Schottky barrier and into the semiconductor. For most exothermic catalytic reactions, hot electrons are expected to have energies in the range of 1-3 eV above the Fermi level, which leads to an inelastic ballistic mean free path of 5-20 nm prior to thermalization into the lattice, depending on the exact choice of metal and electron energy.

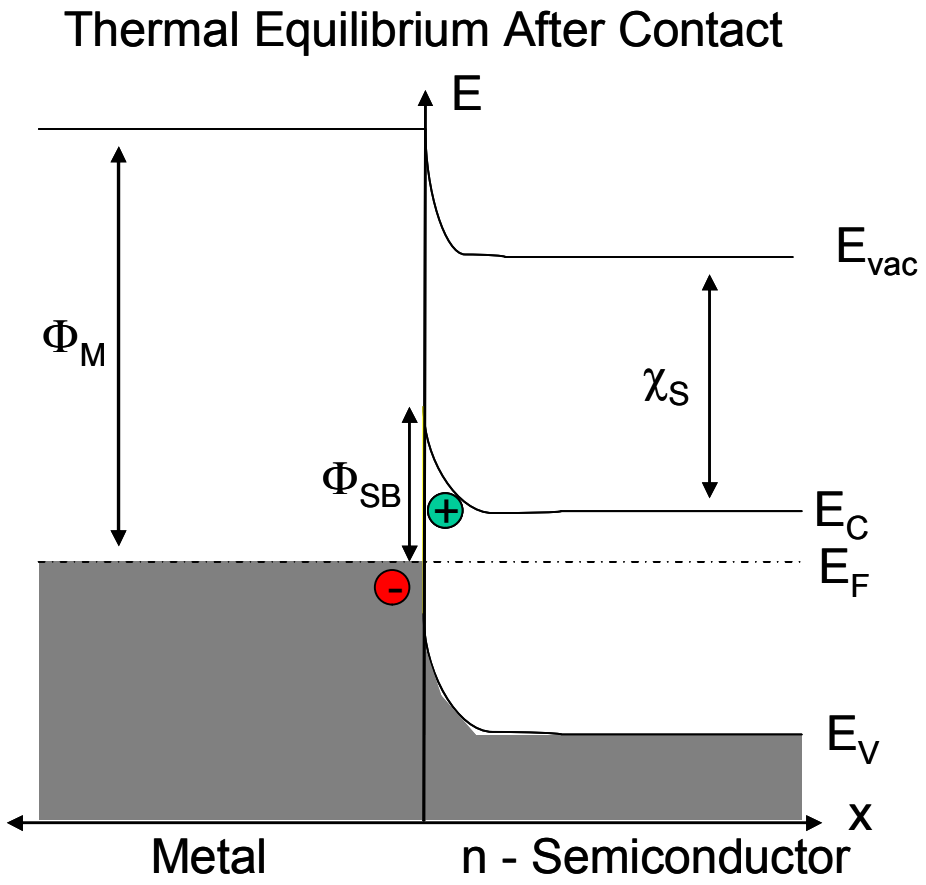

Figure 1.16 Simple band diagram of Schottky barrier formation at a metal-semiconductor interface for an *n*-type (electron-rich) semiconductor. E_{vac} is the vacuum level, E_C is the semiconductor conduction band level, E_F is the Fermi level, which is continuous across the interface, E_V is the semiconductor valence band level. Φ_M, Φ_{SB}, and χ_S are the metal workfunction, Schottky barrier height, and semiconductor electron affinity, respectively.

Schottky diodes, named for Walter Schottky, are devices with a metal-semiconductor interface at which an energy barrier, commonly referred to as a Schottky Barrier, exists that prevents the free flow of low energy electrons through the interface. This barrier, for which the basic band structure is shown in Figure 1.16, arises from the requirement that the Fermi level across an interface remain continuous. The barrier is most often simply described as

(1.1) $$\phi_{Schottky} = \phi_{Metal} - \chi_{Semiconductor}$$ [45]

where $\Phi_{Schottky}$ is the Schottky barrier height, Φ_{Metal} is metal workfunction, and $\chi_{Semiconductor}$ is the electron affinity of the semiconductor[46]. Barrier formation arises from the requirement of Fermi level continuity at the metal-semiconductor interface. When a metal and an *n*-type semiconductor are brought into contact, electrons travel from the semiconductor into the metal because of the lower energy states available in the metal. Eventually, the buildup of negative charge in the metal and positive charge (holes) in the semiconductor causes electrons to begin diffusing back into the semiconductor. In thermal equilibrium, these two sources of electron flow are equivalent and there is no net transport of charge. It is worth noting, however, that although Schottky's elegant description remains the most common seen in conventional publications, the metal-semiconductor interface is in fact much more complex. The interface can be more

accurately described as including a complex interface layer in which a variety of metal-induced gap states, interface-induced gap states, surface states, lateral inhomogeneities, Fermi pinning, and other factors play into the behavior of the metal-semiconductor contact. In many, if not most, cases, the measured Schottky barrier height is heavily influenced by these factors and cannot be accurately predicted by Schottky's original theory. A full treatment of real rectifying metal-semiconductor contacts has been described over the course of several books and full reviews by Winfried Mönch[47-49].

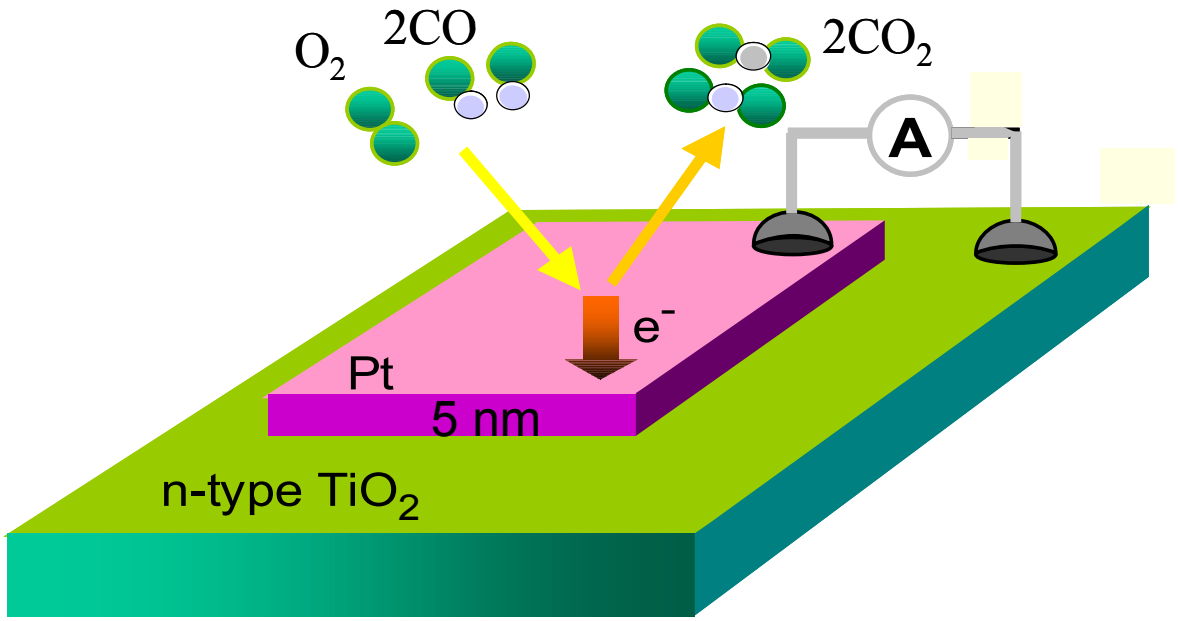

Figure 1.17 Schematic detailing hot electron collection in Pt/TiO_x catalytic nanodiodes in CO oxidation by O_2. Reactants adsorb on the metal surface, react, and desorb. During the reaction event, hot electrons are generated at the reactant-metal interface. These hot electrons travel ballistically through the 5 nm Pt thin film and over the ~1 eV Schottky barrier, and finally scatter and relax in the *n*-type TiO_2 semiconductor. After relaxation, the electrons no longer have enough energy to travel over the Schottky barrier and instead return to the metal through the ammeter, A, where they are measured.

In the Somorjai Group, our research on hot electrons has been aimed primarily at understanding their role in heterogeneous catalysis. The first stage of our work has been focused on understanding how to accurately measure hot electrons *in-situ* during reaction at high temperatures and pressures (~520 K and 1 atm) and how to correlate their presence to real catalytic activity, using the scheme in Figure 1.17. Previously, we have published results detailing the successful measurement of hot electron (> 1 eV) chemicurrent in the oxidation of CO by O_2 using Pt and Pd/TiO_2 catalytic nanodiode devices (Figure 1.20), Pt/GaN catalytic nanodiode devices[50-52], and hybrid nanoparticle-nanodiode devices composed of Pt nanoparticles

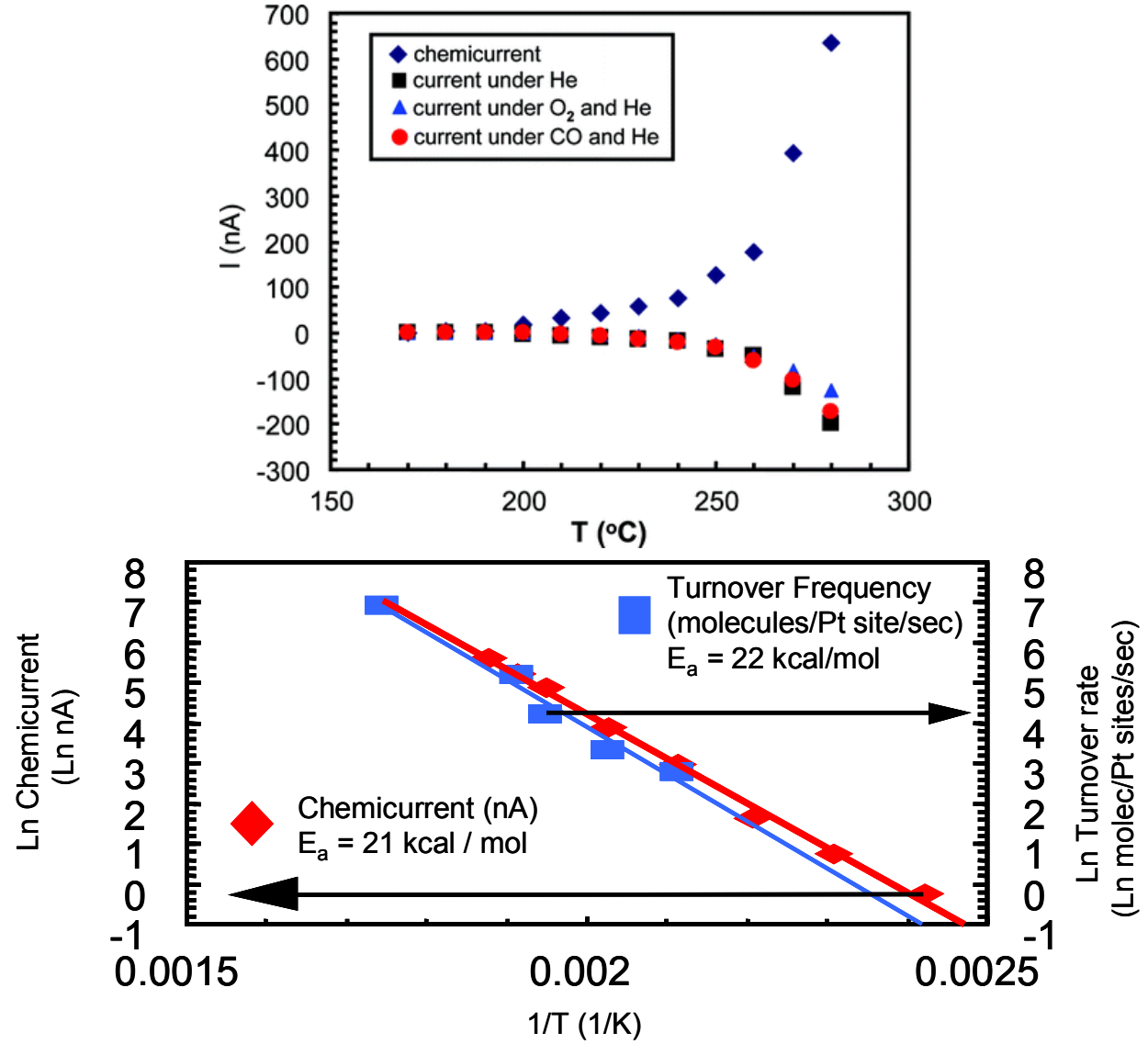

Figure 1.18 Chemicurrent and thermoelectric current as measured on Pt/TiO_x catalytic nanodiode in 40 Torr CO, 100 Torr O_2, and 620 Torr He (top), and an Arrhenius plot comparing chemicurrent and turnover frequency (bottom)[52].

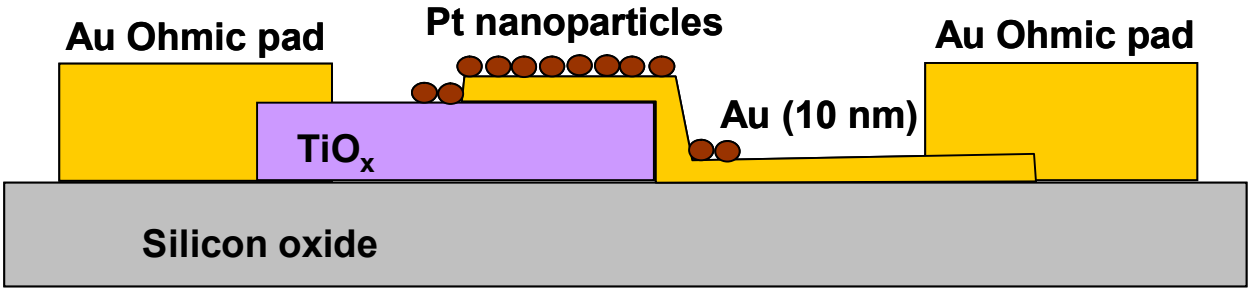

Figure 1.19 Design of Pt nanoparticle on Au/TiO_x catalytic nanodiode. This novel design was used to detect hot electrons generated during reaction on Pt nanoparticles[53].

deposited on an ultra-thin film Au/TiO_2 catalytic nanodiode (Figure 1.19)[53]. We have also succeeded at detecting hot electrons in the hydrogen oxidation reaction using a Pt/TiO_x catalytic nanodiode device kept under a very high partial pressure of oxygen[54]. These experiments found that chemicurrent and turnover frequency are directly related during catalytic reactions on thin-film catalytic nanodiodes. The hot electron yield was found to be on the order of $10^{-4} \sim 10^{-3}$ hot electrons collected per reaction event. We also found that chemicurrent depends exponentially on thin film thickness (Figure 1.20), as expected from mean free path considerations[55].

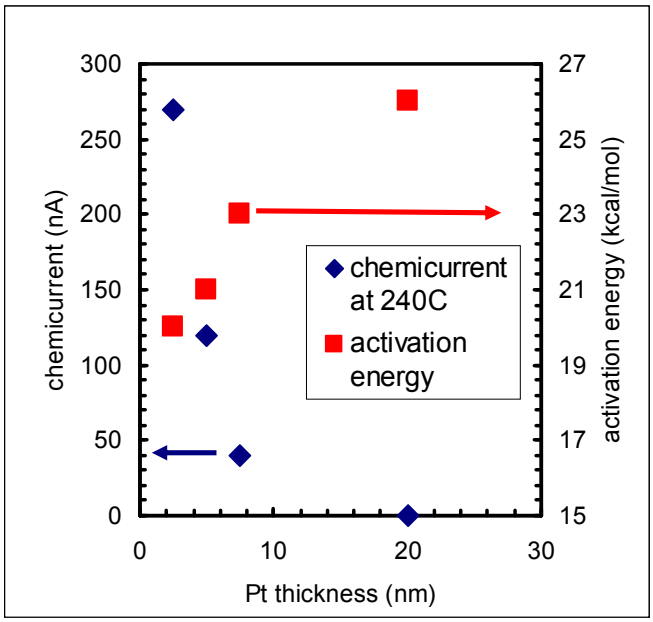

Figure 1.20 Chemicurrent and activation energy versus Pt thin film thickness for Pt/TiO_x catalytic nanodiodes in 40 Torr CO, 100 Torr O_2, and 620 Torr He. Chemicurrent decreases exponentially and activation energy increases with increasing Pt thickness. The exponential decrease in chemicurrent is due to the limited mean free path of hot electrons with energy of 1~3 eV above the Fermi Level and the change in activation energy is due to electronic effects at the surface of a very thin metal film. A similar increase in activation energy was seen on Rh thin films on SiO_2 in the NO/CO reaction when thickness was increased from a discontinuous 0.5 nm to a continuous 8 nm (unpublished results).

Chapter 8 of this text describes experimental results from Rh-based Rh/TiO_x and Rh/GaN catalytic nanodiodes in the reaction of CO with O_2 and the reaction of CO with NO. These results include both the first evidence of hot electron chemicurrent measured on Rh thin films and the first evidence of hot electron excitation from the reaction of CO with NO.

1.5. Summary of Thesis Contents

This thesis is organized into eight chapters, including the present chapter. The work presented will focus on the catalytic properties of novel rhodium-based nanocatalysts, both of the thin film and nanoparticle variety, in the reaction of CO with O_2 and the reaction of CO with NO. Chapter 2 will present the fabrication and synthesis of nanocatalysts. In the first portion of Chapter 2, we will discuss the design and fabrication of ultra-thin film Rh/TiO_x and Rh/GaN catalytic nanodiodes developed to detect and measure hot electron generation in exothermic catalytic reactions. This section will also present some of the tools used to make these devices.

The second half of Chapter 2 describes strategies used to synthesize both shape-controlled Rh nanoparticles and composition-controlled Pd-core Rh-shell bimetallic nanoparticles, as well as the Langmuir-Blodgett Technique, which is used to deposit uniform well-separated sub-monolayer nanoparticle films on a 2D support.

Chapter 3 of this work describes the characterization techniques used to investigate catalyst properties before, after, and sometimes during reaction. These techniques provide information on catalyst coverage, size, shape, crystallinity, lattice parameters, oxidation state, and electrical properties. In Chapter 4, we discuss measurement techniques used to obtain kinetic data in catalysis.

The final four chapters of this thesis are devoted to experimental results. In an effort to improve the focus of this work and also to make room for other material which may not otherwise be published, only one of nine published or upcoming publications to which I have contributed[10, 30, 34, 52-54, 56-58] has been included. The shape-dependence of the reaction of CO and NO on ~6.5 nm Rh nanopolyhedra and nanocubes is discussed in Chapter 5[58]. Chapters 6 and 7 discuss the kinetics of the reactions of CO with O_2 and NO, respectively, on 15 nm Rh-Pd bimetallic core-shell nanoparticles with an emphasis on relating these findings to work which we have previously published in *Science*, but which was carried out at higher pressures than were possible in the published Ambient Pressure X-Ray Photoelectron studies[30]. Chapter 8 describes efforts at detecting hot electrons during the reaction of CO with O_2 and the reaction of CO with NO on Rh/TiO_2 and Rh/GaN catalytic nanodiodes, in which a Schottky barrier is used to screen out reaction-generated hot electrons from low energy thermoelectric electrons.

1.6. References

1. Somorjai, G., *Introduction to Surface Chemistry and Catalysis*. Wiley-Interscience: New York, 1994.
2. Morbidelli, M.; Gavrilidis, A.; Varma, A., *Catalyst Design*. Cambridge University Press: New York, 2001.
3. Kaspar, J.; Fornasiero, P.; Hickey, N., Automotive catalytic converters: current status and some perspectives. *Catalysis Today* **2003,** *77* (4), 419-449.
4. Taylor, K. C., Nitric Oxide Catalysis in Automotive Exhaust Systems. *Catalysis Reviews: Science and Engineering* **1993,** *35* (4), 457 - 481.
5. Somorjai, G. A., The development of molecular surface science and the surface science of catalysis: Berkeley contribution. *J. Phys. Chem. B* **2000,** *104* (14), 2969-2979.
6. Rao, C. N. R.; Kulkarni, G. U.; Thomas, P. J.; Edwards, P. P., Size-dependent chemistry: Properties of nanocrystals. *Chemistry-a European Journal* **2002,** *8* (1), 29-35.
7. Vanharde.R; Hartog, F., STATISTICS OF SURFACE ATOMS AND SURFACE SITES ON METAL CRYSTALS. *Surf. Sci.* **1969,** *15* (2), 189-&.
8. Boudart, M.; Aldag, A.; Benson, J. E.; Doughart.Na; Harkins, C. G., ON SPECIFIC ACTIVITY OF PLATINUM CATALYSTS. *Journal of Catalysis* **1966,** *6* (1), 92-&.
9. Grass, M. E.; Zhang, Y. W.; Butcher, D. R.; Park, J. Y.; Li, Y. M.; Bluhm, H.; Bratlie, K. M.; Zhang, T. F.; Somorjai, G. A., A Reactive Oxide Overlayer on Rhodium Nanoparticles during CO Oxidation and Its Size Dependence Studied by In Situ Ambient-Pressure X-ray Photoelectron Spectroscopy. *Angewandte Chemie-International Edition* **2008,** *47* (46), 8893-8896.

10. Joo, S. H.; Butcher, D. R.; Park, J. Y.; Renzas, J. R.; Grass, M.; Liu, Z.; Aksoy, F.; Mun, B. S.; Salmeron, M.; Somorjai, G., In Preparation.
11. Che, M.; Bennett, C. O., THE INFLUENCE OF PARTICLE-SIZE ON THE CATALYTIC PROPERTIES OF SUPPORTED METALS. *Advances in Catalysis* **1989,** *36*, 55-172.
12. Van Santen, R. A., Complementary Structure Sensitive and Insensitive Catalytic Relationships. *Accounts Chem. Res.* **2009,** *42* (1), 57-66.
13. Tao, F.; Dag, S.; Wang, L. W.; Liu, Z.; Butcher, D. R.; Salmeron, M.; Somorjai, G. A., Restructuring of hex-Pt(100) under CO Gas Environments: Formation of 2-D Nanoclusters. *Nano Lett.* **2009,** *9* (5), 2167-2171.
14. Strongin, D. R.; Carrazza, J.; Bare, S. R.; Somorjai, G. A., THE IMPORTANCE OF C-7 SITES AND SURFACE-ROUGHNESS IN THE AMMONIA-SYNTHESIS REACTION OVER IRON. *Journal of Catalysis* **1987,** *103* (1), 213-215.
15. Tao, A. R.; Habas, S.; Yang, P. D., Shape control of colloidal metal nanocrystals. *Small* **2008,** *4* (3), 310-325.
16. Tsung, C. K.; Kuhn, J. N.; Huang, W. Y.; Aliaga, C.; Hung, L. I.; Somorjai, G. A.; Yang, P. D., Sub-10 nm Platinum Nanocrystals with Size and Shape Control: Catalytic Study for Ethylene and Pyrrole Hydrogenation. *Journal of the American Chemical Society* **2009,** *131* (16), 5816-5822.
17. Wang, Z. L.; Petroski, J. M.; Green, T. C.; El-Sayed, M. A., Shape transformation and surface melting of cubic and tetrahedral platinum nanocrystals. *J. Phys. Chem. B* **1998,** *102* (32), 6145-6151.
18. Bratlie, K. M.; Lee, H.; Komvopoulos, K.; Yang, P. D.; Somorjai, G. A., Platinum nanoparticle shape effects on benzene hydrogenation selectivity. *Nano Lett.* **2007,** *7* (10), 3097-3101.
19. Sinfelt, J. H., HETEROGENEOUS CATALYSIS - SOME RECENT DEVELOPMENTS. *Science* **1977,** *195* (4279), 641-646.
20. Campbell, C. T., BIMETALLIC SURFACE-CHEMISTRY. *Annu. Rev. Phys. Chem.* **1990,** *41*, 775-837.
21. Moranlopez, J. L.; Falicov, L. M., SEGREGATION AND SHORT-RANGE ORDER PROPERTIES AT THE BOUNDARIES OF TWO-DIMENSIONAL BIMETALLIC CLUSTERS. *Surf. Sci.* **1979,** *79* (1), 109-116.
22. Sinfelt, J. H., SUPPORTED BIMETALLIC-CLUSTER CATALYSTS. *Journal of Catalysis* **1973,** *29* (2), 308-315.
23. Raja, R.; Sankar, G.; Hermans, S.; Shephard, D. S.; Bromley, S.; Thomas, J. M.; Johnson, B. F. G., Preparation and characterisation of a highly active bimetallic (Pd-Ru) nanoparticle heterogeneous catalyst. *Chem. Commun.* **1999,** (16), 1571-1572.
24. Stamenkovic, V. R.; Fowler, B.; Mun, B. S.; Wang, G. F.; Ross, P. N.; Lucas, C. A.; Markovic, N. M., Improved oxygen reduction activity on Pt3Ni(111) via increased surface site availability. *Science* **2007,** *315* (5811), 493-497.
25. Park, J. Y.; Zhang, Y.; Grass, M.; Zhang, T.; Somorjai, G. A., Tuning of catalytic CO oxidation by changing composition of Rh-Pt bimetallic nanoparticles. *Nano Lett.* **2008,** *8* (2), 673-677.
26. Studt, F.; Abild-Pedersen, F.; Bligaard, T.; Sorensen, R. Z.; Christensen, C. H.; Norskov, J. K., Identification of non-precious metal alloy catalysts for selective hydrogenation of acetylene. *Science* **2008,** *320* (5881), 1320-1322.

27. Norskov, J. K.; Bligaard, T.; Rossmeisl, J.; Christensen, C. H., Towards the computational design of solid catalysts. *Nat. Chem.* **2009,** *1* (1), 37-46.
28. Sehested, J.; Larsen, K. E.; Kustov, A. L.; Frey, A. M.; Johannessen, T.; Bligaard, T.; Andersson, M. P.; Norskov, J. K.; Christensen, C. H., Discovery of technical methanation catalysts based on computational screening. *Topics in Catalysis* **2007,** *45* (1-4), 9-13.
29. Rodriguez, J. A.; Goodman, D. W., THE NATURE OF THE METAL METAL BOND IN BIMETALLIC SURFACES. *Science* **1992,** *257* (5072), 897-903.
30. Tao, F.; Grass, M. E.; Zhang, Y. W.; Butcher, D. R.; Renzas, J. R.; Liu, Z.; Chung, J. Y.; Mun, B. S.; Salmeron, M.; Somorjai, G. A., Reaction-Driven Restructuring of Rh-Pd and Pt-Pd Core-Shell Nanoparticles. *Science* **2008,** *322* (5903), 932-934.
31. Gustafson, J., Westerstrom, R., Resta, A., Mikkelsen, A., Andersen, J.N., Balmes, O., Torrelles, X., Schmid, M., Varga, P., Hammer, B., Kresse, G., Baddeley, C.J., Lundgren, E., Structure and catalytic reactivity of Rh oxides. *Catalysis Today* **2009**.
32. Salmeron, M.; Schlogl, R., Ambient pressure photoelectron spectroscopy: A new tool for surface science and nanotechnology. *Surface Science Reports* **2008,** *63* (4), 169-199.
33. Ogletree, D. F.; Bluhm, H.; Lebedev, G.; Fadley, C. S.; Hussain, Z.; Salmeron, M., A differentially pumped electrostatic lens system for photoemission studies in the millibar range. *Review of Scientific Instruments* **2002,** *73* (11), 3872-3877.
34. Tao, F.; Grass, M.; Zhang, Y.; Butcher, D. R.; Aloni, S.; Tsung, C. K.; Liu, Z.; Altoe, V.; Renzas, J. R.; Aksoy, F.; Mun, B. S.; Salmeron, M.; Somorjai, G., *In Preparation* **2010**.
35. Kasemo, B.; Walldén, L., Spontaneous emission of photons and electrons during chemisorption of chlorine on sodium. *Solid State Communications* **1974,** *15* (3), 571-574.
36. Delchar, T. A., EXO-ELECTRON EMISSION DURING OXYGEN CHEMISORPTION AT CLEAN NICKEL SURFACES. *J. Appl. Phys.* **1967,** *38* (5), 2403-&.
37. Klar, F.; Bansmann, J.; Glaefeke, H.; Fitting, H. J.; Meiwes-Broer, K. H., Exoelectron emission from magnesium surfaces. *Surf. Sci.* **1999,** *442* (3), 477-484.
38. Bottcher, A.; Grobecker, R.; Greber, T.; Morgante, A.; Ertl, G., EXOELECTRON EMISSION DURING THE OXIDATION OF NA FILMS. *Surf. Sci.* **1993,** *280* (1-2), 170-178.
39. Allen, G. C.; Tucker, P. M.; Hayden, B. E.; Klemperer, D. F., EARLY STAGES IN THE OXIDATION OF MAGNESIUM, ALUMINUM AND MAGNESIUM-ALUMINUM ALLOYS .1. EXOELECTRON EMISSION AND LONG WAVELENGTH PHOTOEMISSION. *Surf. Sci.* **1981,** *102* (1), 207-226.
40. Bottcher, A.; Morgante, A.; Giessel, T.; Greber, T.; Ertl, G., EXOELECTRON EMISSION AT CS SURFACES BY ACCELERATED O(2) MOLECULES. *Chem. Phys. Lett.* **1994,** *231* (1), 119-122.
41. Brako, R.; Newns, D. M., NON-ADIABATIC PROCESSES AT METAL-SURFACES. *Vacuum* **1982,** *32* (1), 39-50.
42. Norskov, J. K., Dynamical aspects of electronic structure during adsorption. *Journal of Vacuum Science and Technology* **1981,** *18* (2), 420-426.
43. Eguiluz, A. G., ELECTRON-HOLE-PAIR DAMPING OF AN EXCITED-STATE OF A MOLECULE ADSORBED ON A METAL-SURFACE. *Physical Review B* **1984,** *30* (8), 4366-4371.
44. Nienhaus, H.; Bergh, H. S.; Gergen, B.; Majumdar, A.; Weinberg, W. H.; McFarland, E. W., Electron-hole pair creation at Ag and Cu surfaces by adsorption of atomic hydrogen and deuterium. *Physical Review Letters* **1999,** *82* (2), 446-449.
45. Schottky, W., Halbleitertheorie der Sperrschicht. *Naturwissenschaften* **1938,** *26*.

46. Sze, S. M., *Physics of Semiconductor Devices*. 2nd ed.; Wiley: New York, 1981.
47. Monch, W. In *Barrier heights of real Schottky contacts explained by metal-induced gap states and lateral inhomogeneities*, Papers from the 26th conference on the physics and chemistry of semiconductor interfaces, San Diego, California (USA), AVS: San Diego, California (USA), 1999; pp 1867-1876.
48. Monch, W., *Electronic Properties of Semiconductor Interfaces*. Springer: Berlin, 2004.
49. Monch, W., *Semiconductor Surfaces and Interfaces*. 3rd ed.; Springer: Berlin, 2001.
50. Ji, X. Z.; Somorjai, G. A., Continuous hot electron generation in Pt/TiO2, Pd/TiO2, and Pt/GaN catalytic nanodiodes from oxidation of carbon monoxide. *J. Phys. Chem. B* **2005,** *109* (47), 22530-22535.
51. Ji, X. Z.; Zuppero, A.; Gidwani, J. M.; Somorjai, G. A., Electron flow generated by gas phase exothermic catalytic reactions using a platinum-gallium nitride nanodiode. *Journal of the American Chemical Society* **2005,** *127* (16), 5792-5793.
52. Park, J. Y.; Renzas, J. R.; Hsu, B. B.; Somorjai, G. A., Interfacial and Chemical Properties of Pt/TiO2, Pd/TiO2, and Pt/GaN Catalytic Nanodiodes Influencing Hot Electron Flow. *The Journal of Physical Chemistry C* **2007,** *111* (42), 15331-15336.
53. Park, J. Y.; Lee, H.; Renzas, J. R.; Zhang, Y. W.; Somorjai, G. A., Probing hot electron flow generated on Pt nanoparticles with Au/TiO2 Schottky diodes during catalytic CO oxidation. *Nano Lett.* **2008,** *8* (8), 2388-2392.
54. Hervier, A.; Renzas, J. R.; Park, J. Y.; Somorjai, G. A., Hydrogen Oxidation-Driven Hot Electron Flow Detected by Catalytic Nanodiodes. *Nano Lett.* **2009,** *9* (11), 3930-3933.
55. Nienhaus, H., Electronic excitations by chemical reactions on metal surfaces. *Surface Science Reports* **2002,** *45* (1-2), 3-78.
56. Park, J. Y.; Aliaga, C.; Renzas, J. R.; Lee, H.; Somorjai, G. A., The Role of Organic Capping Layers of Platinum Nanoparticles in Catalytic Activity of CO Oxidation. *Catalysis Letters* **2009,** *129* (1-2), 1-6.
57. Park, J. Y.; Renzas, J. R.; Contreras, A. M.; Somorjai, G. A., The genesis and importance of oxide-metal interface controlled heterogeneous catalysis; the catalytic nanodiode. *Topics in Catalysis* **2007,** *46* (1-2), 217-222.
58. Renzas, J. R.; Zhang, Y.; Huang, W. Y.; Somorjai, G. A., Rhodium Nanoparticle Shape Dependence in the Reduction of NO by CO. *Catalysis Letters* **2009**.

Chapter 2. Sample Preparation

The samples used for the studies presented here fall into two categories – catalytic nanodiodes fabricated using conventional thin film deposition techniques, and metal nanoparticles synthesized using a combination of metal salts, a reducing solvent, and capping agent. These techniques allowed a great degree of control over sample material, nanoscale morphology, macroscale geometry, and electrical properties.

2.1. Nanodiode Fabrication

Catalytic nanodiodes are metal-semiconductor Schottky diode devices composed of an ultrathin (~5 nm) catalytic metal thin film in contact with a wide-bandgap semiconductor, such as TiO_x or GaN. These diodes are specially designed to separate high-energy hot electrons from low-energy bulk electrons using a Schottky barrier while remaining active for a wide-range of industrially relevant catalytic reactions.

2.1.1. Device Design

Two types of nanodiode devices were used in our work: Rh/TiO_x and Rh/GaN. Early work on the TiO_x-based catalytic nanodiode system used a vertically-oriented device design (Figures 2.1 and 2.2) consisting of a series of separate depositions of Ti, Au, TiO_x, SiN, Pt, and a final Ti/Au layer[1]. This device design suffered from a very low yield as a result of the large number of steps, cross-contamination issues from the use of an electron beam evaporator at a user facility, and difficulty in deposition of a high-quality crystalline TiO_x layer because of challenges associated with reactive electron beam evaporation of this particular material[2]. These difficulties lowered yields to well below 10%.

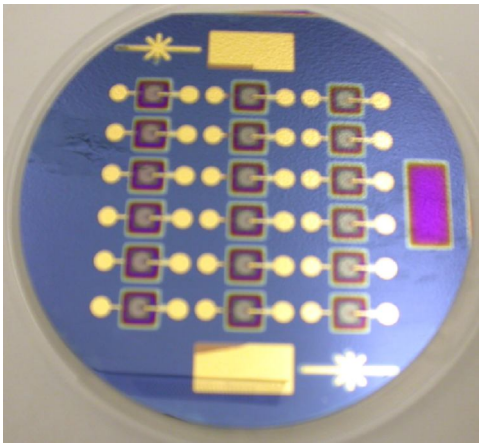

Figure 2.1 Pt/TiO_2 Catalytic Nanodiode Wafer - Original Design

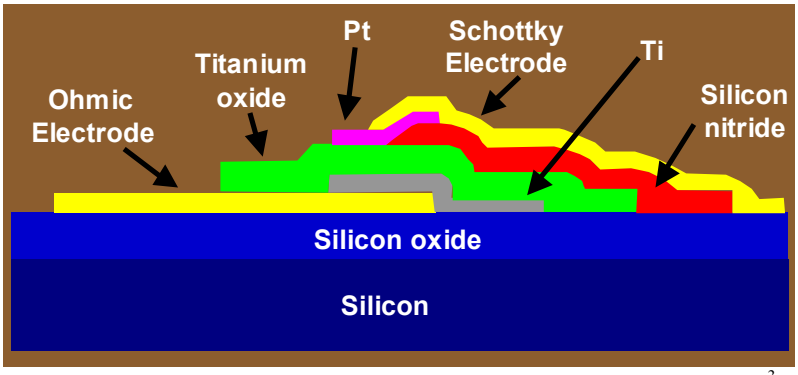

Figure 2.2 Pt/TiO_2 Catalytic Nanodiode Schematic – Original Design[3]

This early design has been substantially improved upon by our work in recent years. Yields have been improved to 95% by decreasing the number of fabrication steps, building a new electron beam evaporator in our lab which does not suffer from cross-contamination issues, and standardizing the TiO_x deposition process through the use of Direct-Current Magnetron Reactive Sputtering and a Rapid Thermal Annealing (RTA) step. Efforts have also been made to understand and account for the interaction of hydrogen with the Pt/TiO_x structure[4]. Studies have also been done using Pt Nanoparticle-Au/TiO_x devices comprised of an Au thin film Schottky contact on TiO_x with Pt nanoparticles deposited on the Au layer[5].

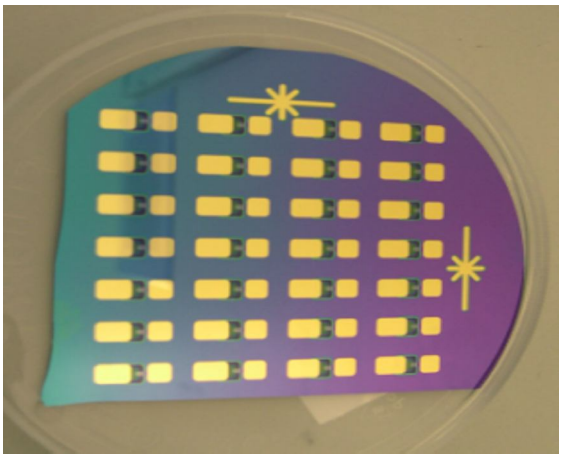

Figure 2.3 Pt/TiO_2 Catalytic Nanodiode Wafer - Improved Design

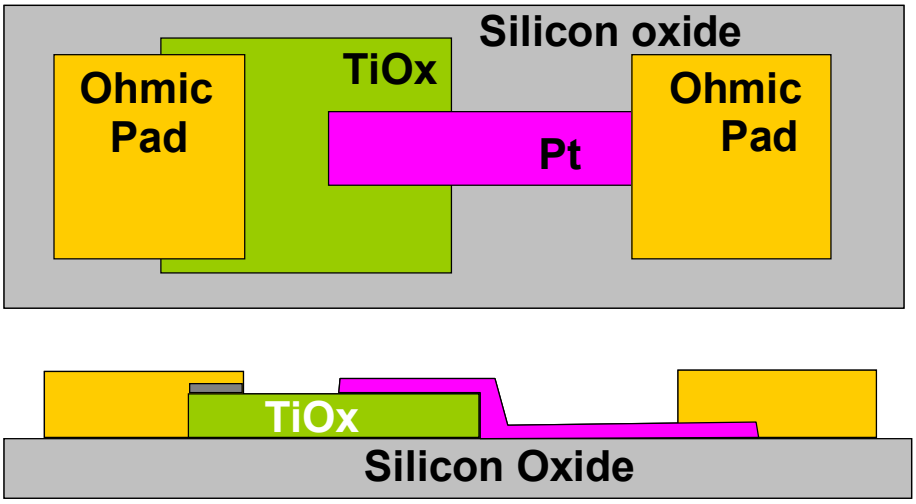

Figure 2.4 Pt/TiO_2 Catalytic Nanodiode Schematic – Improved Design

The Rh/TiO_x devices studied in Chapter 8 were fabricated on 4" p-type Si(100) wafers with a 500 nm thermal oxide layer. Due to the dependence of catalytic turnover number on the availability of metal sites, each device was relatively large in size, measuring approximately 2 cm in length and 0.5 cm in width. First, TiO_x was deposited through an aluminum shadow mask using DC Magnetron Reactive Sputtering. The wafer was then annealed using Rapid Thermal Annealing in order to improve TiO_x oxygen content and crystallinity. Then, two ohmic contacts composed of Ti and Au thin films were deposited with a custom-built electron beam evaporator. Of these ohmic contacts, one covered approximately half of the TiO_x layer and the other was separated from the TiO_x by 1 mm spacing. The final layer was composed of a 5 nm ultra-thin Rh film. A wafer fabricated with this design is shown in Figure 2.3 and the design schematic is shown in Figure 2.4.

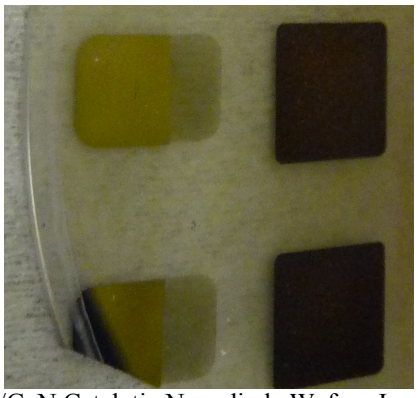

Figure 2.5 Pt/GaN Catalytic Nanodiode Wafer - Improved Design

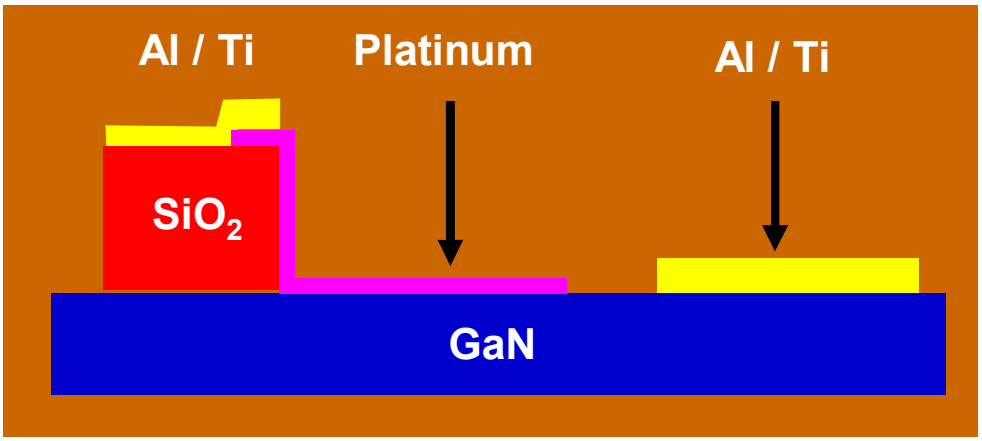

Figure 2.6 Pt/GaN Catalytic Nanodiode Schematic – Improved Design

Rh/GaN devices were also fabricated for use as catalytic hot electron detectors. The initial work on Pt/GaN nanodiodes used devices fabricated by General Electric Global Research[6]. This photolithography-based design has been replaced by a newer design that does not require photolithography and can be fabricated using only electron beam evaporation and RTA. The new design (Figures 2.5 and 2.6) is based on a 2" Si-doped n-type GaN/Sapphire wafer. The sapphire serves as a physical support for the relatively-soft GaN layer. The GaO surface oxide on the GaN was removed using Buffered Oxide Etch. One SiO_2 insulating pad was deposited to support a thick contact pad to make contact to Rh without shorting the device. Ohmic contacts consisted of a Ti/Al structure deposited with electron beam evaporation. The ohmic contacts were annealed using RTA to improve the contact resistance between the metal layers and GaN[7]. The Rh ultra-thin film was deposited last so as to avoid sintering the film during the high temperature RTA process.

2.1.2. DC Magnetron Reactive Sputtering

DC Magnetron Reactive Sputtering is a variant of the commonly used sputtering deposition technique in which the noble gas is replaced by a mixture of noble and reactive gas, such as a mixture of Argon and Oxygen. This technique was used to deposit TiO_x thin films on Si wafers using a Ti target for the sputtering source and an O_2/Ar mixture as the sputtering gas.

Ordinary DC sputtering works by accelerating ionized gas atoms towards a target such that the target atoms are displaced and ejected towards the substrate. The gas is typically ionized with a high voltage, and the choice of gas is made based on mass and reactivity. Noble gases are commonly chosen because they do not readily form chemical bonds to the substrate and target. Gases are typically chosen to have a mass that matches the mass of the target atoms as closely as possible for maximally efficient sputtering. The total gas pressure can be adjusted to determine whether the sputtering process will be dominated by high-energy ballistic events or low-energy thermal sputtering events. The ionized gas atoms are accelerated towards the target material by the use of an electric field placed between the target and substrate. Accelerated ions slam into the target material, displacing the material and ejecting it into the chamber. This ejected vapor deposits on all line-of-sight surfaces in the chamber, including the substrate. The overall process is diagrammed in Figure 2.7.

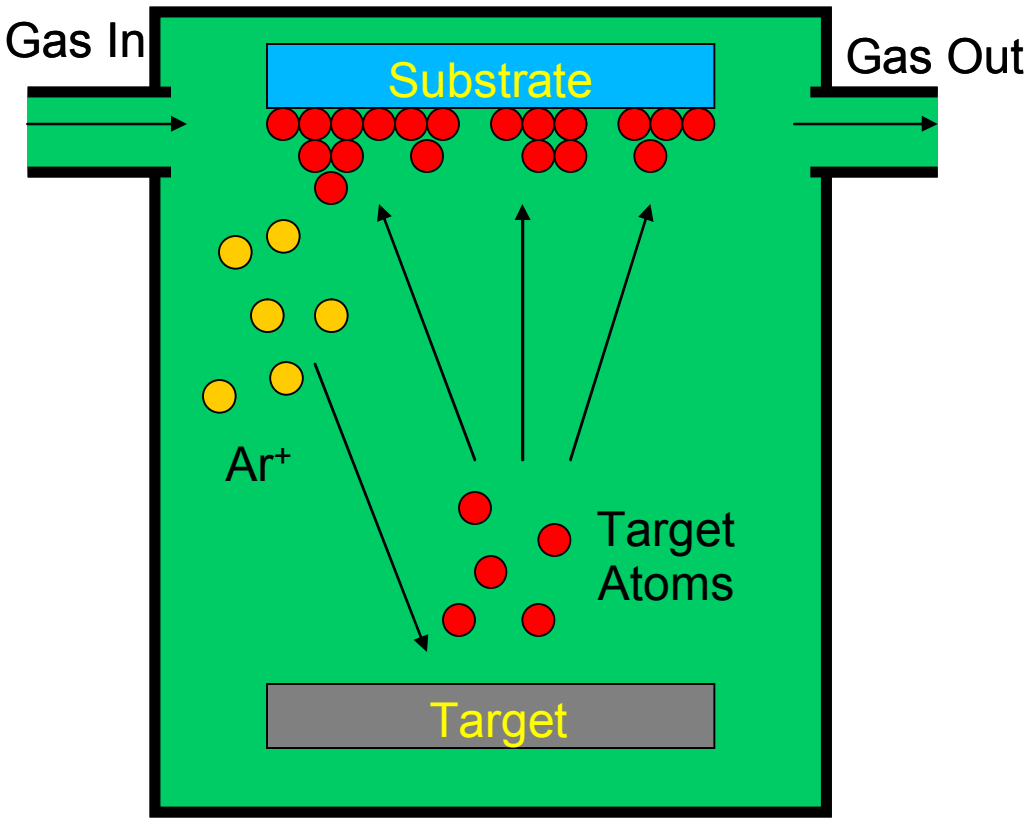

Figure 2.7 Scheme of Direct-Current Sputtering. The Target and Substrate are biased relative to one another. The resulting electric field accelerates Ar^+ towards the Target. These collisions eject atoms from the Target material. The ejected atoms cover all line-of-sight surfaces.

Magnetron sputtering is an upgrade to standard DC sputtering which uses electromagnetic fields to trap stray secondary electrons at the target surface. These electrons undergo further ionization events with the background gas, which leads to a higher density plasma and increases the sputtering rate[8].

Reactive magnetron differs from the process described above only in that the gas is not a noble gas. In order to form TiO_x, a mixture of O_2 and Ar gases was used. The O_2 component of this gas is capable of oxidizing Ti at any stage of the sputtering process – while Ti is part of the target, while Ti is actively traveling between target and substrate, and after Ti has been deposited on the substrate. The tremendously complex interactions involved in reactive sputtering processes have been the subject of intense research efforts in the thin film field[9-11]. The mechanisms determining the morphology of reactively-sputtered TiO_x films has been a sub-field of particular interest[12-16]. In particular, there is a significant difference between the high sputtering rate of the pure target material and the low sputtering rate of the surface after oxidation, which leads to hysteresis in the sputtering rate. The oxide surface is also subject to charging effects, which can greatly influence sputtering behavior and lead to arc formation within the chamber. These difficulties and others have been described particularly well by Musil et al[17]. Despite these challenges, this technique was still preferred for TiO_x deposition because of the higher-quality films produced as compared to those formed using reactive electron beam evaporation[18].

DC Magnetron Reactive Sputtering was performed in the University of California, Berkeley's Microlab facility. Typical parameters were a base pressure of 6×10^{-6} Torr, 37 sccm

Ar (standard cubic centimeters per minute), 11-15 sccm of a 20% O_2/80% Ar gas mixture, total gas pressure of 5 mTorr, 400 W power, and 435 V bias between source and target. Typical TiO_x films had a thickness of about 150 nm, as measured by profilometry, and resistivity of 25 kΩ/square, as measured with four-point probe.

2.1.3. Electron Beam Evaporation

Metals and insulators were deposited on selected areas of the wafer using electron beam evaporation through aluminum shadow masks. Electron beam evaporation is a form of physical vapor deposition which works by focusing electrons on a material until a small spot of material is vaporized. This technique is preferable to thermal evaporation for use with high melting point metals, such as Pt or Rh. It also works well for the deposition of tightly-bound insulating materials like SiO_2 and Al_2O_3, but is not appropriate for poly-atomic materials prone to dissociation, such as TiO_2, which is difficult to evaporate and can decompose to a sub-oxide. Electron beam evaporation is preferable to sputtering for very thin films because thickness measurements can be done *in-situ* using a quartz crystal microbalance without the need for special shielding equipment.

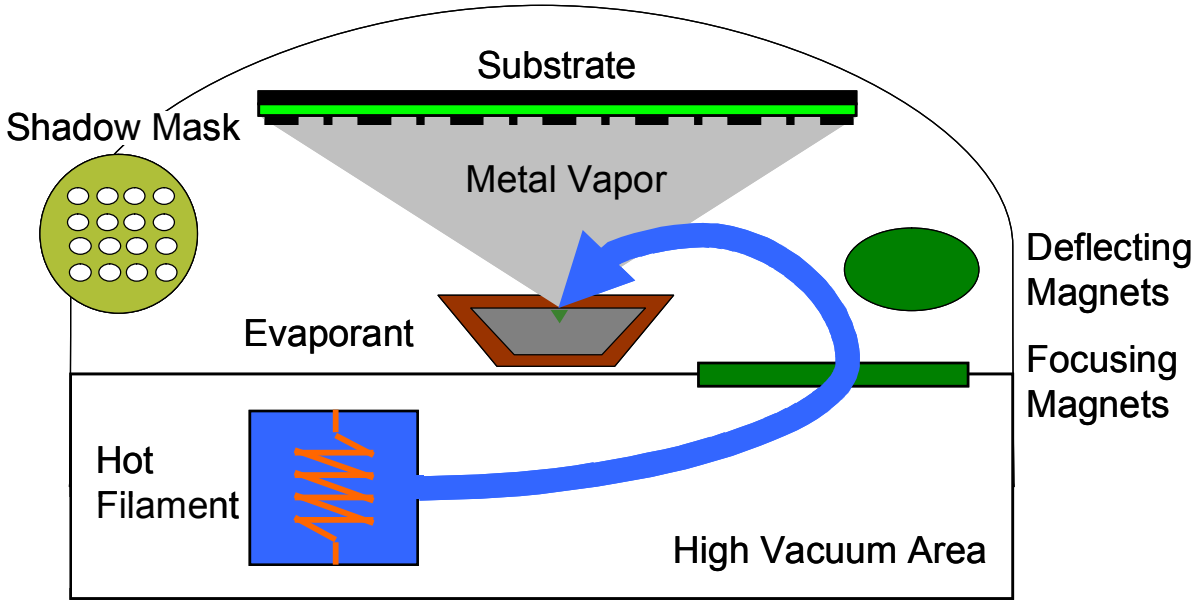

Figure 2.8 Basic Schematic of Electron Beam Evaporation. An Al shadow mask is used to define deposition area.

Deposition was carried out in a system custom built in our lab which uses a turbopump, a water-cooled four crucible rotatable hearth with built-in magnets and filament, a three kW power supply, and a quartz crystal microbalance. Figure 2.8 includes a diagram of the basic process. The pressure prior to deposition was typically 10^{-6} Torr after pumping down for two hours. The distance between the metal source and the target wafer was approximately 0.5 meters. Layer thickness was determined by a quartz crystal microbalance calibrated with multiple characterizations using profilometry and cross-sectional Scanning Electron Microscopy. The relationship describing the uniformity of the layer is given in (2.1) below[19],

(2.1) $$\frac{t_{edge}}{t_{center}} = \frac{1}{\left[1+\left(\frac{r}{h}\right)^2\right]^2}$$

Uniformity of metal layer deposited by Electron Beam Evaporation

where t_{edge} is the film thickness at the edge of the wafer, t_{center} is the film thickness at the center of the wafer, r is the distance from wafer center to wafer edge, and h is the source-target distance. From this relationship, it can be calculated that the maximum thickness variation across a 4" wafer is less than 1 nm for a 50 nm film deposited in this chamber and less than a tenth of a nanometer for a 5 nm film. This was further verified using profilometry.

Electron beam evaporation was carried out using a custom-built evaporator built at Lawrence Berkeley National Laboratory (Figure 2.9).

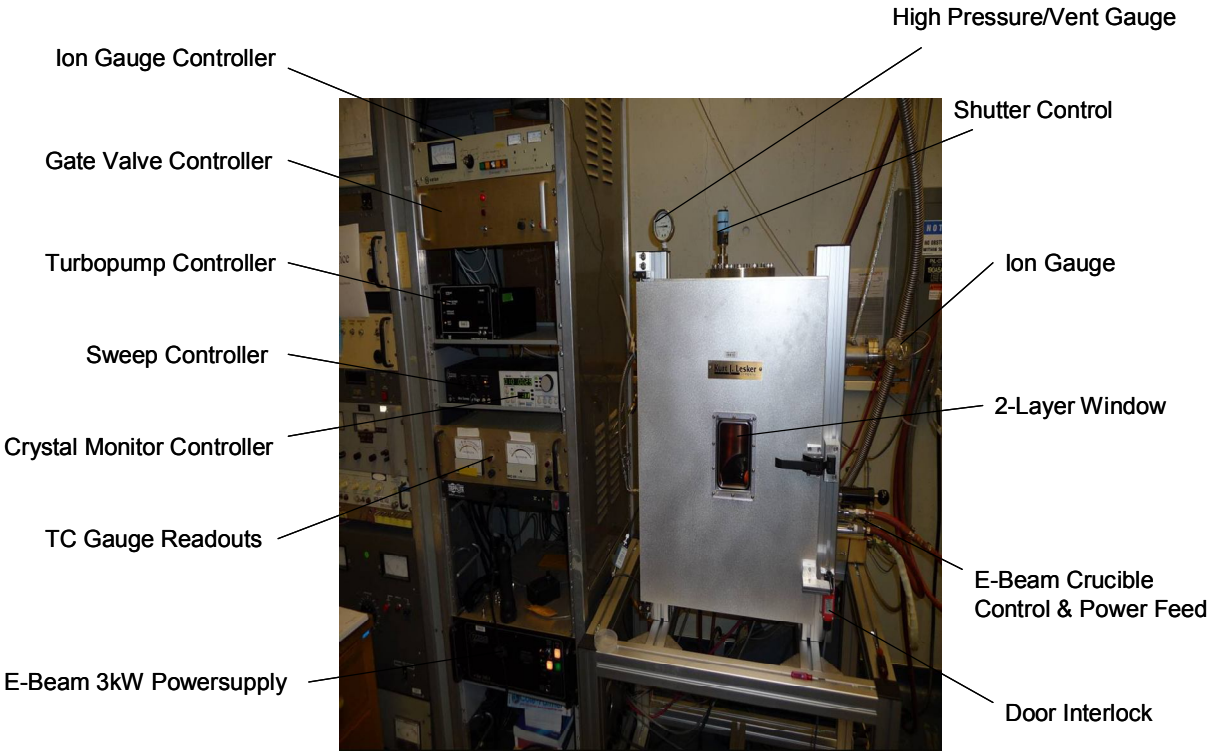

Figure 2.9 Electron Beam Evaporator built for Nanodiode Fabrication. Electron beam evaporation is an excellent tool for metal thin film depositions and can also be used to deposit thin-film insulators and semiconductors.

2.1.4. Rapid Thermal Annealing

Rapid thermal annealing (RTA) is a common semiconductor fabrication technique used to quickly heat a wafer to high temperature in a gas environment in order to alter crystal structure, promote chemical changes such as oxidation within a material, alloy contacts, or reduce stress. By carefully controlling the temperature, anneal time, and gas composition, a wide variety of material structures can be accessed which are not immediately available using only sputtering or evaporation without specialized equipment for *in-situ* heating. Very different RTA steps were

used for TiO_x and GaN-based nanodiode fabrication. In both cases, the inclusion of an appropriate RTA step was found to dramatically improve device stability and reproducibility.

Annealing TiO_x is well known to improve film characteristics[20]. For the TiO_x devices, RTA was used to crystallize the amorphous as-deposited TiO_x and to further oxidize the material. Further oxidation of the TiO_x was necessary to increase resistivity and ensure the formation of a high-quality Schottky contact between Rh and TiO_x. Annealing each wafer in a flow of oxygen at 350°C for 5 minutes after initial TiO_x deposition helped to increase the yield of good devices from ~5% to above 90%. The device quality was very sensitive to the annealing temperature. Annealing at an even slightly higher temperature, such as 400°C, was found to increase resistivity too much and resulted in insulating Rh/TiO_x contacts, while annealing at even a slightly lower temperature, such as 275°C, often resulted in ohmic contacts between Rh and TiO_x.

The GaN devices were not as sensitive to annealing conditions, but RTA was still found to improve device characteristics. For these devices, RTA was carried out in N_2 at 500°C for 5 minutes after deposition of the ohmic contact to GaN in order to promote alloy formation and lower contact resistance. This process and the mechanisms behind the improved contact resistance have been documented extensively in the thin film literature[7, 21].

RTA was done using an AG Associates Heatpulse 210T Rapid Thermal Annealing System available for use at the University of California, Berkeley Microlab facility.

2.2. Nanoparticle Synthesis

Tremendous progress has been made in nanoparticle synthesis in the past twenty years. Modern chemists have developed methods to control nanoparticle size, shape, composition, and even alloy structure for a wide variety of materials, including metals, semiconductors, and insulators. Nanoparticles are also rapidly finding their way into countless commercially relevant products and research in the field has mushroomed. This progress has been particularly important in the area of catalysis. Nanoparticles are of special interest in catalysis because of their high surface-to-volume ratio and because of the wide range of unique catalytic regimes which have been discovered for very small particles, such as size sensitivity[22-24]. In the present work, nanoparticles with controlled shape and composition have been synthesized in order to further understand the role that these parameters play in determining catalytic activity.

2.2.1. Shape Control

Shape has emerged as an important factor in nanoparticle behavior, especially in optical[25-27] and catalytic[28-36] systems. As a result of this, the development of synthetic methods to control nanoparticle shape has become an area of particular interest[37-39]. The most common single-crystalline shapes synthesized include polyhedrons, cubes, truncated cubes, cuboctahedrons, truncated octahedrons, octahedrons, tetrahedrons, nanorods, hexagonal plates, and triangular plates[39]. Several examples of these shapes are included in Figure 2.10. Many other shapes can be generated using twinned or multiply-twinned nanoparticle geometries. A wide variety of different approaches have been used to produce nanoparticles of varied shape, such as vapor-phase evaporation onto solid substrates[40], laser-mediated growth[41], electrochemical syntheis[42], and reduction of transition metal salts[33, 37, 39, 43-45].

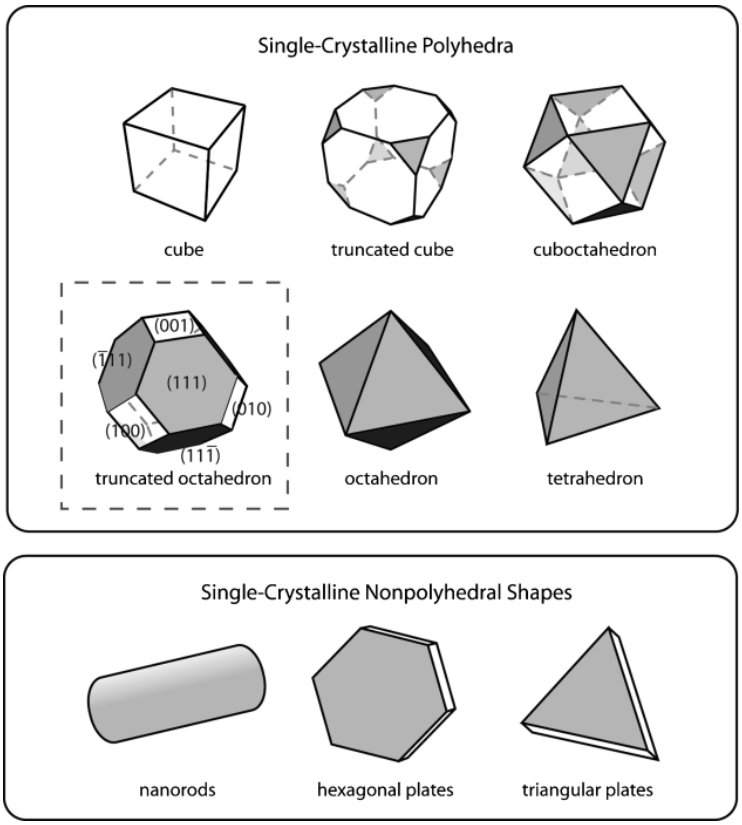

Figure 2.10 Examples of nanoparticle shapes which have been synthesized. The polyhedral shapes differ based on their degree of corner truncation, whereas the nonpolyhedral shapes are design through careful control of aspect ratio and other factors[39].

Of these methods, the most common is the chemical reduction of transition metal salts, which is perhaps the most straightforward and reproducible approach to shape control[46]. In equilibrium conditions, nanoparticle shape is dominated by surface energy minimization because there is little difference between the lattice energy of different facets[47]. The lowest surface energy is typically achieved by a spherical or near-spherical shape. Although it is possible to achieve non-equilibrium shapes kinetically by the use of high growth rates, for which small differences in energy become important and high-energy facets grow faster than low-energy facets, a simpler approach is to use organic capping agents to preferentially inhibit nanoparticle growth along one crystal plane relative to another[47, 48]. For example, a capping agent could be used that binds much more strongly to a (111) crystal face than to a (100) crystal face. This disparity would cause the relative growth rate on the (100) face to exceed the growth rate on the (111) face, eventually resulting in a cubic structure[43]. Although shape control has also been achieved using silver ions as a capping agent rather than organics, such as poly(vinylpyrrolidone) (PVP), this approach was found to poison the catalytic behavior of the synthesized nanoparticles[49]. The interaction of organic capping agents with metal nanoparticles is not fully understood, however, and remains an area of active study[50-52]. The choice of metal salt is also known to affect nanoparticle shape[45].

The two major approaches to nanoparticle shape control are homogeneous and heterogeneous nucleation. The primary difference between these two approaches is whether the nanoparticle seeds, i.e. small clusters that serve as nucleation sites for particle growth, are formed *in situ* or formed in a separate reaction step. In practice, homogeneous nucleation is more

often used because of the simplicity of the one-pot synthesis. Heterogeneous nucleation requires synthesis of the nanoparticle seeds in one reactor followed by carefully controlled transfer to another reactor for nanoparticle growth. The advantage of heterogeneous nucleation is that it isolates seed nucleation and allows separate tuning of the nucleation and growth steps[39]. Heterogeneous nucleation also leads to more monodispersity in nanoparticle sizes. This added layer of control can be useful because growth on a pre-existing nanoparticle seed requires much less thermodynamic energy than seed particle nucleation[53]. Images of (100) and (111)-oriented metal nanoparticles synthesized using these techniques are included in Figure 2.11.

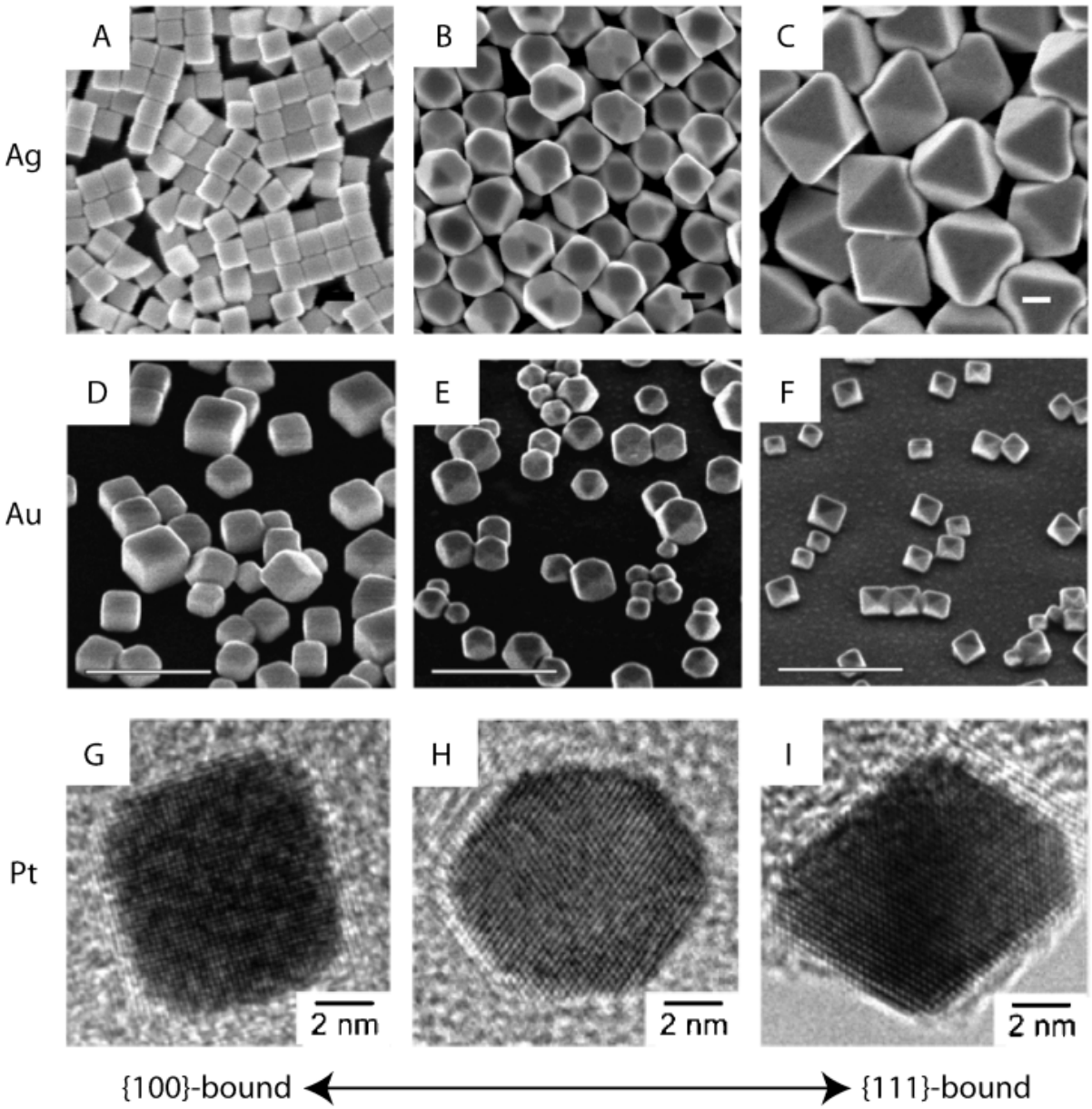

Figure 2.11 Images of Ag, Au, and Pt nanoparticles bound by fcc (100) and (111) planes. These nanoparticles were synthesized using an approach in which the relative stabilization of the (100) and (111) facets was controlled through selective use of capping agents[39].

In this work, all syntheses use the homogeneous nucleation approach. Each synthesis consists of three primary elements: a metal salt precursor, a capping agent or mixture of capping agents, and a polyol liquid. When the mixture is heated and stirred, the metal salt and capping agent(s) dissolve in the polyol liquid and the metal salt is reduced by the polyol. The reduced metal ions form seeds. Nanoparticle growth rate is mediated by the capping agent, which stabilizes growth and prevents uncontrolled aggregation of the nanoparticles. Shape is controlled through the use of capping agents with preferential binding for one crystal face. Nanoparticle growth continues until the reaction is quenched by lowering the temperature. Parameters such as reactant and capping agent concentration, reaction time, and reaction temperature must all be optimized in order to achieve desired nanoparticle size and shape. Shape is controlled in this work through the choice of capping agent, with PVP used for synthesis of 6.5 nm nanopolyhedra and a combination of PVP and tetramethylammonium bromide (TTAB) used for the synthesis of 6.2 nm nanocubes. This synthesis is described in detail in Section 5.3.2.

2.2.2. Composition Control

Bimetallic nanoparticle systems are of great interest in heterogeneous catalysis because of their unique synergetic behavior under certain conditions[54-56]. There are two primary paths to synthesizing bimetallic nanoparticles – co-reduction of precursors and sequential reduction of precursors[46, 57]. The difference between the two is that in a sequential process, monometallic nanoparticle cores are formed prior to reduction of the second metal salt, whereas the two precursors are both added to the solution prior to reaction in co-reduction. Sequential reduction can be thought of as similar to a seeded growth strategy in monometallic nanoparticle synthesis, in which seed formation is performed separately from the growth step. In this case, the second metal precursor is added after core formation. Of these two bimetallic growth strategies, co-reduction is generally presented as preferable for the formation of bimetallic alloys and sequential reduction is considered best for the formation of core-shell structures[46, 57]. The synthetic strategy used to form metal nanoparticles using the co-reduction method is diagrammed in Figure 2.12.

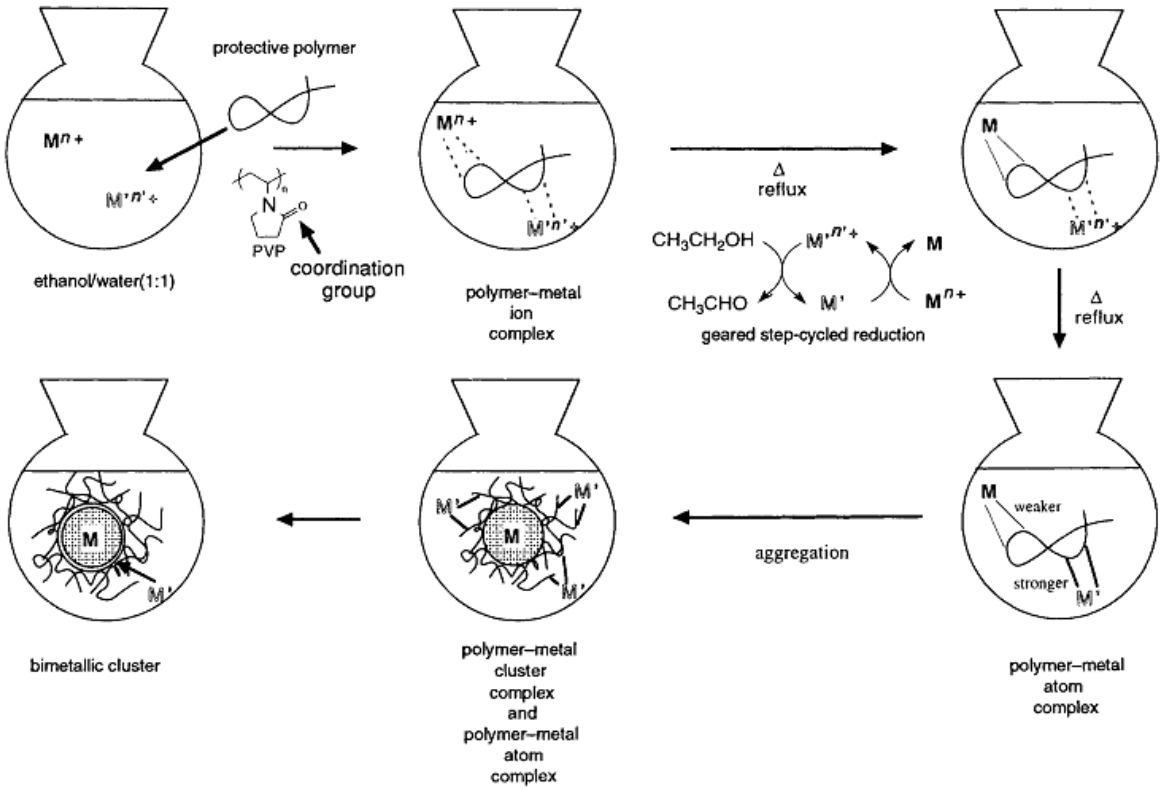

Figure 2.12 Bimetallic nanoparticle formation mechanism for PVP-capped nanoparticles synthesized using co-reduction in alcohol[58].

This simple precursor addition order model does not adequately predict real bimetallic nanoparticle structure, however. In fact, both methods have achieved alloy and core-shell structures. Both Hg-Ag bimetallic alloy nanoparticle structures[59] and Hg-Ag Ag-core/Hg-shell nanoparticles[60] have been produced using a co-reduction strategy, while three kinds of Au-Pd bimetallic nanoparticles, random alloy, Au core-Pd shell, and Pd core-Au shell, have been formed using successive reduction[61]. In addition, the bimetallic Pd core-Rh shell nanoparticles studied in Chapters 6 and 7 were formed using a co-reduction technique. The actual formation mechanism underlying bimetallic nanoparticle synthesis is more closely related to reduction potentials.

Bimetallic nanoparticle structure is determined by the relative energetics of the reduction of the two metal salt precursors. If one metal ion is much more easily reduced than the other, it will begin to form nanoparticle cores much more quickly, even if the two salts were added simultaneously. As a result, it is possible to form core-shell nanoparticles even using a co-reduction strategy. In a sequential reduction process, the ions of the second metal added will reduce the nanoparticle cores formed by the first metal if the redox potential of the second metal is high enough[62]. This process can lead to a mixed alloy interstitial region between the core and shell, a completely alloyed nanoparticle, or, in the case of relatively small nanoparticle cores or a very large difference in redox potentials, can even lead to a core-shell nanoparticle in which the second metal forms the nanoparticle core and the first metal becomes the shell.

The stabilizing, or capping, agent is also very important in bimetallic nanoparticle growth. Without a capping agent, such as PVP, it is very challenging to synthesize a core-shell nanoparticle[57]. The capping agent is important because it helps to stabilize metal ions prior to

reduction by coordination. After coordination to the metal ions and reduction of ions to zerovalent metal atoms, the polymer also plays an important role in stabilizing the small metal atoms and clusters as nanoparticle growth continues.

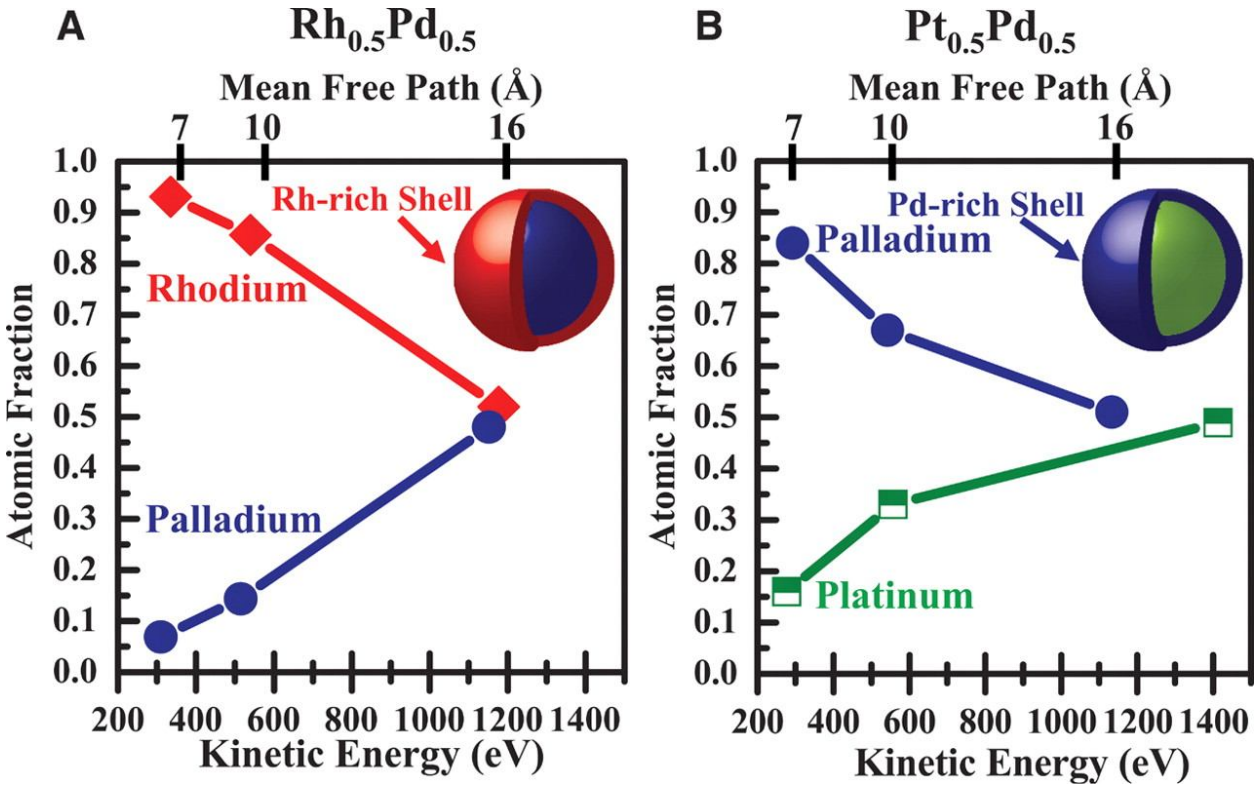

Figure 2.13 X-Ray Photoelectron Spectroscopy using variable photon energy to demonstrate the core-shell structure of $Rh_{0.5}Pd_{0.5}$ and $Pt_{0.5}Pd_{0.5}$ bimetallic nanoparticles synthesized using co-reduction in alcohol[63]. Low kinetic energy electrons are more sensitive to surface layers than high kinetic energy electrons. In (A), the $Rh_{0.5}Pd_{0.5}$ nanoparticle is shown to be Rh-rich at the surface and of mixed composition in the bulk. In (B), the $Pt_{0.5}Pd_{0.5}$ nanoparticle is shown to be Pd-rich at the surface and of mixed composition in the bulk.

As a whole, the process of bimetallic core-shell nanoparticle synthesis by co-reduction in alcohol, as used to synthesize the Rh-Pd nanoparticles with PVP capping agent studied in this work, can be described as a series of several steps. First, the metal ions in solution coordinate to the PVP. The metal with higher reduction potential, Pd in this case, is reduced to its zerovalent state. This metal begins to aggregate and form clusters because it is not strongly bound to the PVP capping agent. During this process, the second metal, with lower reduction potential, also begins to be reduced, but the zerovalent second metal is more strongly bound to the PVP than the zerovalent first metal and as a result aggregates into the nanoparticle structure at a slower rate. The degree of alloying depends on the difference in the rates of ion reduction and nanoparticle aggregation as determined by reduction potentials and the strength of the atom-polymer complex[57]. Core-shell structure can be confirmed using a variety of characterization techniques, including X-Ray Diffraction, X-Ray Photoelectron Spectroscopy, and Energy Dispersive X-Ray Analysis, among others. An example of this is given in Figure 2.13.

Details regarding the synthesis of Rh-Pd bimetallic core-shell nanoparticles are provided in Section 6.2.

2.2.3. Nanoparticle Deposition

The two most common ways of preparing nanoparticle samples in our lab are 2D and 3D. 2D samples consist of nanoparticles deposited directly on a flat substrate, such as a silicon wafer, whereas 3D samples are prepared by sonicating a solution of nanoparticles into a porous oxide support such that the nanoparticles are relatively well-dispersed within the support. The primary advantage of using 2D nanoparticle supports is that the samples can easily be characterized using ultra-high vacuum techniques, such as electron microscopy and x-ray spectroscopy. This approach eliminates any potential ambiguity regarding differences in nanoparticle behavior due to changes in the support and local environment of the nanoparticles, which can sometimes be a problem with 3D samples. The main advantage of using 3D samples, however, is that the enormous increase in surface area allows catalytic studies to be carried out using a much larger amount of catalyst, which improves the accuracy of catalytic measurements and more precisely models the catalyst geometries found in industrial applications. The nanoparticle studies presented here were all carried out in a 2D geometry so as to facilitate sample characterization.

2.2.3.1. Dropcasting

The simplest strategy for deposition of nanoparticles on a 2D support is dropcasting. Dropcasting is done by pipetting a drop of nanoparticle solution on to the support. Although pipetting is a very straightforward and simple technique, it is extremely irreproducible and allows only the most rudimentary control over nanoparticle surface coverage. Dropcasting often leads to undesirable multi-layer structures and leads to very high uncertainty in the surface site calculations necessary to compare catalyst activity. Dropcasting is best used only for experiments in which control of sample concentration is not required, such as in preparing samples for X-Ray Diffraction (XRD) experiments, in which a large amount of sample is needed in order to have measureable signal and the only information of interest is nanoparticle lattice structure, which does not change with particle concentration. In this thesis, the only samples prepared using the dropcasting technique were those used for XRD.

2.2.3.2. The Langmuir-Blodgett Technique

The Langmuir-Blodgett technique is used to deposit a controllable surface coverage of evenly-spaced nanoparticles on a 2D surface. As shown in Figure 2.14, the apparatus consists of a water-filled Teflon trough with a moveable barrier separating the trough into two partitions. Pieces of wafer or other 2D support are submerged in the water on a moveable platform which can be brought up above the surface of the water. Individual droplets of nanoparticles are placed on the water surface such that the nanoparticles do not penetrate the surface and remain suspended atop the water. Less than one monolayer is added, as can be easily checked visually for a sufficiently dilute sample. The barrier is then moved towards the wafer platform in order to compress the water surface and the nanoparticle film supported on it. Barrier movement is stopped when the surface pressure reaches a known value. After the surface equilibrates, the wafer platform is slowly raised up above the water such that the nanoparticles are transferred to the wafer surface[64]. This technique is commonly used for the study of nanoparticle catalysis on 2D supports because it enables accurate characterization of the number of surface sites, which is necessary in order to determine turnover frequency.

Langmuir-Blodgett nanoparticle deposition was carried out in a specialized LB trough in Professor Peidong Yang's laboratory at the University of California, Berkeley. Our nanoparticles

were typically deposited at a surface pressure of 15 mN/m in order to obtain coverage of around 30% of a monolayer. This coverage provides a large number of nanoparticles without risking multilayer formation.

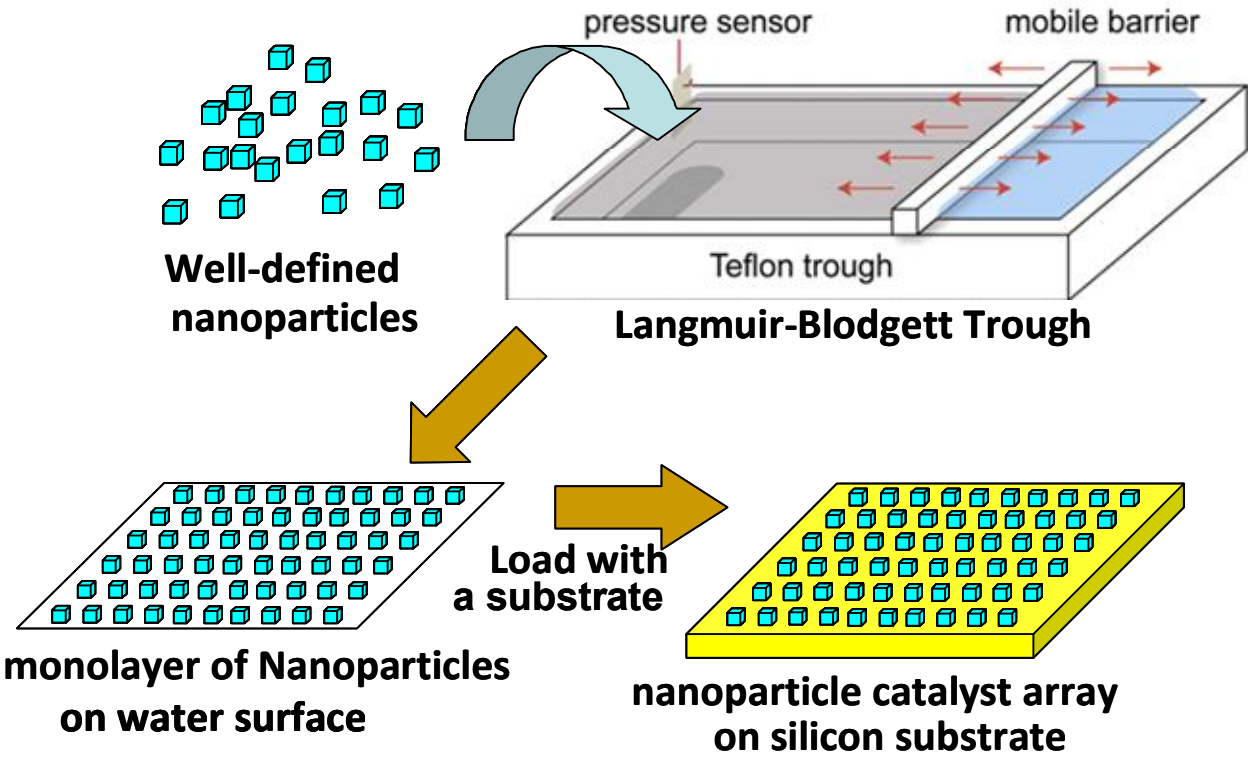

Figure 2.14 The Langmuir-Blodgett Technique. Nanoparticles are uniformly deposited on a substrate by dropcasting the nanoparticles on a water surface and compressing the surface prior to lifting the substrate up from below the surface. A well-separated layer of nanoparticles with controlled uniform coverage can be deposited on a substrate using this method. Adapted from [65].

2.3. References

1. Ji, X. Z.; Zuppero, A.; Gidwani, J. M.; Somorjai, G. A., The catalytic nanodiode: Gas phase catalytic reaction generated electron flow using nanoscale platinum titanium oxide Schottky diodes. *Nano Lett.* **2005,** *5* (4), 753-756.
2. Mergel, D.; Buschendorf, D.; Eggert, S.; Grammes, R.; Samset, B., Density and refractive index of TiO2 films prepared by reactive evaporation. *Thin Solid Films* **2000,** *371* (1-2), 218-224.
3. Park, J. Y.; Somorjai, G. A., Energy conversion from catalytic reaction to hot electron current with metal-semiconductor Schottky nanodiodes. *J. Vac. Sci. Technol. B* **2006,** *24* (4), 1967-1971.
4. Hervier, A.; Renzas, J. R.; Park, J. Y.; Somorjai, G. A., Hydrogen Oxidation-Driven Hot Electron Flow Detected by Catalytic Nanodiodes. *Nano Lett.* **2009,** *9* (11), 3930-3933.

5. Park, J. Y.; Lee, H.; Renzas, J. R.; Zhang, Y. W.; Somorjai, G. A., Probing hot electron flow generated on Pt nanoparticles with Au/TiO2 Schottky diodes during catalytic CO oxidation. *Nano Lett.* **2008,** *8* (8), 2388-2392.
6. Ji, X. Z.; Zuppero, A.; Gidwani, J. M.; Somorjai, G. A., Electron flow generated by gas phase exothermic catalytic reactions using a platinum-gallium nitride nanodiode. *Journal of the American Chemical Society* **2005,** *127* (16), 5792-5793.
7. Luther, B. P.; Mohney, S. E.; Jackson, T. N.; Khan, M. A.; Chen, Q.; Yang, J. W., Investigation of the mechanism for Ohmic contact formation in Al and Ti/Al contacts to [bold n]-type GaN. *Applied Physics Letters* **1997,** *70* (1), 57-59.
8. Rossnagel, S. M., Thin film deposition with physical vapor deposition and related technologies. *Journal of Vacuum Science & Technology A* **2003,** *21* (5), S74-S87.
9. Berg, S.; Blom, H. O.; Larsson, T.; Nender, C., Modeling of reactive sputtering of compound materials. *Journal of Vacuum Science & Technology A: Vacuum, Surfaces, and Films* **1987,** *5* (2), 202-207.
10. Berg, S.; Nyberg, T., Fundamental understanding and modeling of reactive sputtering processes. *Thin Solid Films* **2005,** *476* (2), 215-230.
11. Berg, S.; Larsson, T.; Nender, C.; Blom, H. O., Predicting thin-film stoichiometry in reactive sputtering. *J. Appl. Phys.* **1988,** *63* (3), 887-891.
12. Chung, C. K.; Liao, M. W.; Lai, C. W., Effects of oxygen flow ratios and annealing temperatures on Raman and photoluminescence of titanium oxide thin films deposited by reactive magnetron sputtering. *Thin Solid Films* **2009,** *518* (5), 1415-1418.
13. Tang, H.; Prasad, K.; Sanjines, R.; Schmid, P. E.; Levy, F., ELECTRICAL AND OPTICAL-PROPERTIES OF TIO2 ANATASE THIN-FILMS. *J. Appl. Phys.* **1994,** *75* (4), 2042-2047.
14. Liu, B.; Wen, L.; Zhao, X., The photoluminescence spectroscopic study of anatase TiO2 prepared by magnetron sputtering. *Mater. Chem. Phys.* **2007,** *106* (2-3), 350-353.
15. Boukrouh, S.; Bensaha, R.; Bourgeois, S.; Finot, E.; de Lucas, M. C. M., Reactive direct current magnetron sputtered TiO2 thin films with amorphous to crystalline structures. *Thin Solid Films* **2008,** *516* (18), 6353-6358.
16. Wicaksana, D.; Kobayashi, A.; Kinbara, A. In *Process effects on structural properties of TiO[sub 2] thin films by reactive sputtering*, 38th National Symposium of the American Vacuum Society, Seattle, Washington (USA), AVS: Seattle, Washington (USA), 1992; pp 1479-1482.
17. Musil, J.; Baroch, P.; Vlcek, J.; Nam, K. H.; Han, J. G., Reactive magnetron sputtering of thin films: present status and trends. *Thin Solid Films* **2005,** *475* (1-2), 208-218.
18. Löbl, P.; Huppertz, M.; Mergel, D., Nucleation and growth in TiO2 films prepared by sputtering and evaporation. *Thin Solid Films* **1994,** *251* (1), 72-79.
19. Ohring, M., *Materials Science of Thin Films*. Academic Press: Boston, 1992.
20. Hou, Y. Q.; Zhuang, D. M.; Zhang, G.; Zhao, M.; Wu, M. S., Influence of annealing temperature on the properties of titanium oxide thin film. *Appl. Surf. Sci.* **2003,** *218* (1-4), 97-105.
21. Ruvimov, S.; Liliental-Weber, Z.; Washburn, J.; Duxstad, K. J.; Haller, E. E.; Fan, Z. F.; Mohammad, S. N.; Kim, W.; Botchkarev, A. E.; Morkoc, H., Microstructure of Ti/Al and Ti/Al/Ni/Au Ohmic contacts for n-GaN. *Applied Physics Letters* **1996,** *69* (11), 1556-1558.
22. Grass, M.; Rioux, R.; Somorjai, G., Dependence of Gas-Phase Crotonaldehyde Hydrogenation Selectivity and Activity on the Size of Pt Nanoparticles (1.7-7.1 nm) Supported on SBA-15. *Catalysis Letters* **2009,** *128* (1-2), 1-8.

23. Grass, M. E.; Zhang, Y. W.; Butcher, D. R.; Park, J. Y.; Li, Y. M.; Bluhm, H.; Bratlie, K. M.; Zhang, T. F.; Somorjai, G. A., A Reactive Oxide Overlayer on Rhodium Nanoparticles during CO Oxidation and Its Size Dependence Studied by In Situ Ambient-Pressure X-ray Photoelectron Spectroscopy. *Angewandte Chemie-International Edition* **2008,** *47* (46), 8893-8896.
24. Rioux, R. M.; Hsu, B. B.; Grass, M. E.; Song, H.; Somorjai, G. A., Influence of Particle Size on Reaction Selectivity in Cyclohexene Hydrogenation and Dehydrogenation over Silica-Supported Monodisperse Pt Particles. *Catalysis Letters* **2008,** *126* (1-2), 10-19.
25. Yu, Y. Y.; Chang, S. S.; Lee, C. L.; Wang, C. R. C., Gold nanorods: Electrochemical synthesis and optical properties. *J. Phys. Chem. B* **1997,** *101* (34), 6661-6664.
26. Jin, R. C.; Cao, Y. W.; Mirkin, C. A.; Kelly, K. L.; Schatz, G. C.; Zheng, J. G., Photoinduced conversion of silver nanospheres to nanoprisms. *Science* **2001,** *294* (5548), 1901-1903.
27. Sherry, L. J.; Chang, S. H.; Schatz, G. C.; Van Duyne, R. P.; Wiley, B. J.; Xia, Y. N., Localized surface plasmon resonance spectroscopy of single silver nanocubes. *Nano Lett.* **2005,** *5* (10), 2034-2038.
28. Bratlie, K. M.; Lee, H.; Komvopoulos, K.; Yang, P. D.; Somorjai, G. A., Platinum nanoparticle shape effects on benzene hydrogenation selectivity. *Nano Lett.* **2007,** *7* (10), 3097-3101.
29. El-Sayed, M. A., Shape-dependent nanocatalysis and the effect of catalysis on the nanoparticle shape and size in colloidal solution. *Abstracts of Papers of the American Chemical Society* **2006,** *231*, 212-IEC.
30. Lee, I.; Delbecq, F.; Morales, R.; Albiter, M. A.; Zaera, F., Tuning selectivity in catalysis by controlling particle shape. *Nature Materials* **2009,** *8* (2), 132-138.
31. Narayanan, R.; El-Sayed, M. A., Shape-dependent catalytic activity of platinum nanoparticles in colloidal solution. *Nano Lett.* **2004,** *4* (7), 1343-1348.
32. Narayanan, R.; El-Sayed, M. A., Catalysis with transition metal nanoparticles in colloidal solution: Nanoparticle shape dependence and stability. *J. Phys. Chem. B* **2005,** *109* (26), 12663-12676.
33. Peng, Z. M.; Yang, H., Designer platinum nanoparticles: Control of shape, composition in alloy, nanostructure and electrocatalytic property. *Nano Today* **2009,** *4* (2), 143-164.
34. Renzas, J. R.; Zhang, Y.; Huang, W. Y.; Somorjai, G. A., Rhodium Nanoparticle Shape Dependence in the Reduction of NO by CO. *Catalysis Letters* **2009**.
35. Subhramannia, M.; Pillai, V. K., Shape-dependent electrocatalytic activity of platinum nanostructures. *Journal of Materials Chemistry* **2008,** *18* (48), 5858-5870.
36. Tsung, C. K.; Kuhn, J. N.; Huang, W. Y.; Aliaga, C.; Hung, L. I.; Somorjai, G. A.; Yang, P. D., Sub-10 nm Platinum Nanocrystals with Size and Shape Control: Catalytic Study for Ethylene and Pyrrole Hydrogenation. *Journal of the American Chemical Society* **2009,** *131* (16), 5816-5822.
37. Ahmadi, T. S.; Wang, Z. L.; Green, T. C.; Henglein, A.; ElSayed, M. A., Shape-controlled synthesis of colloidal platinum nanoparticles. *Science* **1996,** *272* (5270), 1924-1926.
38. Song, H.; Kim, F.; Connor, S.; Somorjai, G. A.; Yang, P. D., Pt nanocrystals: Shape control and Langmuir-Blodgett monolayer formation. *J. Phys. Chem. B* **2005,** *109* (1), 188-193.
39. Tao, A. R.; Habas, S.; Yang, P. D., Shape control of colloidal metal nanocrystals. *Small* **2008,** *4* (3), 310-325.

40. Baletto, F.; Ferrando, R., Structural properties of nanoclusters: Energetic, thermodynamic, and kinetic effects. *Rev. Mod. Phys.* **2005,** *77* (1), 371-423.
41. Pyatenko, A.; Yamaguchi, M.; Suzuki, M. In *"Soft" and "hard" laser treatments of noble metals nanoparticles. How do they work in particle size and shape control?*, 2009 Conference on Lasers & Electro-Optics Europe & 11th European Quantum Electronics Conference (CLEO/EQEC), Munich, Germany, 14-19 June; Ieee: Munich, Germany, 2009; pp 1 pp.-1 pp.
42. Yu; Chang, S.-S.; Lee, C.-L.; Wang, C. R. C., Gold Nanorods: Electrochemical Synthesis and Optical Properties. *The Journal of Physical Chemistry B* **1997,** *101* (34), 6661-6664.
43. Lu, X. M.; Rycenga, M.; Skrabalak, S. E.; Wiley, B.; Xia, Y. N., Chemical Synthesis of Novel Plasmonic Nanoparticles. *Annu. Rev. Phys. Chem.* **2009,** *60*, 167-192.
44. Zhang, Y. W.; Grass, M. E.; Habas, S. E.; Tao, F.; Zhang, T. F.; Yang, P. D.; Somorjai, G. A., One-step polyol synthesis and langmuir-blodgett monolayer formation of size-tunable monodisperse rhodium nanocrystals with catalytically active (111) surface structures. *Journal of Physical Chemistry C* **2007,** *111* (33), 12243-12253.
45. Zhang, Y. W.; Grass, M. E.; Kuhn, J. N.; Tao, F.; Habas, S. E.; Huang, W. Y.; Yang, P. D.; Somorjai, G. A., Highly selective synthesis of cataytically active monodisperse rhodium nanocubes. *Journal of the American Chemical Society* **2008,** *130* (18), 5868-+.
46. Roucoux, A.; Schulz, J.; Patin, H., Reduced transition metal colloids: A novel family of reusable catalysts? *Chemical Reviews* **2002,** *102* (10), 3757-3778.
47. Yin, Y.; Alivisatos, A. P., Colloidal nanocrystal synthesis and the organic-inorganic interface. *Nature* **2005,** *437* (7059), 664-670.
48. Xia, Y.; Xiong, Y. J.; Lim, B.; Skrabalak, S. E., Shape-Controlled Synthesis of Metal Nanocrystals: Simple Chemistry Meets Complex Physics? *Angewandte Chemie-International Edition* **2009,** *48* (1), 60-103.
49. Grass, M. E.; Yue, Y.; Habas, S. E.; Rioux, R. M.; Teall, C. I.; Yang, P.; Somorjai, G. A., Silver ion mediated shape control of platinum nanoparticles: Removal of silver by selective etching leads to increased catalytic activity. *Journal of Physical Chemistry C* **2008,** *112* (13), 4797-4804.
50. Borodko, Y.; Habas, S. E.; Koebel, M.; Yang, P. D.; Frei, H.; Somorjai, G. A., Probing the interaction of poly(vinylpyrrolidone) with platinum nanocrystals by UV-Raman and FTIR. *J. Phys. Chem. B* **2006,** *110* (46), 23052-23059.
51. Borodko, Y.; Humphrey, S. M.; Tilley, T. D.; Frei, H.; Somorjai, G. A., Charge-transfer interaction of poly(vinylpyrrolidone) with platinum and rhodium nanoparticles. *Journal of Physical Chemistry C* **2007,** *111* (17), 6288-6295.
52. Borodko, Y.; Jones, L.; Lee, H.; Frei, H.; Somorjai, G., Spectroscopic Study of Tetradecyltrimethylammonium Bromide Pt-C(14)TAB Nanoparticles: Structure and Stability. *Langmuir* **2009,** *25* (12), 6665-6671.
53. Markov, I. V., *Crystal Growth for Beginners: Fundamentals of Nucleation, Crystal Growth, and Epitaxy*. World Scientific Publishing Company: 2003.
54. Thomas, J. M.; Raja, R.; Johnson, B. F. G.; Hermans, S.; Jones, M. D.; Khimyak, T., Bimetallic Catalysts and Their Relevance to the Hydrogen Economy. *Industrial & Engineering Chemistry Research* **2003,** *42* (8), 1563-1570.
55. Sinfelt, J. H., *Bimetallic Catalysis: Discoveries, Concepts, and Applications*. Wiley: New York, 1983.

56. Basile, F.; Fornasari, G.; Trifirò, F.; Vaccari, A., Rh-Ni synergy in the catalytic partial oxidation of methane: surface phenomena and catalyst stability. *Catalysis Today* **2002,** *77* (3), 215-223.
57. Toshima, N.; Yonezawa, T., Bimetallic nanoparticles - novel materials for chemical and physical applications. *New Journal of Chemistry* **1998,** *22* (11), 1179-1201.
58. Yonezawa, T.; Toshima, N., MECHANISTIC CONSIDERATION OF FORMATION OF POLYMER-PROTECTED NANOSCOPIC BIMETALLIC CLUSTERS. *Journal of the Chemical Society-Faraday Transactions* **1995,** *91* (22), 4111-4119.
59. Henglein, A.; Brancewicz, C., Absorption spectra and reactions of colloidal bimetallic nanoparticles containing mercury. *Chem. Mat.* **1997,** *9* (10), 2164-2167.
60. Katsikas, L.; Gutierrez, M.; Henglein, A., Bimetallic colloids: Silver and mercury. *Journal of Physical Chemistry* **1996,** *100* (27), 11203-11206.
61. Michel, J. H.; Schwartz, J. T., *Stud. Surf. Sci. Catal.* **1987,** *31*, 669.
62. Wang, Y.; Toshima, N., Preparation of Pd-Pt bimetallic colloids with controllable core/shell structures. *J. Phys. Chem. B* **1997,** *101* (27), 5301-5306.
63. Tao, F.; Grass, M. E.; Zhang, Y. W.; Butcher, D. R.; Renzas, J. R.; Liu, Z.; Chung, J. Y.; Mun, B. S.; Salmeron, M.; Somorjai, G. A., Reaction-Driven Restructuring of Rh-Pd and Pt-Pd Core-Shell Nanoparticles. *Science* **2008,** *322* (5903), 932-934.
64. Schwartz, D. K., Langmuir-Blodgett film structure. *Surface Science Reports* **1997,** *27* (7-8), 245-334.
65. Somorjai, G.; Tao, F.; Park, J., The Nanoscience Revolution: Merging of Colloid Science, Catalysis and Nanoelectronics. *Topics in Catalysis* **2008,** *47* (1), 1-14.

Chapter 3. Characterization Techniques

Modern catalysis research necessitates the use of a wide variety of characterization techniques to verify the size, shape, composition, and lattice structure of nanometer-scale thin films and particles. In this thesis, nanoparticle catalysts are studied *ex-situ* before and after reaction to determine the effect of high temperature (~250°C) catalytic reactions on the particle morphology and composition. Thin film nanodiodes are studied using a combination of microscopy and electrical characterization in order to understand both their morphological and electrical stability.

3.1. Scanning Electron Microscopy

Scanning electron microscopy (SEM) is among the most common surface science techniques in use today. The primary use of SEM is to obtain nanometer-scale topographic information about a surface. In basic terms, SEM operates by focusing a beam of high energy electrons on a surface and collecting secondary or backscattered electrons. An image is formed by rastering the electron beam across the surface plane and assigning contrast to the number of electrons counted at each point. A typical SEM image is presented in Figure 3.1. This image demonstrates the ability of SEM to clearly show morphological characteristics of a surface. The weaknesses of SEM include its inability to clearly distinguish between elements and to obtain height information from surface features without destroying the sample for use in cross-sectional analysis.

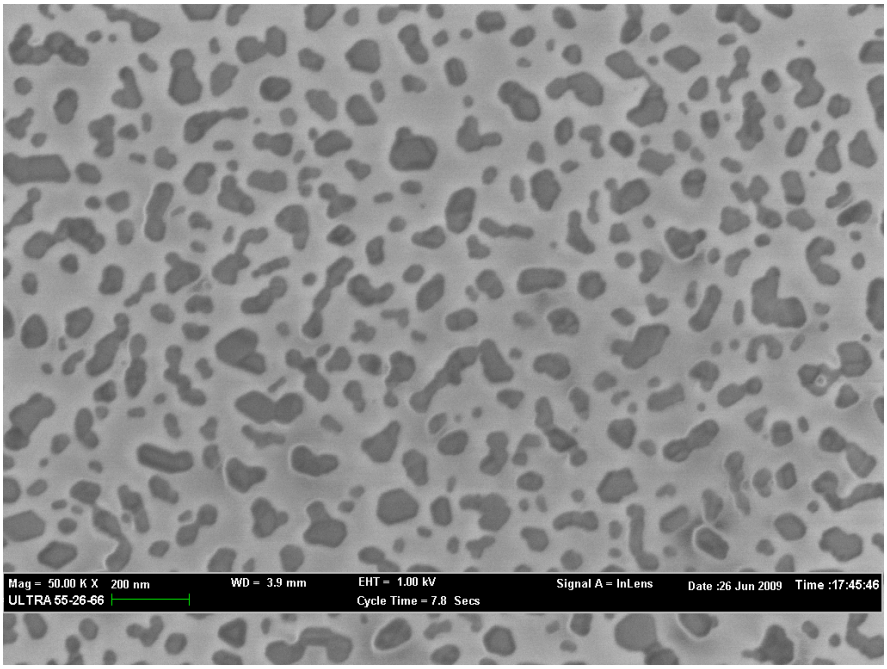

Figure 3.1 SEM of 8 nm Pd thin film on p-type Si after treatment at 300°C.

Conceptually, SEM has been around since 1927, when it was proposed by Stintzing in a German patent for use in determining the size and number of particles on a surface. Stintzing's formulation was for a one-dimensional scan and he is not known to have attempted construction of the instrument[1]. Although Max Knoll succeeded in producing an SEM image by 1935, the SEM was not commercially available until 1965, when Sir Charles Oakley of Cambridge University succeeded in developing an instrument and convincing the Cambridge Instrument Company to market and sell it as the first commercial SEM[2].

The modern SEM is a marvel of engineering in the service of science. The instrument is diagrammed in Figure 3.2 and begins with an electron gun. The electron gun is typically a filament or sharp tip. A resistive Tungsten or LaB_6 filament heated by an electrical current emits electrons through the process of thermionic emission. The filament material affects the brightness, source size, and vacuum requirements of the emitted beam. The brightness is of particular importance because of its relationship to the signal-to-noise ratio of the instrument. Tungsten has a brightness of 10^5 A cm^{-2} sr^{-1} and requires a 10^{-6} Torr vacuum, whereas LaB_6 has an order of magnitude more brightness at the cost of requiring a vacuum of 10^{-8} Torr. Brightness can be improved to as high as 10^9 A cm^{-2} sr^{-1} at the cost of a greater vacuum requirement of 10^{-10} Torr by using a cold field emitter, which operates by the application of a DC potential to a tungsten tip until the resulting electric field is high enough to cause electron emission[3]. Electric field strength depends on the ratio of applied voltage to the tip radius and can thus be enhanced by shrinking the tip to 100 nm or less.

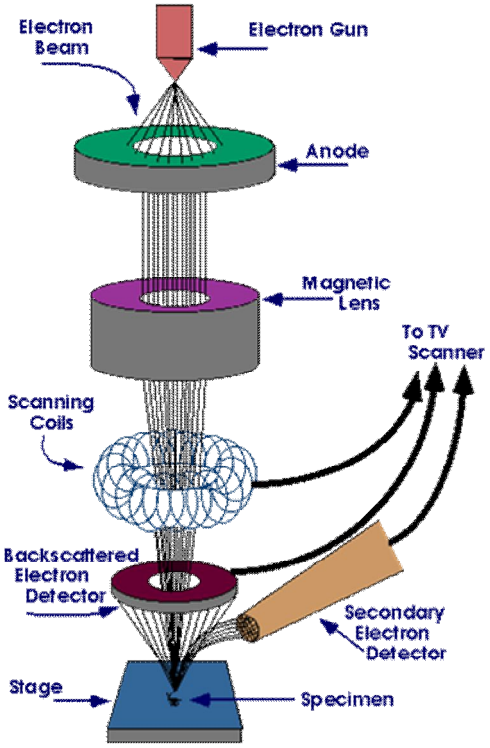

Figure 3.2 Schematic of a Scanning Electron Microscope[3]

Electrons produced by the electron gun are accelerated towards the sample by an anode and focused with a series of magnetic lenses in the column. The quality of beam focus and, consequently, the physical size of the beam, is critical to the generation of high resolution SEM images. The anode is used to control the acceleration voltage, which typically ranges from 1-30

kV. A high acceleration voltage improves resolution at the cost of increased sample charging, which can severely degrade image quality. The first lenses encountered by the electron beam are condenser. Condenser lenses used in electron microscopy are magnetic analogues of their common optical forbears. A series of condenser lenses focus and refocus the beam and can be used to control beam diameter. Smaller beam diameters have improved resolution at the cost of decreased signal-to-noise ratio. The SEM column also includes scanning coils used to raster the beam across the surface and stigmation coils, which are used to account and correct for unequal deflection in the x and y axes in order to obtain a perfectly round beam. The final element of the column is the objective lens, which controls the final beam focus distance. A very short focal length has improved resolution at the cost of a worse depth of field, which limits the ability to resolve features in the z-dimension[4].

Figure 3.3 Zeiss Ultra 55 Field Emission SEM at Lawrence Berkeley National Laboratory's Molecular Foundry

Once the electron reaches the surface, the interaction can be either elastic or inelastic in nature. Backscattered electrons are elastic in nature, meaning they do not suffer significant loss of energy and simply scatter off the surface, whereas secondary electrons with typical energies of about 10 eV result from an inelastic interaction. The majority of electrons are backscattered. These electrons suffer no energy loss, have a larger interaction volume, and can be used to differentiate between high Z (atomic number) and low Z elements because the probability of the backscattering event is proportional to Z^2. This chemical sensitivity is offset by a decrease in resolution with the use of this method. Secondary electrons are created when an incoming electron interacts with conduction band electrons in a metal surface or valence electrons in semiconducting or insulating surfaces. The images produced from the detection of these

electrons have relatively high resolution and are more sensitive to topographic variations on the surface[3]. The strengths of secondary electron detection have made it the most common detection technique used in scanning electron microscopy.

SEM was used in Chapters 5, 6, and 7 for determining nanoparticle coverage and post-reaction morphological integrity. The SEM images used in this dissertation were taken at the Molecular Foundry at Lawrence Berkeley National Laboratory using a Zeiss Ultra 55 Field Emission SEM (Figure 3.3). Typical parameters were 6 kV acceleration voltage with a working distance of 7 mm.

3.2. Transmission Electron Microscopy

Transmission Electron Microscopy (TEM), like SEM, is a commonly used technique for imaging nanoparticles in the heterogeneous catalysis field. TEM offers improved resolution at the cost of specialized sample preparation. In TEM, an electron beam of 100-300 keV electrons is focused onto a sample by a series of electromagnetic lenses. The electron source and focusing lenses are very similar to those described previously for use in SEM. The most obvious difference is in the location of the detector, which is placed on the opposite side of the sample from the electron source so as to measure electrons which pass through the sample. TEM resolution is limited primarily by imperfections in the electron beam focus. Magnifications can reach as high as 10^6. A sample image is shown in Figure 3.4, below.

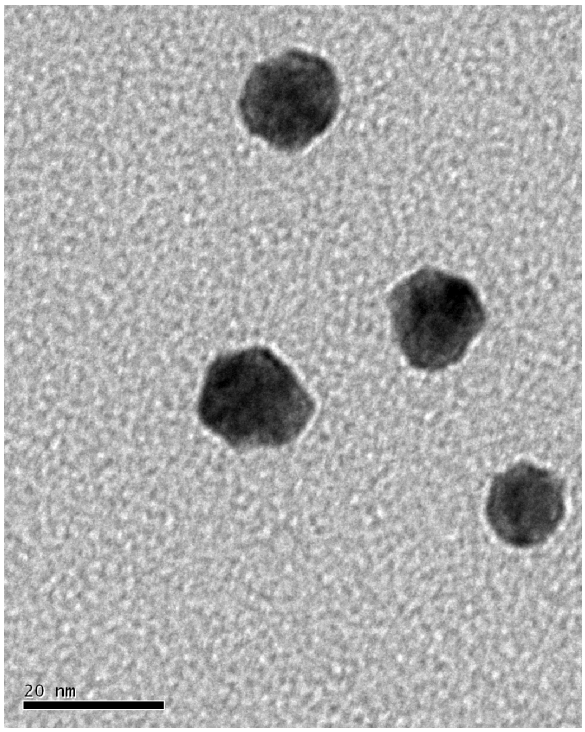

Figure 3.4 Transmission Electron Microscopy image of ~15 nm Rh nanoparticles

The two most common modes of imaging with TEM are bright field and dark field. In bright field, the image is constructed based on the difference in the number of electrons transmitted through the sample at each point. Variations in material composition, density, and thickness lead to electron beam attenuation, scattering, and interaction. A very dense, thick sample will permit no significant electron transmission and very thin, porous sample will permit

significant electron transmission, leading to a significant difference in image contrast. In dark field mode, the image is obtained from electrons which are diffracted from the sample. These electrons are detected slightly off-axis from the transmitted part of the electron beam. As with other diffraction techniques, dark field TEM emphasizes crystallinity within the sample and can be used to determine lattice structure. Lattice structure is particularly important for shape-dependent catalyst studies, in which the surface structure may affect the measured catalytic activity.

The most notable downside to TEM is that the sample must be supported on a specialized grid which permits maximum flux of the electron beam to the detector. These grids are typically composed of materials such as copper, molybdenum, gold, and platinum, with mesh size on the order of 1 – 100 m and thickness around 100 nm to ensure maximum electron transparency. Samples on silicon wafers, such as the nanodiodes discussed in Chapter 8, cannot be directly studied with TEM due to this electron transparency requirement, although many studies have been done using small amounts of supported catalyst[5].

TEM was used in Chapter 5 to determine particle shape and crystallinity and in Chapters 5, 6, and 7 to determine the particle size distribution. The TEM images used in this dissertation were taken at the Molecular Foundry at Lawrence Berkeley National Laboratory using a Philips FEI Tecnai 12 Transmission electron microscope (TEM) and Philips CM200/FEG high-resolution TEM (HRTEM). Typical acceleration voltages were 100 and 200 kV, respectively.

3.3. X-Ray Photoelectron Spectroscopy

X-Ray Photoelectron Spectroscopy (XPS) is a photon in, electron out surface-sensitive core-level spectroscopy used in these studies to determine surface elemental composition and oxidation state. This technique is sensitive to the first 0.5-2 nm of a surface, depending on the kinetic energy of the electrons being detected. The foundation of XPS is the photoelectric effect, which was first described by Einstein in 1905[6]. A sample is irradiated with enough energy to cause electron emission. The number of emitted electrons depends on the intensity of the incident light and the kinetic energy of the emitted electrons depends on the wavelength of the incident light. The basic setup used for XPS is presented in Figure 3.5.

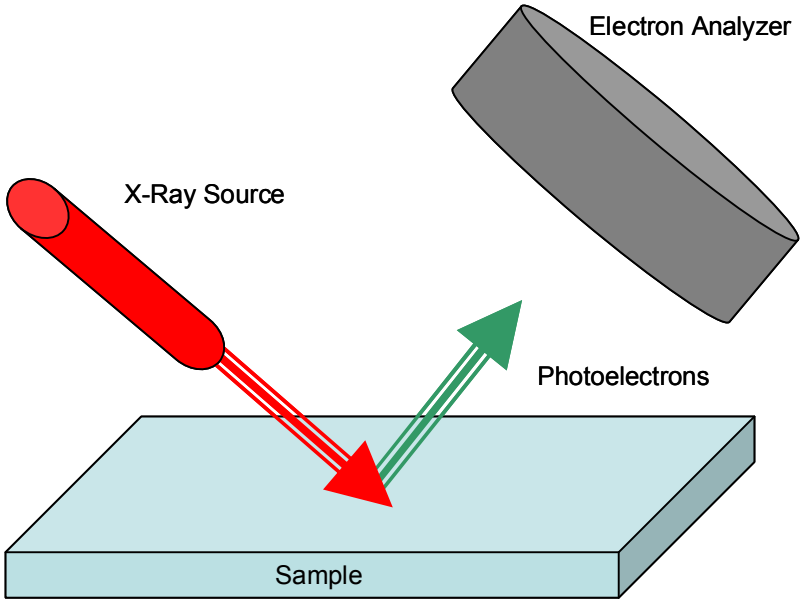

Figure 3.5 Basic scheme of generic XPS setup

In order for photoelectrons to be emitted, the energy of the light, hυ, must be greater than the sum of the electron binding energy within the atom, EB, and the workfunction of the spectrometer, Φ. Emitted photoelectrons are then detected and their kinetic energy, KE, is measured. The relationship between these factors can be described as

$$E_B = h\nu - KE - \Phi \quad (3.1)$$

Simple description of XPS energy relationships

The binding energy indicates the element and the specific energy level from which the electron originated. This equation, however, cannot be directly used to calculate the expected binding energy in real world systems. Several other factors complicate the picture. For instance, when an electron is emitted from a solid, an electronic rearrangement takes place in the solid which decreases the apparent binding energy. This decrease can be as much as 30 eV. Spin-orbit splitting causes some peaks to appear as doublets. In addition, XPS spectra commonly include Auger peaks and Fermi edges, both of which can be analyzed in order to obtain more information about a given sample. These additional complications can be accounted for by extending the basic XPS relationship described earlier to include specific factors for electronic relaxation, spin-orbit splitting, and other effects.

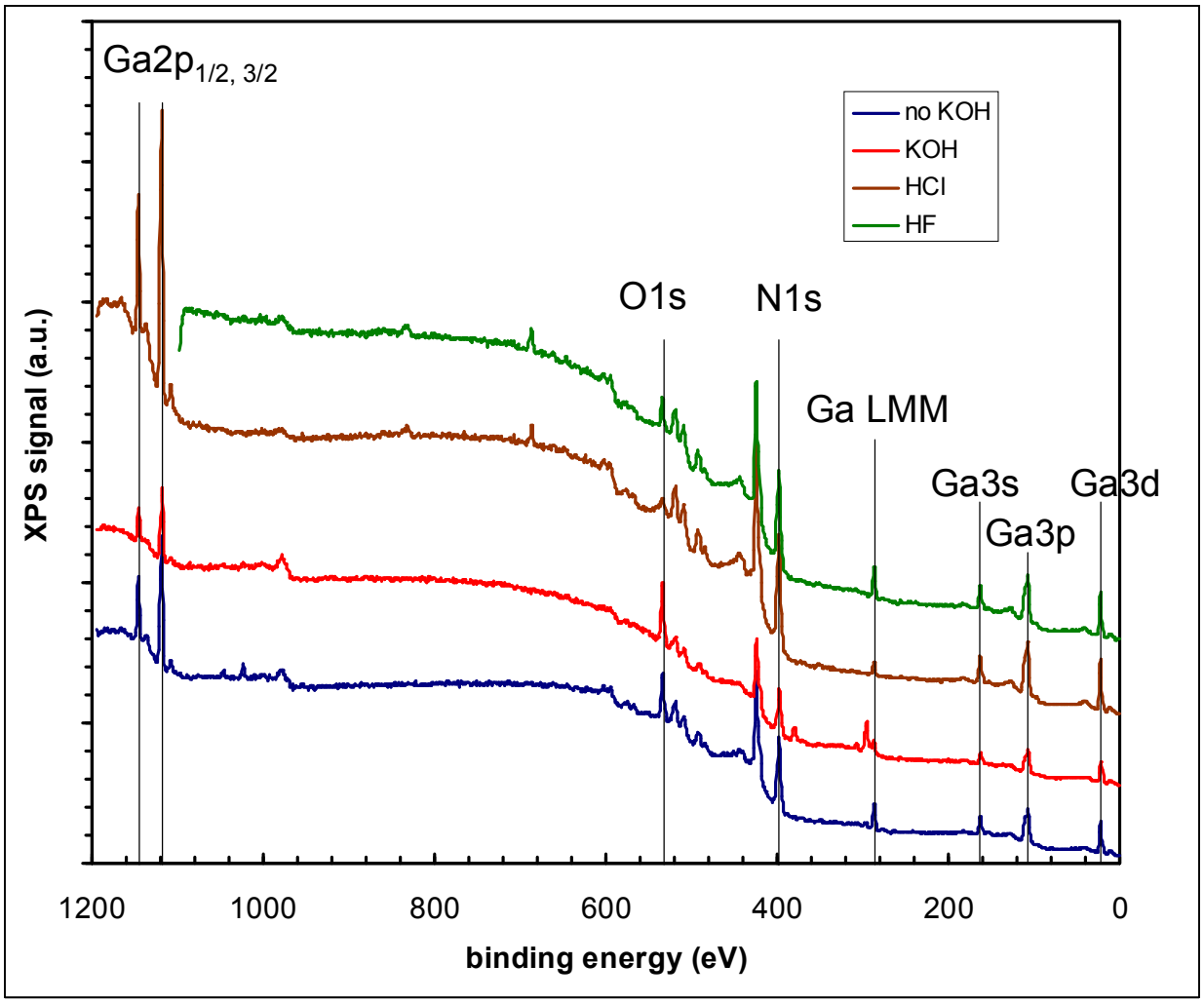

Figure 3.6 XPS Spectra taken from GaN after different surface treatments

The two major pieces of information derived from XPS experiments in the following studies are composition and oxidation state. Compositional analysis is carried out by comparing peak areas and looking for any relative changes. In order to compare peaks, the peaks must first be normalized using an atomic sensitivity factor. The atomic sensitivity factor is different for each peak for each element and accounts for a broad range of parameters, including the photoelectric cross section, detector efficiency, photon flux, orbital symmetry, the inelastic mean free path of the photoelectron, analyzer transmission efficiency, and the analysis area. These factors can be calculated independently, but are more often obtained from reference tables. Sample XPS spectra taken from a GaN surface are included in Figure 3.6.

Oxidation state is determined by examining peaks for any sort of shift in binding energy. When an atom is oxidized, the atom loses electron density. This deficit causes the remaining electrons to become more tightly bound to the positive atomic center and consequently increases the amount of energy required to remove an electron. Binding energy increases due to oxidation typically range from 0-4 eV. Oxidation state analysis can become very difficult when multiple

oxidation states are present for the same element in the sample. Other changes in the local chemical environment can also cause binding energy shifts.

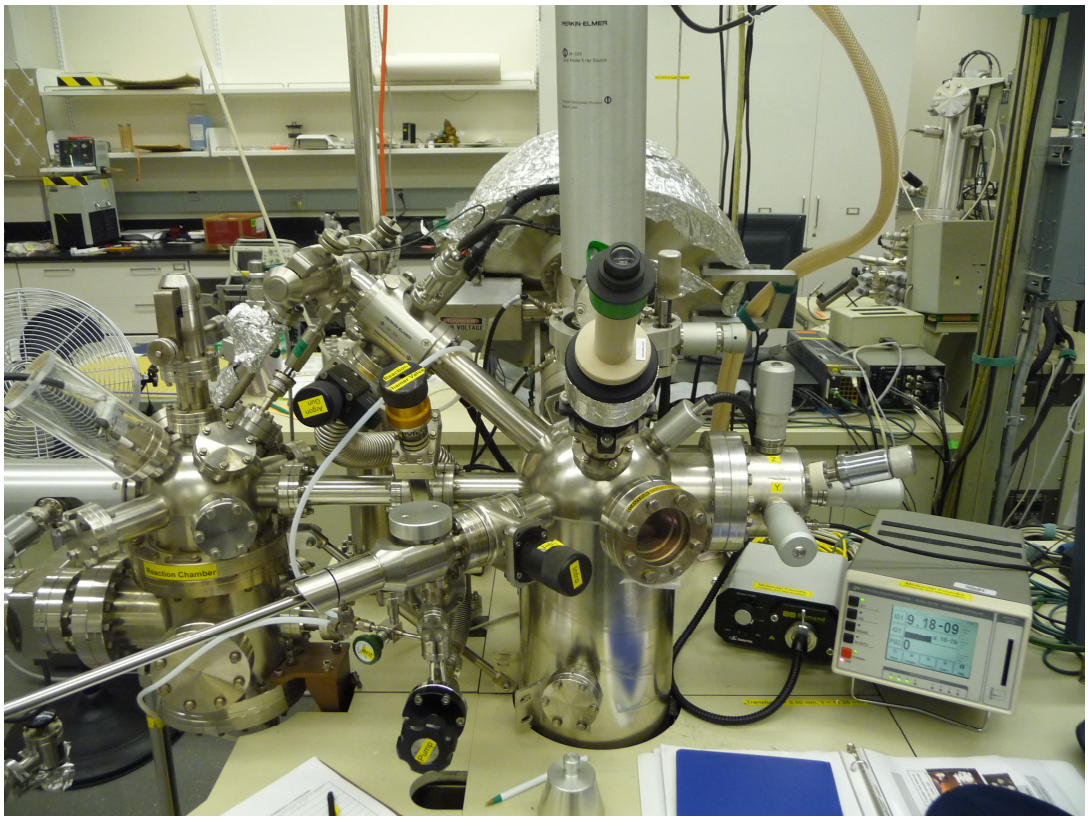

Figure 3.7 The XPS setup at Lawrence Berkeley National Laboratory's Molecular Foundry

The surface sensitive nature of XPS makes XPS ideal for examining samples with surface layers. These types of samples are ideal for depth-probe XPS, in which the inelastic mean free path of the photoelectrons is altered in order to control the effective probe depth in the range of 0.5-2 nm. Although the most common method of controlling the effective probe depth is to change the angle of the detector relative to the sample, this technique can lead to analytical complications and is not suitable for nanoparticle analysis due to their symmetry. A more effective mode of depth profiling is to change the photon energy of the light, hυ. Changing this energy directly affects the kinetic energy of the detected photoelectrons. For a given peak, when the photon energy is decreased, the photoelectron kinetic energy decreases by an equivalent amount. An electron with lower kinetic energy has lower mean free path, which prevents electrons from deeper in the sample from reaching the surface and being detected. In this manner, non-destructive depth profiling can be directly carried out on nanoparticle samples. In order to change the photon energy, it is necessary to use either multiple x-ray sources of different hυ or to use a Synchotron light source, such as the Advanced Light Source at Lawrence Berkeley National Laboratory. The Advanced Light Source also has two beamlines which have been specifically designed to run at relatively high gas pressures (~ 1 Torr) by using a series of differential pumping stages[7]. The Ambient Pressure X-Ray Photoelectron Spectroscopy (APXPS) beamline has been used to study nanoparticle catalysis *in-situ* during reaction[8].

XPS was used in Chapters 5, 6, 7, and 8 to determine elemental composition and oxidation state. The XPS used in this study was done at the Molecular Foundry at Lawrence

Berkeley National Laboratory using a Perkin-Elmer PHI 5300 XPS spectrometer with a position-sensitive detector, a hemispherical energy analyzer, and an Al-K_α x-ray source (Figure 3.7). APXPS was carried out at Beamline 9.3.2 at the Advanced Light Source at Lawrence Berkeley National Laboratory.

3.4. X-Ray Diffraction

In X-Ray Diffraction (XRD), x-ray photons of Å-scale wavelength interact with a solid sample to obtain information about the internal structure of the sample[9]. Diffraction of the photons in a periodic lattice of atoms can lead to constructive interference when the path difference between photons scattered from adjacent lattice planes is equal to an integer number of wavelengths. This angle can then be used to determine the distance between the two lattice places. Careful analysis of the resulting spectra can be used to identify bulk phases, characterize defects, estimate particle sizes, determine lattice constants, and establish composition.

The most common XRD setup consists of a fixed x-ray source and moveable detector, with the sample located between the two. The detector can be swept through a wide angle to measure x-ray intensity as a function of the angle 2θ between the incoming and diffracted x-ray beams. Most XRD setups use a CuK_α x-ray source, which has a wavelength of 1.54 Å.

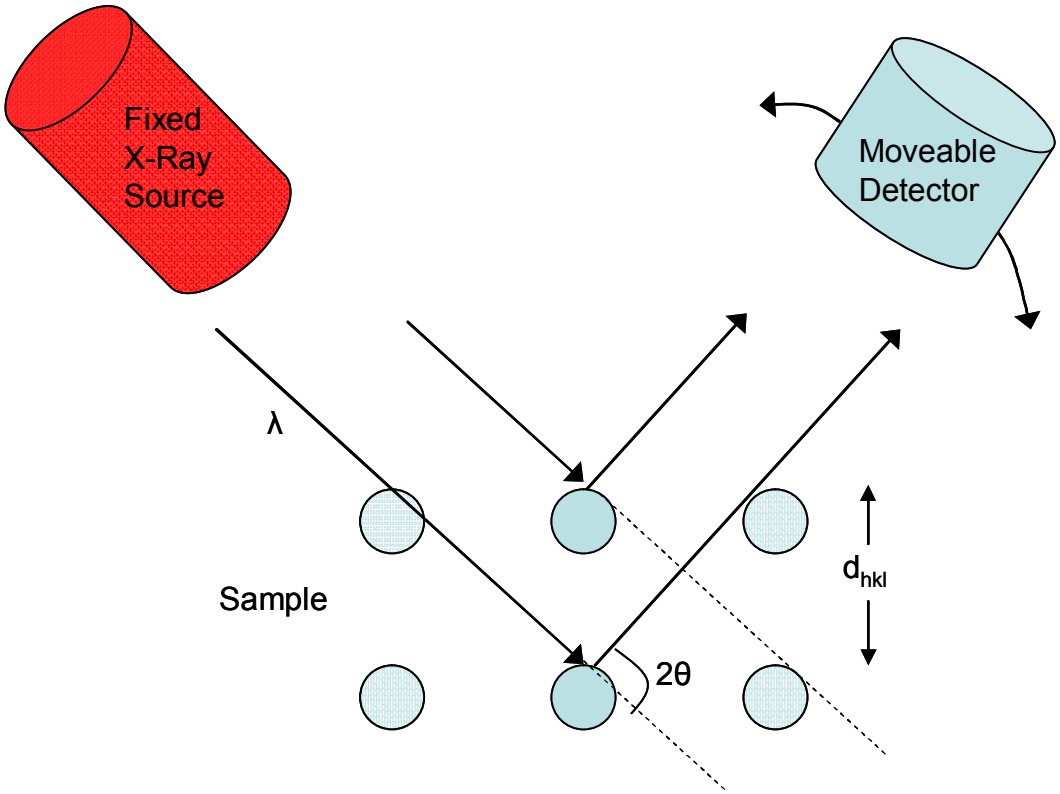

Figure 3.8 Common XRD Setup, including Bragg's law parameters. Peaks occur when the path length difference between photons is such that the photons interfere constructively rather than destructively.

X-ray diffraction requires constructive interference of radiation scattered throughout a crystalline sample with excellent long-range order. Photons scattered over a solid material are either scattered such that they satisfy the Bragg condition, in which case scattering is strong and constructive interference occurs through the mutual reinforcement of waves scattered along the

same direction, or are scattered such that they do not satisfy the Bragg condition and the randomly-scattered waves cancel each other out. The Bragg condition is $n\lambda = 2d_{hkl}\sin(\theta)$, where n is a positive integer, λ is the x-ray photon wavelength, d_{hkl} is the distance between two lattice planes, and θ is the angle between incoming x-rays and the reflecting lattice plane[10]. The basic setup and conditions are diagrammed in Figure 3.8. Different crystal phases and materials can be identified by their characteristic XRD patterns, which come about from the Bragg condition. Amorphous materials, such as TiO_x deposited at low temperature, have no diffraction peaks, whereas the same material can have very clear diffraction peaks after annealing to promote crystallization. An example of this application is shown in Figure 3.9.

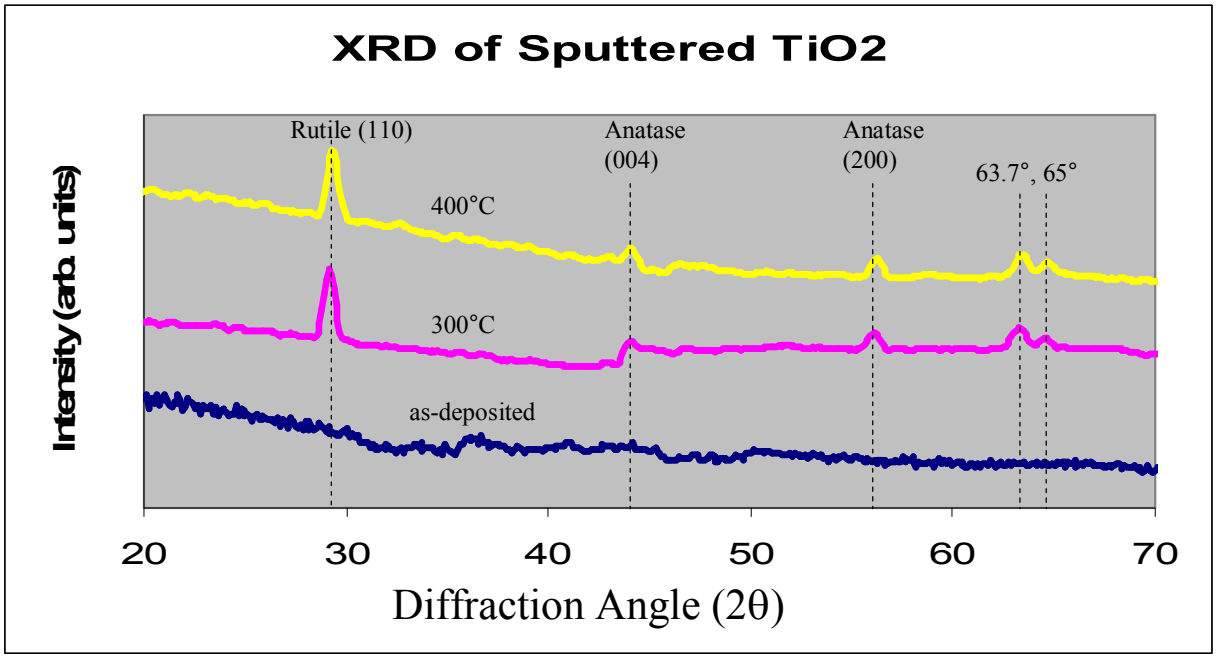

Figure 3.9 XRD spectra of a sputter-deposited 150 nm TiO_2 thin film before and after annealing in oxygen. The film is completely amorphous as-deposited, but shows evidence of Rutile and Anatase crystal phases after annealing.

The Bragg condition, however, assumes a sample of perfect order and infinite span penetrated by perfectly monochromatic radiation. In reality, defects and spatial limitations are the order of the day. The finite size of nanoparticles and thin films prevents some scattered waves which do not meet the Bragg condition from being canceled out, or destructively interfered with. This finite-size effect leads to broadening of the diffraction peaks. Smaller nanocrystals have wider peaks. This phenomenon can actually be used to determine nanoparticle size in the range of 5-50 nm[11].

This technique does have some disadvantages. The primary issue is that XRD requires long-range order to have measurable diffraction. This requirement prevents the technique from being used to measure very small cluster-like nanoparticles or from obtaining information from any amorphous media. Used in the right context, however, XRD can play a very important role in nanoparticle characterization and analysis.

XRD was used in Chapters 5, 6, and 7 to determine nanoparticle shape and lattice constants. XRD was also used in Chapter 8 to determine TiO_x crystallinity. The XRD used in this

dissertation was done at the University of California, Berkeley, using a Bruker D8 GADDS diffractometer using Co-Kα radiation.

3.5. Current-Voltage Curves

Current-Voltage Curves (IV curves) were used to determine the Schottky barrier height of Rh/TiO_x and Rh/GaN catalytic nanodiodes used to study hot electron detection in catalysis. This technique is simple to implement, as it requires only a voltage source and current measurement. Schottky barrier height is a crucial measure for hot electron detection because it determines the amount of energy an electron must possess in order to successfully transport from the catalytic metal to the wide-bandgap semiconductor. If the Schottky barrier is too high, no hot electrons in the system will have enough energy to surmount the barrier and reach the semiconductor. If the Schottky barrier is too low, too many thermally excited electrons will have sufficient energy to surmount the Schottky barrier and it will be impossible to distinguish between chemically-excited hot electrons and thermally-excited electrons. A sample IV curve is given in Figure 3.10.

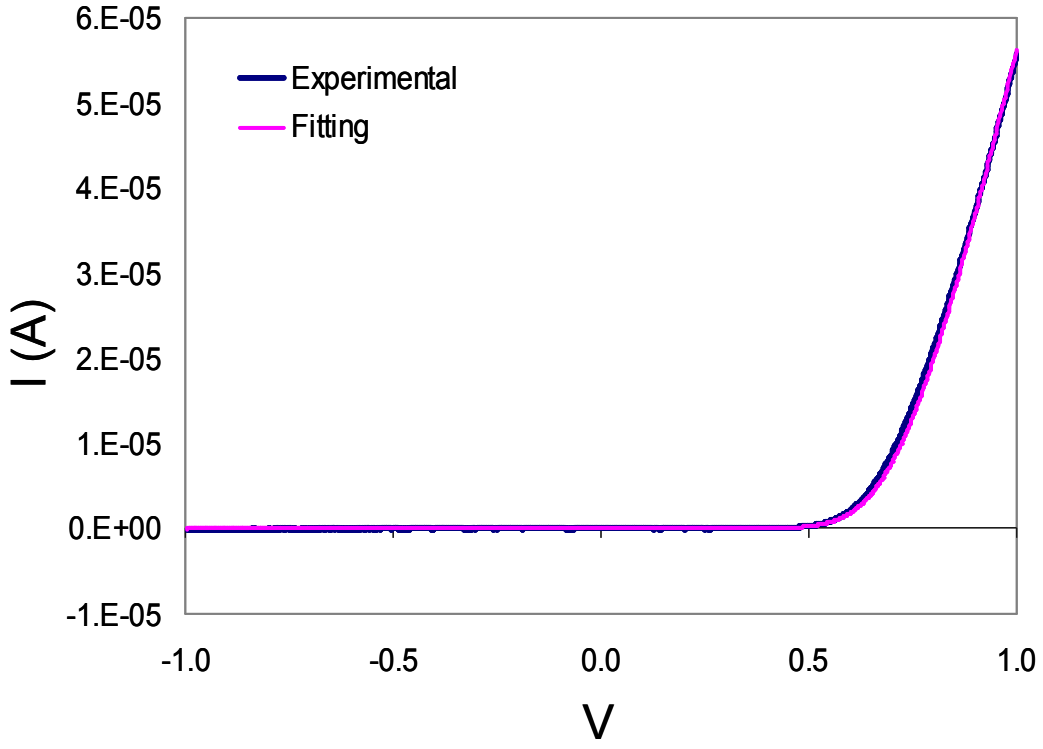

Figure 3.10 Current-Voltage Curve from Pt/TiO_2 Catalytic Nanodiode

There are four primary mechanisms for electron transport in a metal-semiconductor junction. The processes are: transport over the Schottky barrier, quantum tunneling through the Schottky barrier, electron-hole recombination in the band-bending region, and electron-hole recombination in the neutral region due to hole-injection from the metal[12]. Other mechanisms for electron transport include leakage through the contact periphery due to enhanced electromagnetic

fields at sharp features, such as a corner or edge, and leakage through interface states and charge trapping in the interfacial region where the semiconductor and metal meet[12].

The IV behavior of metal-semiconductor Schottky contacts is best described using Thermionic Emission-Diffusion theory. This theory describes the behavior as:

$$I = FA^{**}T^2 \exp(-\frac{\phi_B}{k_B T})\left[\exp(\frac{q(V - IR_S)}{\eta k_B T}) - 1\right] \quad (3.2)$$

Thermionic Emission equation

where I is current, F is area, A** is the effective Richardson constant, T is temperature, q is the magnitude of the electrical charge on an electron, k_B is the Boltzmann constant, Φ_B is the Schottky barrier height, V is the applied bias, R_S is the series resistance, and η is the ideality factor[13]. The effective Richardson constant is a material-dependent factor that accounts for the probability of an electron being backscattered by electron optical-phonon scattering, the probability of quantum-mechanical reflection or tunneling, electron thermal velocity, effective diffusion velocity, the difference in masses between light and heavy holes, and other factors. The experimental IV curve can be fit to this equation using η, Φ_B, and R_S as parameters. The Schottky barrier height is assumed to be the value of Φ_B for the best available fit.

Other methods to measure barrier heights include activation energy plots, capacitance-voltage measurement, and photoelectric measurement. Activation energy plots are derived from IV curves measured at a series of temperatures, typically between 150°C and room temperature. This method works because Φ_B and A** can be assumed to be relatively independent of temperature in this range. Capacitance-voltage measurement determines barrier height by superimposing a small ac bias on a dc bias. This induces opposite charges at the interface and can be used to probe charge trapping and donor levels within the device. Photoelectric measurement is based on the photoexcitation of electrons. Assuming sufficient photon absorption in the metal, the barrier height is equivalent to the minimum photon energy necessary to excite metal electrons over the Schottky barrier such that significant photoelectric current is measured.

IV curves were used in Chapter 8 to determine the Schottky barrier height of the catalytic nanodiodes in different gas compositions. The IV curves were taken from -1 V to +1 V *in situ* using a Keithley 2400 Sourcemeter controlled by LabTracer 2 software.

3.6. References

1. McMullan, D., The Early Development of the Scanning Electron Microscope. In *Biological Low-Voltage Scanning Electron Microscopy*, 2008; pp 1-25.
2. Everhart, T. E., Persistence pays off: Sir Charles Oatley and the scanning electron microscope. *J. Vac. Sci. Technol. B* **1996,** *14* (6), 3620-3624.
3. Contreras, A. M. Nanolithographic Fabrication and Heterogeneous Reaction Studies of Two-Dimensional Platinum Model Catalyst Systems. Lawrence Berkeley National Laboratory, Berkeley, 2006.
4. Janssen, G. How does an EM work? (TEM-FESEM). http://www.vcbio.science.ru.nl/en/fesem/info/principe/.

5. Datye, A. K., Electron microscopy of catalysts: recent achievements and future prospects. *Journal of Catalysis* **2003,** *216* (1-2), 144-154.
6. Einstein, A., Generation and conversion of light with regard to a heuristic point of view. *Ann. Phys.-Berlin* **1905,** *17* (6), 132-148.
7. Salmeron, M.; Schlogl, R., Ambient pressure photoelectron spectroscopy: A new tool for surface science and nanotechnology. *Surface Science Reports* **2008,** *63* (4), 169-199.
8. Tao, F.; Grass, M. E.; Zhang, Y. W.; Butcher, D. R.; Renzas, J. R.; Liu, Z.; Chung, J. Y.; Mun, B. S.; Salmeron, M.; Somorjai, G. A., Reaction-Driven Restructuring of Rh-Pd and Pt-Pd Core-Shell Nanoparticles. *Science* **2008,** *322* (5903), 932-934.
9. Niemantsverdriet, J. W., *Spectroscopy in Catalysis*. VCH: Weinheim, 1993.
10. Klug, H. P., Alexander, L.E., *X-Ray Diffraction Procedures*. Wiley: New York, 1954.
11. Cullity, B. D., *Elements of X-Ray Diffraction*. 2nd ed.; Addison Welsey: Reading, 1978.
12. Sze, S. M., *Physics of Semiconductor Devices*. 2nd ed.; Wiley: New York, 1981.
13. Park, J. Y.; Renzas, J. R.; Hsu, B. B.; Somorjai, G. A., Interfacial and Chemical Properties of Pt/TiO2, Pd/TiO2, and Pt/GaN Catalytic Nanodiodes Influencing Hot Electron Flow. *The Journal of Physical Chemistry C* **2007,** *111* (42), 15331-15336.

Chapter 4. Measurement Techniques

The work presented here includes the *in-situ* measurement of catalytic reaction rates using two approaches. The first of these approaches, Gas Chromatography, is well-known to nearly all chemists. The second of these approaches is a novel approach to the measurement of reaction rate in which hot electrons produced by chemical reaction on the catalyst surface are detected and correlated to catalytic activity. Both techniques were available in the reaction chamber used for these studies, but hot electron detection could only be used for nanodiode studies because of the unique diode structure necessary to detect catalytic activity in this way.

4.1. Gas Chromatography

4.1.1. Gas Chromatography

Gas chromatography (GC) is one of the work-horses of modern catalysis research. It is used to separate and detect gases. This technique has played an important role in research done in fields such as catalysis, food contaminants, pollution analysis, biochemistry, and the petrochemical industry. GC was originally invented by A.T. James and A.J.P. Martin in the early 1950s[1]. Their earliest-published work was on the separation of fatty acids in 1952[2]. The modern GC essentially consists of a long column, sometimes 10 meters or more, placed in an oven and connected to a detector. In this simple setup, the column determines gas separation, the oven is used to control column temperature, which can increase or lower retention time and prevent complete condensation onto the column, and the detector measures the amount of analyte that is exiting the column at any given moment. A series of switching valves and stainless steel connections are used to control sampling and carrier gas backpressure. Data is collected as the intensity of the detector signal versus time. A photograph of a gas chromatograph from the 1980s is included in Figure 4.1.

Figure 4.1 HP 5890 Series II Gas Chromatograph commonly used for kinetic measurements

Column selection is crucial to successful gas chromatography measurements. The right column can make the difference between clean, narrow, well-separated peaks with low retention times and asymmetric, overlapping peaks with poor signal-to-noise and long retention times. In some cases, multiple columns are used in serial or parallel in order to facilitate efficient separation. A wide variety of GC columns exist. The major categories are packed columns and capillary columns. Packed columns are filled with particles which have been coated with a stationary phase, which is generally liquid or elastomeric. The major disadvantage of packed columns is that the non-linear path has high resistance to gas flow, which leads to longer retention times for the same separation as compared to capillary columns. Capillary columns consist of a very thin open tube in which the inner walls of the tube have been coated by a stationary phase. These columns have higher separation efficiency but are more susceptible to sample overloading. A packed column properly connected inside a GC oven is shown in Figure 4.2.

Figure 4.2 Packed column inside the oven of a GC.

Many types of detectors are used in GC, including flame ionization detectors (FID), thermal conductivity detectors (TCD), electron capture detectors (ECD), photoionization detectors (PID), atomic emission detectors (AED), and more. Choice of detector is based on sensitivity to the analytes in question. Some studies require multiple detectors in order to accurately measure all products. The two detectors most commonly used in the Somorjai group laboratories are FID and TCD. FID uses a hydrogen/air flame to burn hydrocarbon analytes. The burnt analytes produce ions that are attracted to a biased cathode and detected as current with a sensitivity on the order of 2 picograms per second. FID is not effective for the detection of molecules such as O_2, CO, NO, CO_2, N_2, and N_2O, however, which are the analytes of interest in the studies presented in this work. These analytes were detected using TCD. TCD works by flowing the analyte over a heated filament. When gas with a thermal conductivity that differs from the baseline (typically established from He reference gas) passes over the filament, the potential across the filament changes. The new potential is compared with that from the He reference gas. The difference between the two is converted into the electrical signal.

In this report, product accumulation is presented in terms of the turnover frequency (TOF), which is measured as product molecules produced per metal site per second. This metric is common in the catalysis literature and enables quantitative comparison of product formation for different samples at the same temperature.

All gas chromatography was done using a HP 5890 Series II GC using a molecular sieve packed column in parallel with a Hayesep D packed column both connected to one TCD.

4.1.2. Reaction Chamber

Reactions were carried out in a batch mode on 2D samples in a stainless steel 1 L chamber consisting of a ceramic heater connected to gold-plated leads. A diagram and photograph of the setup are included in Figures 4.3 and 4.4, respectively. Temperature was measured with a Type-K thermocouple mounted on a small piece of silicon wafer on the heater. The thermocouple was mounted in this way to minimize the disparity between the measured

temperature and the temperature on the sample surface without requiring frequent remounting of the thermocouple. The heater leads were hollow and connected to each other with a hollow electrical break such that compressed air was able to flow through both leads to cool them and prevent unwanted background reaction on the surface of the leads. Prior to each reaction, the chamber was pumped to UHV (typically 10^{-7} Torr, although pumping overnight decreased that to 10^{-8} Torr) with a turbomolecular pump in order to remove unwanted gas-phase contaminants. A gate valve between the turbomolecular pump and the main chamber was then closed and the chamber was then refilled from a gas manifold with reactants and carrier gas to a total pressure of 1 atmosphere. Carrier gas was always put into the chamber last and gases were allowed to mix at room temperature for 30 minutes to ensure adequate mixing.

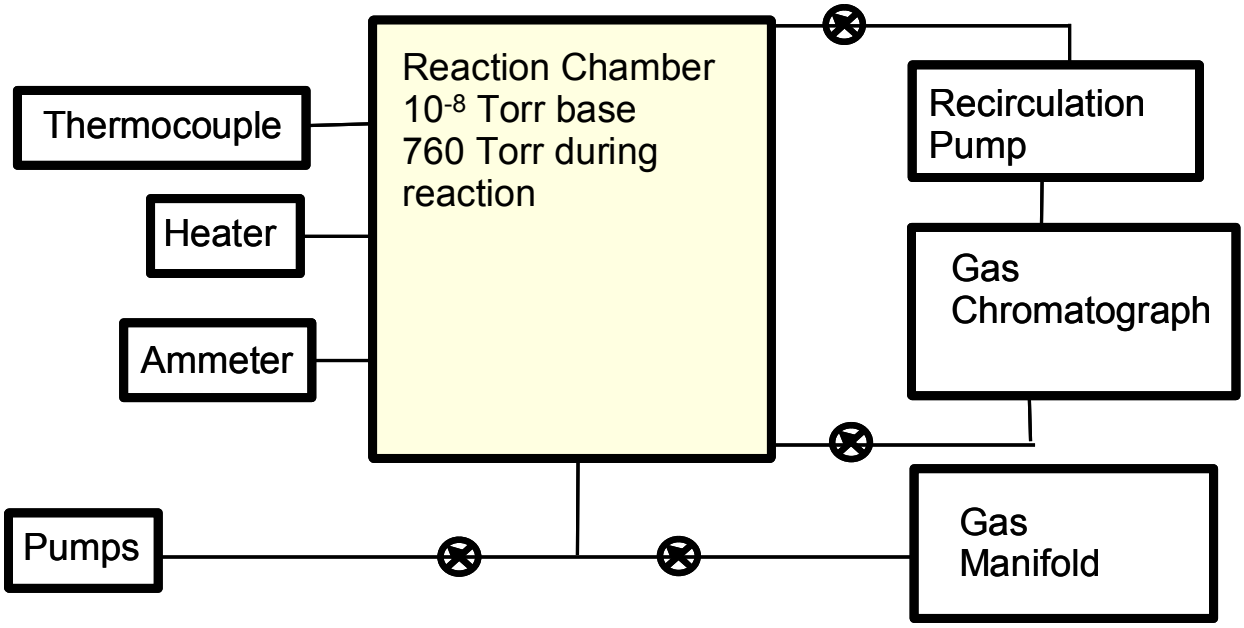

Figure 4.3 Diagram of reaction setup used for both kinetic and chemicurrent measurements

The gas mixture was circulated using a recirculation pump located between the chamber and the two-position 10-way valve used to sample the reaction mixture into the GC. Pressures were measured with an ion gauge on the turbomolecular pump side of the gate valve for low pressure (below 10^{-4} Torr) and a 1000 Torr range Baratron gauge mounted in the main reaction chamber for accurate measurement of reactant and carrier gas pressures from 0.1-1000 Torr. Electrical measurements were carried out on nanodiode samples with gold wire leads connected to the ohmic pads of the diodes by squeezing the leads between the pads and a ceramic Makor washer and tightening the washer with a gold-plated screw. The gold wires were connected outside the chamber using BNC electrical feedthroughs. On the air side of the chamber, electrical connections were made using a low-noise triax cable connected to a Keithley 6487 picoammeter for current measurement or to a Keithley 2400 sourcemeter for IV curve characterization.

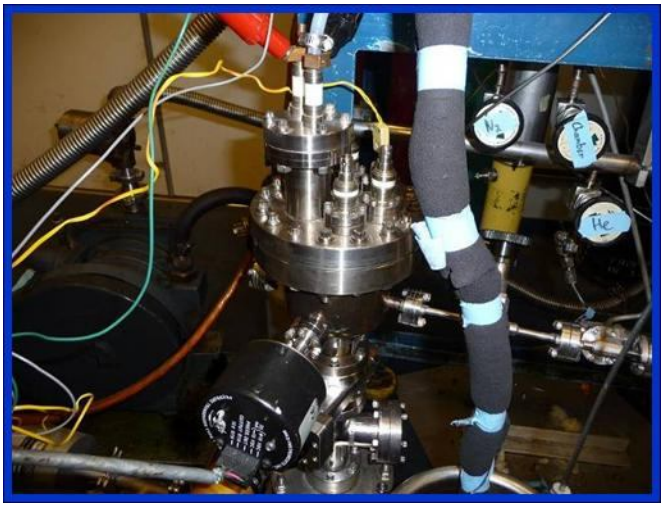

Figure 4.4 Photograph of the 1 L reactor used for kinetic and hot electron studies

4.2. Hot Electron Measurement

In situ current measurements consist of two components: a reaction-driven hot electron current and a heat-driven thermoelectric current. The real chemicurrent is the reaction-driven hot electron component. In order to detect this component, the thermoelectric current must be independently measured and then separated from the overall current in reaction. In this section, we will discuss these two components and how they influence hot electron measurement.

4.2.1. Thermoelectric Current

Thermoelectric current generation in the catalytic nanodiode is due to multiple sources. These sources include current due to temperature gradients within the device and thermionic emission within the device. These sources result from the *in-situ* heating of the device and are also influenced by heat deposited on the device by exothermic reaction events during the catalytic process. Although perhaps not obvious at first glance, significant temperature gradients exist during reaction because of the geometry of the system. As noted in Section 4.1.2 and also visible in Figure 4.5, during reaction the device is heated from below by a boronitride heater (GE Advanced Ceramics, HT-01) and effectively cooled from above by the mixture of gases being flowed through the reaction chamber and through the sampling loop of the Gas Chromatograph by a recirculation pump. This geometry is unavoidable in the case of a planar device over which reaction gas must flow for proper kinetics. The result is a non-equilibrium system with a small difference in temperature between the semiconductor and the metal ohmic and Schottky contact layers deposited on top of the semiconductor. At elevated temperatures, the electron energy distributions on the cold and hot areas of the device differ and as a result, electrons move from the hot area to the cold area in an attempt to reach equilibrium. The result is diffusion current due to the movement of electrons. In the case where the temperature gradient is fixed, as in the reactor in question, a potential difference develops between the two regions of the device, with the potential at the hot end lowering and the potential at the hot end rising. The magnitude and even direction of this potential depends on the Seebeck coefficient. As an example, the Seebeck coefficient in TiO_2 is 0.4mV/K at 300°C and the Seebeck coefficient of GaN is -0.05 mV/K at 300K[3]. This effect is called the Seebeck Effect and contributes directly to the thermoelectric current measured in the device[4].

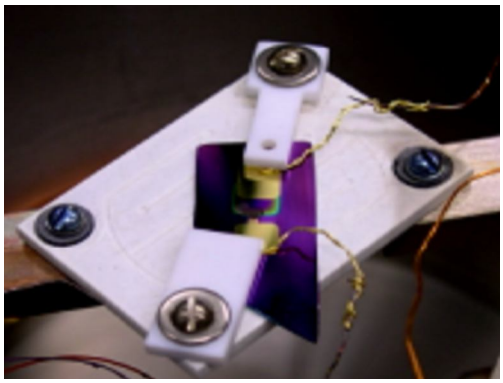

Figure 4.5 Nanodiode mounted for current measurement

Thermionic emission within the device is the second major factor in determining the overall level of thermoelectric current. For $T > 0$ K, electrons in the conduction band of the semiconductor can sometimes have enough energy to surmount the Schottky barrier and cross over into the metal. Although the barrier height as measured from IV curves is typically high enough to prevent this from happening, local inhomogeneities in the metal-semiconductor interface can lead to local minima in the Schottky barrier height. The presence of these local minima implies that the Schottky barrier height cannot be viewed directly as the cut-off energy below which no electrons may pass. As the upper end of the electron energy distribution increases exponentially with temperature, current transport across the barrier increases as well.

At high enough temperature, a Schottky barrier of any height becomes effectively ohmic due to the large concentration of electrons with energy sufficient to cross over the Schottky barrier. This problem is not nearly as significant in reactions at relatively low temperature[5] as it is in reactions at relatively high temperature[3]. In order to mitigate this effect, the barrier height should be as high as possible so as to lower the flux of thermally excited electrons over the barrier[6].

Another factor in the thermoelectric current is heat transfer to the catalyst surface from the exothermic reaction. The surface temperature change due to this factor can be calculated as

$$\Delta T = R_{TOF} NEd / k \tag{4.1}$$

Temperature Change due to exothermic reaction on surface

where ΔT is the temperature change, R_{TOF} is the turnover frequency, N is the surface site density, E is the energy gain per reaction event, d is the layer thickness, and k is the thermal conductivity. Assuming turnover frequencies are of the order of 10^3 product molecules per site per second, with site density of 10^{13} sites/mm^2, energy gain per reaction event of ~3.1 eV (5×10^{-19} J), then for a catalytic metal layer of 5 nm thickness and with thermal conductivity of ~100 W/(meter-K), the temperature change on the surface is only 3×10^{-7} K. For the TiO_2 layer, with thickness of 150 nm and thermal conductivity of 3.3 W/(meter-K), the temperature change is 2×10^{-4} K[7]. These contributions to thermoelectric current are negligible in a process in which reaction temperature is typically ~500 K and the heater feedback loop is only stable to within several tenths of a Kelvin.

4.2.2. Chemicurrent Measurement

Overall chemicurrent depends directly on the hot electron yield, which is the number of hot electrons measured per reaction event. The process by which a hot electron generated by a chemical reaction event is measured is comprised of three sequential steps: (a) injection of the hot electron into the metal thin film; (b) ballistic transport of the hot electron across the metal film, taking into account attenuation and the inelastic mean free path; (c) transmission of the hot electron over/through the Schottky barrier[8]; and (d) transport from the semiconductor to the ammeter, during which losses may occur within the semiconductor, ohmic pad, or even within the ammeter. Hot electron yield depends on the efficiency of these steps.

Step (a), hot electron injection, has been studied recently for the CO oxidation by O_2 reaction by our collaborators, Sergey Maximoff and Martin Head-Gordon[9]. In their work, they found that the yield depends on the exact nature of the reaction transition state and, specifically, the mechanism by which the $CO_2^{\delta-}$ reaction product desorbs and dissociates into $CO_2 + \delta e^-$. They also determined that this desorption process implies a power-law relationship between the measured chemicurrent and the heat of adsorption with an exponent of 2.66. Maximoff and Head-Gordon also postulated that their analysis may be extendable to a variety of other oxidation-reduction reactions on similar high work-function catalytic metal surfaces.

Step (b) of the above process, ballistic transport of hot electrons across the metal film, can be considered as a factor of attenuation in the metal film and the related inelastic mean free path of the hot electron. Attenuation can be described using Beer's law. In the context of the ballistic transport of hot electrons through a metal film, Beer's law can be written as

$$A(E_{ex}, \mathbf{k}) \approx \exp(-\frac{d}{\lambda_B(E_{ex})\cos\theta}) \quad (4.2)$$

Attenuation of a hot electron through a metal thin film

where A is attenuation or absorption, d is the metal film thickness, λ_B is the attenuation length, E_{ex} is the excess energy of the hot electron above the Fermi level (e.g. $E_{ex} = E - E_F$), and θ is the angle at which the hot electron is injected[6]. λ_B depends on both the quasi-elastic mean free path due to electron-phonon scattering, λ_{el}, and the inelastic mean free path due to electron-electron scattering, $\lambda_{e\text{-}e}$. However, electron-electron scattering is the dominant process in the determination of the excess energy dependence of λ_B. The inelastic mean free path due to electron-electron scattering can be described as

$$\lambda_{e-e} \cong \upsilon_{el} \cdot \tau_{e-e} \propto \frac{\sqrt{E_{ex} + E_F}}{E_{ex}^2} \quad (4.3)$$

Inelastic mean free path due to electron-electron scattering

where υ_{el} is the velocity of the excited electrons, $\tau_{e\text{-}e}$ is the lifetime of the excited electrons, E_{ex} is the excess energy of the electrons above the Fermi level, and E_F is the Fermi level[6]. This model does not account for band structure effects, amplification due to electron-electron scattering at energies far enough above the Fermi level such that both scattered electrons still have energy sufficient to transport through the metal, reflections at the metal-surface and metal-semiconductor interfaces, or issues related to film crystallinity.

Transport of the hot electron over the Schottky barrier, step (c) above, may occur through a few basic processes. These processes are: transport over the Schottky barrier; quantum-mechanical tunneling through the Schottky barrier, particularly in the energy regime near the top of the barrier at which point the barrier is relatively thin; recombination of electron-hole pairs in the space-charge region; injection of holes from the metal to the semiconductor in the neutral region; injection of current through traps in the interfacial region between the metal and semiconductor; and current leakage at the edge of the metal-semiconductor contact due to relatively high electric fields at the boundary[10]. Similarly, internal efficiencies within the semiconductor may affect step (d) as well. Current may be attenuated by the recombination of electron-hole pairs within the semiconductor depletion region and may actually be amplified if the incident hot electron has enough excess energy to ionize the semiconductor through the impact ionization process[6]. These complex processes are difficult to model accurately within the context of a non-ideal ultra thin-film device at relatively high temperature (~500 K) during catalytic reaction or in oxidizing or reducing conditions. However, great efforts have been taken to model these processes[6, 8-19] and it is hoped that these efforts may soon provide effective, reliable approaches to determining the efficiency of each individual step in the hot electron detection process such that directed efforts can be made to improve device performance in each area.

In order to experimentally determine the hot electron current, current must be measured on the device in reaction and under thermoelectric conditions at similar temperatures and pressures and with the device barrier height kept relatively constant. Current is measured in a variety of conditions and the barrier height is calculated from IV curves taken in each condition (see Section 3.5). The hot electron chemicurrent is the current due exclusively to hot electrons and not to thermoelectric effects. This current is taken as the difference between the current in

reaction and the current in thermoelectric conditions at the same temperature. Thermoelectric current is measured most accurately when the device is in similarly oxidizing or reducing conditions as during the measurement of current in reaction because this ensures a similar barrier height for the two measurements. All currents are collected on a Keithley 6487 Picoammeter controlled by the Keithley ExceLINX program and connected to the device via low-noise triax cables, BNC electrical feedthroughs, and gold wiring within the chamber. Contact to devices was made by clipping the gold wires tightly to the device contact pads. Chemicurrent measurement results are presented in Chapter 8.

4.3. References

1. Bartle, K. D.; Myers, P., History of gas chromatography. *Trac-Trends in Analytical Chemistry* **2002,** *21* (9-10), 547-557.
2. James, A. T.; Martin, A. J. P., GAS-LIQUID PARTITION CHROMATOGRAPHY - THE SEPARATION AND MICRO-ESTIMATON OF VOLATILE FATTY ACIDS FROM FORMIC ACID TO DODECANOIC ACID. *Biochemical Journal* **1952,** *50* (5), 679-690.
3. Park, J. Y.; Renzas, J. R.; Hsu, B. B.; Somorjai, G. A., Interfacial and Chemical Properties of Pt/TiO2, Pd/TiO2, and Pt/GaN Catalytic Nanodiodes Influencing Hot Electron Flow. *The Journal of Physical Chemistry C* **2007,** *111* (42), 15331-15336.
4. Werheit, H.; Kuhlmann, U.; Herstell, B.; Winkelbauer, W., Reliable measurement of Seebeck coefficient in semiconductors. *Journal of Physics: Conference Series* **2009**, 012037 (5 pp.).
5. Hervier, A.; Renzas, J. R.; Park, J. Y.; Somorjai, G. A., Hydrogen Oxidation-Driven Hot Electron Flow Detected by Catalytic Nanodiodes. *Nano Lett.* **2009,** *9* (11), 3930-3933.
6. Nienhaus, H., Electronic excitations by chemical reactions on metal surfaces. *Surface Science Reports* **2002,** *45* (1-2), 3-78.
7. Park, J. Y.; Renzas, J. R.; Contreras, A. M.; Somorjai, G. A., The genesis and importance of oxide-metal interface controlled heterogeneous catalysis; the catalytic nanodiode. *Topics in Catalysis* **2007,** *46* (1-2), 217-222.
8. Gadzuk, J. W., On the detection of chemically-induced hot electrons in surface processes: from X-ray edges to schottky barriers. *J. Phys. Chem. B* **2002,** *106* (33), 8265-8270.
9. Maximoff, S. N.; Head-Gordon, M. P., Chemistry of fast electrons. *Proceedings of the National Academy of Sciences of the United States of America* **2009,** *106* (28), 11460-11465.
10. Sze, S. M., *Physics of Semiconductor Devices*. 2nd ed.; Wiley: New York, 1981.
11. Bottcher, A.; Imbeck, R.; Morgante, A.; Ertl, G., NONADIABATIC SURFACE-REACTION - MECHANISM OF ELECTRON-EMISSION IN THE CS+O-2 SYSTEM. *Physical Review Letters* **1990,** *65* (16), 2035-2037.
12. Campillo, I.; Silkin, V. M.; Pitarke, J. M.; Chulkov, E. V.; Rubio, A.; Echenique, P. M., First-principles calculations of hot-electron lifetimes in metals. *Physical Review B* **2000,** *61* (20), 13484-13492.
13. Kharlamov, F. V.; Kharlamov, V. F., Transmission of hot electrons through a metal-semiconductor interface. *Semiconductors* **2009,** *43* (1), 42-46.
14. Kharlamov, V. F.; Kostin, A. V.; Kubyshkina, M. V.; Kharlamov, F. V., Metal-to-semiconductor emission of hot electrons excited on catalytic reaction. *Semiconductors* **2008,** *42* (1), 59-66.

15. Monch, W. In *Barrier heights of real Schottky contacts explained by metal-induced gap states and lateral inhomogeneities*, Papers from the 26th conference on the physics and chemistry of semiconductor interfaces, San Diego, California (USA), AVS: San Diego, California (USA), 1999; pp 1867-1876.
16. Norskov, J. K., Dynamical aspects of electronic structure during adsorption. *Journal of Vacuum Science and Technology* **1981,** *18* (2), 420-426.
17. Trail, J. R.; Bird, D. M.; Persson, M.; Holloway, S., Electron-hole pair creation by atoms incident on a metal surface. *Journal of Chemical Physics* **2003,** *119* (8), 4539-4549.
18. Trail, J. R.; Graham, M. C.; Bird, D. M.; Persson, M.; Holloway, S., Energy loss of atoms at metal surfaces due to electron-hole pair excitations: First-principles theory of "chemicurrents". *Physical Review Letters* **2002,** *88* (16).
19. Werner, J. H.; Guttler, H. H., Barrier inhomogeneities at Schottky contacts. *J. Appl. Phys.* **1991,** *69* (3), 1522-1533.

Chapter 5. Rh Nanoparticle Shape Dependence in CO Oxidation by NO

The shape dependence of the catalytic reduction of NO by CO on Rhodium nanopolyhedra and nanocubes was studied from 230 – 270°C. The nanocubes are found to exhibit higher turnover frequency and lower activation energy than the nanopolyhedra. These trends are compared to previous studies on Rh single crystals.

5.1. Introduction

In recent years, intense efforts have been directed towards the development of a molecular understanding of the role of nanoparticle properties such as size, structure, and composition on catalytic activity and selectivity[1, 2]. Nanoparticle shape, in particular, has been demonstrated to play an important role in catalysis[3-8]. The role of shape is thought to be closely related to the role of structure-sensitivity in catalysis. As an example, a study of benzene hydrogenation on ~12-13 nm Pt nanoparticles found that both cyclohexene and cyclohexane were formed on cuboctahedral nanoparticles, which contain primarily 111-faces, whereas only cyclohexane was formed on 100-dominated cubic nanoparticles[5]. These selectivities were consistent with previous results on (111) and (100) Pt single crystals[11, 12]. Nanoparticle shape was also shown to play an important role in selectivity in pyrrole hydrogenation on Pt nanopolyhedra and nanocubes[4]. This study found that although *n*-butylamine was the dominant product for both 5 and 9 nm Pt nanocubes at low temperature, both pyrrolidine and *n*-butylamine were formed on 5 nm Pt nanopolyhedra. These studies demonstrate the importance of the role of nanoparticle shape in catalysis and, in particular, the importance of characterizing this role in relation to single crystal studies on structure-sensitive reactions.

The reaction studied here, the catalytic reduction of Nitric Oxide (NO) by Carbon Monoxide (CO) on Rhodium metal, is extremely important because of its role in the three-way catalytic converter used in automobile exhaust systems[13]. The reaction proceeds much faster on Rh than on Pd or Pt[14] and is known to be structure sensitive on Rh single crystals[10]. The products of the reaction are CO_2 at all temperatures, N_2O primarily (~75%) at the lower (< 320°C) temperatures investigated in this study, and N_2 primarily at higher temperatures (> 320 °C)[14]. Although many mechanisms have been proposed for this reaction[9, 15-20], it remains an open area of investigation[21, 22] due to its enormous complexity. One relatively simple model, proposed by Permana et al.[23], is as follows, where S refers to an available surface site:

(1) $CO_{(g)} + S \leftrightarrow CO_{(ads)}$
(2) $NO_{(g)} + S \leftrightarrow NO_{(ads)}$
(3) $NO_{(ads)} + S \rightarrow N_{(ads)} + O_{(ads)}$
(4) $CO_{(ads)} + O_{(ads)} \rightarrow CO_{2\,(g)} + 2\ S$
(5) $NO_{(ads)} + N_{(ads)} \rightarrow N_2O_{(g)} + 2\ S$
(6) $2\ N_{(ads)} \rightarrow N_{2\,(g)} + 2\ S$

More detailed models, such as that proposed by Chuang and Tan[24], account for the role of Rh oxidation in the reaction, which is very important in strongly oxidizing conditions and for

smaller, more easily oxidized catalysts. Other models, such as that proposed by Avalos et al., account for experimental evidence of N-island formation[25] and concerns that Step (6), above, may be too slow to adequately account for N_2 production during reaction. In light of this, these authors suggest that the decomposition of an intermediate surface species, N-NO, is responsible for N_2 formation during the reaction. Much work has also been done to elucidate the role of nanoparticle size on this reaction[26-28]. Oh and Eickel, for example, found that increased Rh particle size leads to a significant increase in turnover frequency, a decrease in calculated activation energy, and no significant effect on selectivity[26]. The role of nanoparticle shape in the NO-CO reaction, however, has not yet been addressed. This paper reports results of a study on the role of nanoparticle shape in this reaction. Rh nanopolyhedra and nanocubes were synthesized, characterized, and studied in reaction conditions similar to those used in previous studies on Rh single crystals[9, 15, 23]. Our results show a clear shape-dependence for the NO-CO reaction at low temperatures (230-270°C) based on observed differences in turnover frequency and activation energy on the Rh nanopolyhedra and Rh nanocube catalysts.

5.2. Experimental Details

5.2.1. Nanoparticle Synthesis

Rh NPs of (111)-oriented nanopolyhedra[29] and (100)-oriented nanocubes[30] were synthesized using two similar techniques, both of which have been published previously. In brief, to make the nanopolyhedra, 0.00625 mmol $[Rh(Ac)_2]_2$ and 0.25 mmol poly(vinylpyrrolidone) (Mw = 55,000, in terms of the repeating unit) were added to 20 ml ethylene glycol in a 50 ml three-necked flask at room temperature. The solution was then heated to 100 °C and degassed for 20 min under vacuum while stirring, resulting in a green solution. The flask was then heated to 185 °C at 10 °C min-1, and maintained at this temperature for 2 h under Ar. When the reaction was complete, an excess of acetone was added at room temperature and the resulting Rh nanopolyhedra were separated by centrifugation and washed twice by precipitation/dispersion[29].

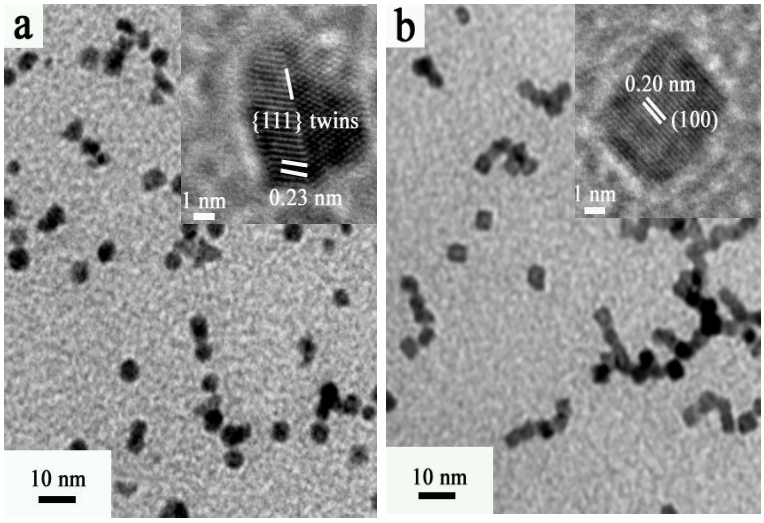

Figure 5.1 TEM images of (a) 6.5 nm Rh nanopolyhedra, and (b) 6.2 nm Rh nanocube catalysts.

The procedure used to synthesize Rh nanocubes was similar to that used to synthesize Rh nanopolyhedra, except that 0.2 mmol $RhCl_3$, 1 mmol tetramethylammonium bromide, and 4 mmol poly(vinylpyrrolidone) (Mw = 24,000, in terms of the repeating unit) were added to 20 ml ethylene glycol in a 50 ml three-necked flask at room temperature, which was evacuated at 80 °C for 20 min, and heated at 185 °C for 1.5 h[30]. Both the nanopolyhedra and nanocube samples were subsequently deposited onto 1 x 1 cm^2 pieces of Si wafer using the Langmuir-Blodgett technique, which has been described previously[29].

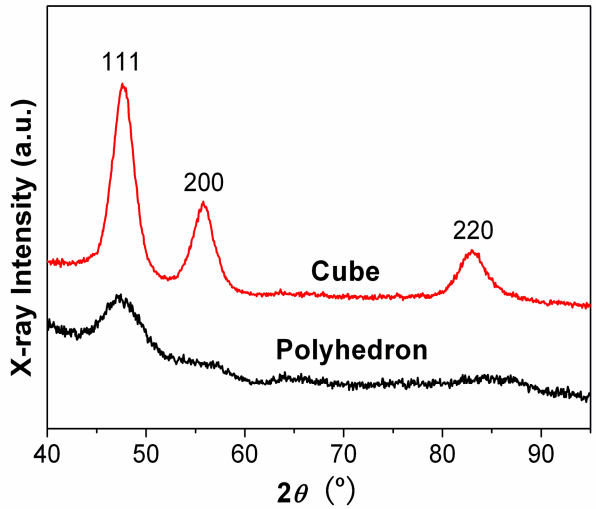

Figure 5.2 XRD of Rh nanopolyhedra and Rh nanocube catalysts.

5.2.2. Nanoparticle Characterization

The shape, size, and lattice structure of the Rh nanocrystals were analyzed using a Philips FEI Tecnai 12 Transmission electron microscope (TEM) and Philips CM200/FEG high-resolution TEM (HRTEM), operated at 100 and 200 kV, respectively. Analysis of at least 50 particles from each synthesis determined that the sizes of the two types of nanoparticle catalysts are comparable, with the nanopolyhedra measuring approximately 6.5 ± 0.6 nm in diameter and the nanocubes measuring approximately 6.2 ± 0.6 nm in diameter, as shown in Figure 5.1. Powder X-ray diffraction (XRD) patterns were recorded on a Bruker D8 GADDS diffractometer using Co-Kα radiation (λ = 1.79 Å). The recorded spectra are presented in Figure 5.2. Both TEM and XRD indicated that the nanopolyhedra have predominantly (111) surface sites, whereas the nanocubes have predominantly (100) surface sites. The presence of some (111) and (220)-oriented sites in the XRD is likely due to a combination of defects in the nanoparticles and, especially for the (111) peak, the sensitivity of XRD to bulk crystallinity in addition to surface orientation. Sample coverage, uniformity, and aggregation were checked before and after reaction using a Zeiss Ultra 55 Field Emission Scanning Electron Microscope. No significant surface melting or particle aggregation was observed within the limits of detection of SEM for nanoparticles subjected to a reaction temperature of 270°C. Nanoparticles subjected to higher reaction temperatures typically showed evidence of melting and aggregation. Prior to reaction,

particles were difficult to image, presumably due to the PVP capping layer, which may have been partially removed during reaction[31].

5.2.3. Reaction Setup

Reaction studies were performed in batch mode with 8 torr NO, 8 torr CO, and 744 torr He in a 1 L ultrahigh vacuum chamber with a base pressure of 1.0 × 10−8 Torr. These reactant pressures were chosen in order to be consistent with conditions used for high-pressure single crystal studies [9, 15, 23]. Sample temperature was measured with a Type-K thermocouple mounted on a 8 mm^2 piece of blank Si wafer on the same ceramic button heater (Momentive) used to heat the sample. Products were measured with an HP Series II gas chromatograph equipped with a thermal conductivity detector and separated with two columns in parallel – a 1 m x 1/8" 60/80 Argon sieve (Supelco) to separate N_2, NO, and CO, and a 3 m x 1/8" 100/120 Hayesep D (Supelco) to separate N_2O and CO_2. The reaction was carried out multiple times over fresh samples of each catalyst. The reaction temperature was kept between 230 and 270°C to ensure that product formation was fast enough for accurate measurement and that the nanoparticles did not aggregate or sinter significantly. Data gathered above the 270°C threshold was not reliable and is not reported here. Turnover frequency at each temperature was determined over the course of 3 hours. No significant deactivation was detected. The measured reaction rates are reported as turnover frequencies (TOF) and are measured in units of product molecules per metal surface site per second. The number of surface sites was determined from SEM images taken from randomly-selected areas of the sample, analyzed with conventional image processing software to determine nanoparticle coverage, and converted into surface sites based purely on geometrical considerations. This method is intended to calculate the total number of surface sites and cannot account for site blocking by the PVP capping agent or other means. Consequently, the results presented here are overestimates of the number of active reaction sites and thus underestimate the true turnover frequency. It is also possible that some PVP capping agent is removed during reaction[31], which could result in an increased number of active reaction sites at high temperature. Previous studies have established the difficulty of determining truly exact turnover numbers and the importance of qualitative analysis of turnover frequencies even on comparatively stable samples in the same reaction system[32-34].

5.3. Results and Discussion

The turnover frequencies (TOF) for CO_2, N_2O, and N_2 formation for the Rh nanopolyhedra and Rh nanocube catalysts are reported in Figure 5.3. The activation energies as calculated from the accumulation of each product from 230 - 270°C are presented in Table 1 for both the nanopolyhedra and nanocube catalysts, as compared to single crystal data taken at similar temperatures and pressures[9, 10]. The measured turnover frequencies were higher for the nanocube catalysts than for the nanopolyhedra catalysts at all temperatures. The measured activation energies of the products from the reaction on the Rh nanopolyhedra catalysts were 37.0 ± 3.3, 39.3 ± 4.3, and 26.6 ± 3.7 kcal/mol for CO_2, N_2O, and N_2 formation, respectively. The activation energies of the products from the reaction on the Rh nanocube catalysts were 28.4 ± 1.6, 30.6 ± 4.5, and 22.0 ± 3.1 kcal/mol, for CO_2, N_2O, and N_2 formation. The selectivity for

N_2O versus N_2 was similar for both catalysts and increased with temperature, from ~70% N_2O at 230°C to ~84% N_2O at 270°C. Both catalysts produced primarily N_2O in this temperature range.

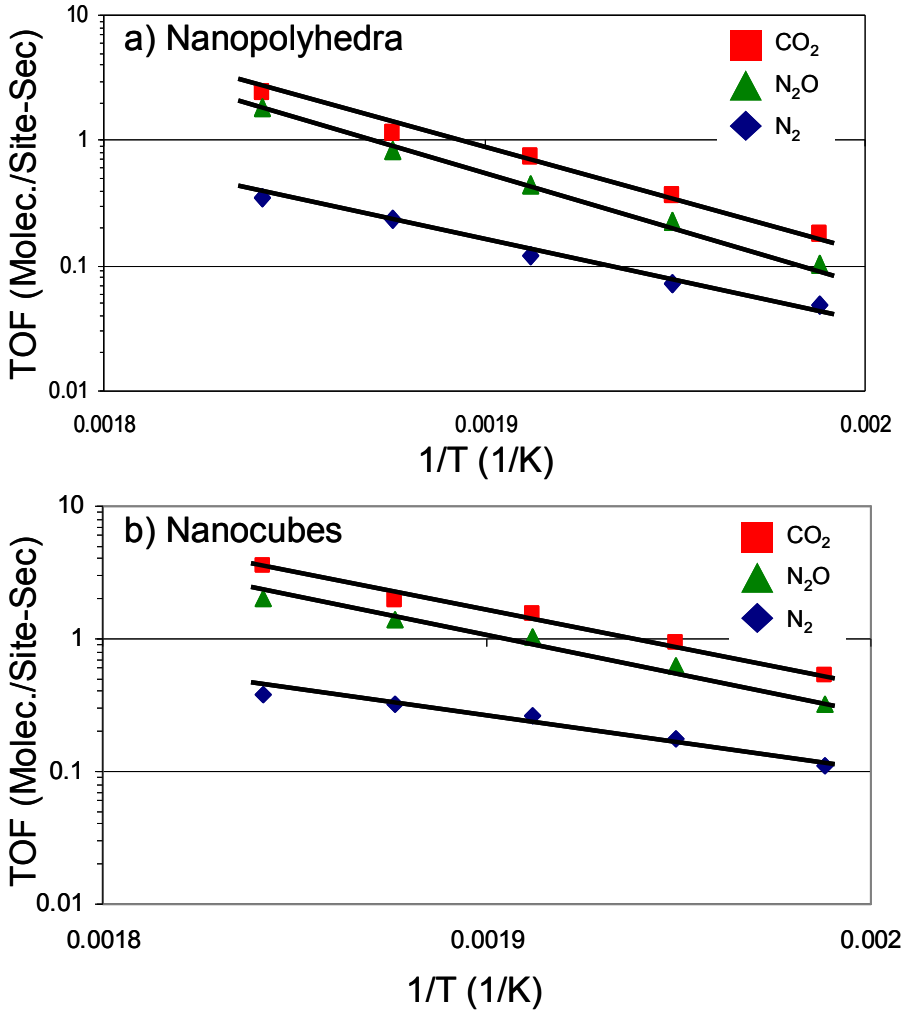

Figure 5.3 CO_2, N_2O, and N_2 turnover frequencies of a) Rh nanopolyhedra and b) Rh nanocube catalysts as a function of inverse temperature.

The Rh nanopolyhedra and Rh nanocubes compare well to trends in Rh single crystals studied at similar pressures. Previous reports in this temperature range have found higher turnover frequencies for Rh (100) single crystals than for Rh (111) single crystals[9, 10]. Both Rh (100) and Rh (111) single crystals are strongly selective towards N_2O in this temperature range[9, 10]. The similarities in the trends between these single crystal results and the shape-dependent results presented here for (111)-dominated nanopolyhedra and (100)-dominated nanocubes indicate that the effect of surface structure on turnover frequency and selectivity is similar in both nanoparticle and single crystal regimes. Evidence from measured activation energies, however, implies more complexity, as shown in Table 1. Although the activation energies for CO_2 and N_2O formation on the nanopolyhedra catalysts are similar to those previously reported for this reaction on Rh (111) single crystals[9], the measured activation energies for CO_2 and N_2O formation on the nanocube catalysts are intermediate to the two separate temperature regimes reported previously on Rh (100) single crystals[10]. Rh (100) single crystals have been reported to

feature both a low temperature regime with higher activation energies for all products and a high temperature regime with lower activation energies for all products starting at about 315°C[10, 16]. Herman et al. attributed this breakpoint to a higher coverage of adsorbed N and adsorbed NO species on the (100) surface at lower temperatures and a consequent shortage of available sites for NO dissociation, a shortage that is alleviated at high temperatures to the extent that the rate of NO dissociation begins to limit the reaction rather than the availability of sites[10] The activation energy measured for N_2 formation on both the nanopolyhedra and nanocube catalysts was lower than that reported on single crystals[10], as reported in Table 5.1. This may be due to the increased selectivity towards N_2O observed in the nanoparticle catalysts. In addition to the effect of NO adsorption and dissociation site availability, another possible explanation for the intermediate activation energies found for the nanocubes is that the small size of the nanoparticles leads to different kinetics than for (100) single crystals. In this case, the observed differences could be attributed to the role of Rh oxide in catalytic reactivity[24, 35, 36], because relatively small transition metal nanoparticles develop stable oxides at lower temperatures than single crystals[37], which may amplify the effect of differences in the oxidation of Rh (111) and Rh (100)[38] on the catalytic reactivity of the 6.2 nm nanocubes and 6.5 nm nanopolyhedra.

	CO_2 E_a	N_2O E_a	N_2 E_a	Selectivity
Nanopolyhedra[a]	37.0 ± 3.3	39.3 ± 4.3	26.6 ± 3.7	84%
Nanocubes[a,]	28.4 ± 1.6	30.6 ± 4.5	22.0 ± 3.1	84%
Rh (111)[9]	34.2	35.7	32.1	~72%[b]
Rh (100) LT[10]	35.0	35.8	33.8	~64%[b]
Rh (100) HT[10]	22.2	15.3	26.2	

[a] E_a (kcal/mol) measured from 230 - 270°C
b Estimated from published results

Table 5.1 Apparent activation energies (E_a, kcal/mol) for CO_2, N_2O, and N_2 and selectivity toward N_2O (where Selectivity = $N_2O/(N_2O + N_2)$ * 100%) at 270°C for the NO-CO reaction at 8 torr NO and 8 torr CO over Rh nanopolyhedra, Rh nanocube, Rh (111) single crystal, and Rh (100) single crystal catalysts. Single crystal values are as reported previously[9, 10]. LT refers to a temperature range of ~255 - 320°C and HT refers to a range of ~320 - 400°C.

Surface reconstruction and rearrangement is also a possible cause of the intermediate activation energies measured on the cubic nanoparticles, as single crystals are well-known to reconstruct at elevated temperatures and pressures[39] and nanoparticle surface melting is a growing part of present day inquiry[40]. Surface reconstruction is also known to be effected by surface oxidation in some cases[36], a phenomenon which may be important in the system investigated in this work. Although not presented in detail here, some experimental evidence during reaction above 270°C and subsequent re-reaction at lower temperatures on the same Rh nanocube sample suggested surface reconstruction and a shift towards (111)-like kinetics in the nanocubes which did not occur for the nanopolyhedra, which were already in the low surface energy (111) surface atom arrangement. In this case it is possible that the intermediate activation energies reported for the cubic nanocatalysts may have been a result of temperature-dependent

surface reconstruction and the measurement of a temperature regime either intermediate to or inclusive of two separate crystal-face regimes – a (100)-dominated low temperature regime and a (111)-dominated post-melting high temperature regime. Further work is required to fully understand the role of surface reconstruction in structure sensitive catalytic reactions on shape-controlled nanoparticles.

The differences in the overall catalytic activity between the nanopolyhedra and nanocubes are likely due to several mechanistic differences in the reaction between NO and CO on Rh (100) and Rh (111) [9, 10, 15, 16, 19, 21-23, 25, 41-46]. In summary, the reaction between CO and O is faster and the products of NO dissociation have a higher heat of adsorption on the (100) surface than on the (111) surface[41]. These differences mean that CO_2 formation and NO dissociation are faster on (100) surfaces at low temperatures, which leads to higher turnover frequencies for all products on (100) surfaces at relatively low temperatures. As temperature increases, however, the accumulation of strongly bound N leads to a lower rate of N_2 formation and desorption, which eventually leads to site blocking and a greater degree of lateral interactions with coadsorbed species[46]. When the temperature is high enough (~320°C on the (100) single crystal), N_2 is formed more easily and there is an abrupt change in selectivity towards N_2 which also affects the formation of the other products[10].

5.4. Conclusions

The study of the role of shape is important to the understanding and development of new nanocatalysts for future applications. In this study, we showed a relationship between nanoparticle shape and catalytic properties for the reduction of NO by CO. We synthesized PVP-capped 6.5 nm nanopolyhedra and 6.2 nm rhodium nanocubes and deposited them evenly across silicon wafers using the Langmuir-Blodgett technique. We then characterized the nanoparticles with TEM, XRD, and SEM, and studied their behavior in the NO + CO reaction. Our study found that nanocubes show higher turnover frequency and lower activation energies for all products and similar selectivity toward N_2O between 230 and 270°C as compared to nanopolyhedra due to the differences in surface structure. The activation energies for product formation on the Rh nanopolyhedra were found to be comparable to previous reports on Rh (111) single crystals, whereas the activation energies measured on the Rh nanocubes were found to be intermediate to those previously reported for two temperature regimes studied on Rh (100) single crystals. This study clearly shows that nanoparticle shape has an important effect on the reduction of NO by CO at low temperatures and implies that nanoparticle shape is an important criterion in the development of nanocatalysts for a wide range of structure-sensitive heterogeneous catalytic reactions.

5.5. References

1. Bell, A. T., The impact of nanoscience on heterogeneous catalysis. *Science* **2003,** *299* (5613), 1688-1691.
2. Peng, Z. M.; Yang, H., Designer platinum nanoparticles: Control of shape, composition in alloy, nanostructure and electrocatalytic property. *Nano Today* **2009,** *4* (2), 143-164.
3. Lee, I.; Delbecq, F.; Morales, R.; Albiter, M. A.; Zaera, F., Tuning selectivity in catalysis by controlling particle shape. *Nature Materials* **2009,** *8* (2), 132-138.

4. Tsung, C. K.; Kuhn, J. N.; Huang, W. Y.; Aliaga, C.; Hung, L. I.; Somorjai, G. A.; Yang, P. D., Sub-10 nm Platinum Nanocrystals with Size and Shape Control: Catalytic Study for Ethylene and Pyrrole Hydrogenation. *Journal of the American Chemical Society* **2009,** *131* (16), 5816-5822.
5. Bratlie, K. M.; Lee, H.; Komvopoulos, K.; Yang, P. D.; Somorjai, G. A., Platinum nanoparticle shape effects on benzene hydrogenation selectivity. *Nano Lett.* **2007,** *7* (10), 3097-3101.
6. Grass, M. E.; Yue, Y.; Habas, S. E.; Rioux, R. M.; Teall, C. I.; Yang, P.; Somorjai, G. A., Silver ion mediated shape control of platinum nanoparticles: Removal of silver by selective etching leads to increased catalytic activity. *Journal of Physical Chemistry C* **2008,** *112* (13), 4797-4804.
7. El-Sayed, M. A., Shape-dependent nanocatalysis and the effect of catalysis on the nanoparticle shape and size in colloidal solution. *Abstracts of Papers of the American Chemical Society* **2006,** *231*, 212-IEC.
8. Subhramannia, M.; Pillai, V. K., Shape-dependent electrocatalytic activity of platinum nanostructures. *Journal of Materials Chemistry* **2008,** *18* (48), 5858-5870.
9. Peden, C. H. F.; Belton, D. N.; Schmieg, S. J., STRUCTURE SENSITIVE SELECTIVITY OF THE NO-CO REACTION OVER RH(110) AND RH(111). *Journal of Catalysis* **1995,** *155* (2), 204-218.
10. Herman, G. S.; Peden, C. H. F.; Schmieg, S. J.; Belton, D. N., A comparison of the NO-CO reaction over Rh(100), Rh(110) and Rh(111). *Catalysis Letters* **1999,** *62* (2-4), 131-138.
11. Bratlie, K. M.; Flores, L. D.; Somorjai, G. A., In situ sum frequency generation vibrational spectroscopy observation of a reactive surface intermediate during high-pressure benzene hydrogenation. *J. Phys. Chem. B* **2006,** *110* (20), 10051-10057.
12. Bratlie, K. M.; Kliewer, C. J.; Somorjai, G. A., Structure effects of benzene hydrogenation studied with sum frequency generation vibrational spectroscopy and kinetics on Pt(111) and Pt(100) single-crystal surfaces. *J. Phys. Chem. B* **2006,** *110* (36), 17925-17930.
13. Taylor, K. C., Nitric Oxide Catalysis in Automotive Exhaust Systems. *Catalysis Reviews: Science and Engineering* **1993,** *35* (4), 457 - 481.
14. Granger, P.; Dhainaut, F.; Pietrzik, S.; Malfoy, P.; Mamede, A. S.; Leclercq, L.; Leclercq, G., An overview: Comparative kinetic behaviour of Pt, Rh and Pd in the NO+CO and NO+H-2 reactions. *Topics in Catalysis* **2006,** *39* (1-2), 65-76.
15. Permana, H.; Ng, K. Y. S.; Peden, C. H. F.; Schmieg, S. J.; Lambert, D. K.; Belton, D. N., Adsorbed species and reaction rates for NO-CO over Rh(111). *Journal of Catalysis* **1996,** *164* (1), 194-206.
16. Hendershot, R. E.; Hansen, R. S., REDUCTION OF NITRIC-OXIDE WITH CARBON-MONOXIDE ON THE RH(100) SINGLE-CRYSTAL SURFACE. *Journal of Catalysis* **1986,** *98* (1), 150-165.
17. Peden, C. H. F.; Goodman, D. W.; Blair, D. S.; Berlowitz, P. J.; Fisher, G. B.; Oh, S. H., KINETICS OF CO OXIDATION BY O2 OR NO ON RH(111) AND RH(100) SINGLE-CRYSTALS. *Journal of Physical Chemistry* **1988,** *92* (6), 1563-1567.
18. Belton, D. N.; DiMaggio, C. L.; Schmieg, S. J.; Ng, K. Y. S., Reaction of coadsorbed nitric oxide and nitrogen atoms on Rh(111). *Journal of Catalysis* **1995,** *157* (2), 559-568.
19. Avalos, L. A.; Bustos, V.; Unac, R.; Zaera, F.; Zgrablich, G., Toward a realistic model for the kinetics of the NO plus CO reaction on rhodium surfaces. *Journal of Molecular Catalysis a-Chemical* **2005,** *228* (1-2), 89-95.

20. Hecker, W. C.; Bell, A. T., REDUCTION OF NO BY CO OVER SILICA-SUPPORTED RHODIUM - INFRARED AND KINETIC-STUDIES. *Journal of Catalysis* **1983,** *84* (1), 200-215.
21. Matsushima, T., N-2 emission in NO and N2O reduction on Rh(100) and Rh(110). *Phys. Chem. Chem. Phys.* **2007,** *9* (23), 3031-3042.
22. Gustafson, J., Westerstrom, R., Resta, A., Mikkelsen, A., Andersen, J.N., Balmes, O., Torrelles, X., Schmid, M., Varga, P., Hammer, B., Kresse, G., Baddeley, C.J., Lundgren, E., Structure and catalytic reactivity of Rh oxides. *Catalysis Today* **2009**.
23. Permana, H.; Ng, K. Y. S.; Peden, C. H. F.; Schmieg, S. J.; Belton, D. N., EFFECT OF NO PRESSURE ON THE REACTION OF NO AND CO OVER RH(111). *Journal of Physical Chemistry* **1995,** *99* (44), 16344-16350.
24. Chuang, S. S. C.; Tan, C. D., Mechanistic studies of the NO-CO reaction on Rh/Al2O3 under net-oxidizing conditions. *Journal of Catalysis* **1998,** *173* (1), 95-104.
25. Zaera, F.; Gopinath, C. S., Effect of coverage and temperature on the kinetics of nitrogen desorption from Rh(111) surfaces. *Journal of Chemical Physics* **2002,** *116* (3), 1128-1136.
26. Oh, S. H.; Eickel, C. C., INFLUENCE OF METAL-PARTICLE SIZE AND SUPPORT ON THE CATALYTIC PROPERTIES OF SUPPORTED RHODIUM - CO-O2 AND CO-NO REACTIONS. *Journal of Catalysis* **1991,** *128* (2), 526-536.
27. Araya, P.; Gracia, F.; Cortes, J.; Wolf, E. E., FTIR study of the reduction reaction of NO by CO over Rh/SiO2 catalysts with different crystallite size. *Applied Catalysis B-Environmental* **2002,** *38* (2), 77-90.
28. Kaspar, J.; Deleitenburg, C.; Fornasiero, P.; Trovarelli, A.; Graziani, M., NO REDUCTION BY CO OVER RH AL2O3 - EFFECTS OF RHODIUM DISPERSION ON THE CATALYTIC PROPERTIES. *Journal of Catalysis* **1994,** *146* (1), 136-143.
29. Zhang, Y. W.; Grass, M. E.; Habas, S. E.; Tao, F.; Zhang, T. F.; Yang, P. D.; Somorjai, G. A., One-step polyol synthesis and langmuir-blodgett monolayer formation of size-tunable monodisperse rhodium nanocrystals with catalytically active (111) surface structures. *Journal of Physical Chemistry C* **2007,** *111* (33), 12243-12253.
30. Zhang, Y. W.; Grass, M. E.; Kuhn, J. N.; Tao, F.; Habas, S. E.; Huang, W. Y.; Yang, P. D.; Somorjai, G. A., Highly selective synthesis of cataytically active monodisperse rhodium nanocubes. *Journal of the American Chemical Society* **2008,** *130* (18), 5868-+.
31. Grass, M. E.; Zhang, Y. W.; Butcher, D. R.; Park, J. Y.; Li, Y. M.; Bluhm, H.; Bratlie, K. M.; Zhang, T. F.; Somorjai, G. A., A Reactive Oxide Overlayer on Rhodium Nanoparticles during CO Oxidation and Its Size Dependence Studied by In Situ Ambient-Pressure X-ray Photoelectron Spectroscopy. *Angewandte Chemie-International Edition* **2008,** *47* (46), 8893-8896.
32. Choi, K. I.; Vannice, M. A., CO OXIDATION OVER PD AND CU CATALYSTS .3. REDUCED AL2O3-SUPPORTED PD. *Journal of Catalysis* **1991,** *131* (1), 1-21.
33. Yao, Y. F. Y., THE OXIDATION OF CO AND HYDROCARBONS OVER NOBLE-METAL CATALYSTS. *Journal of Catalysis* **1984,** *87* (1), 152-162.
34. Yoon, K. J.; Kang, H. K.; Yie, J. E., Synergism and kinetics in CO oxidation over palladium-rhodium bimetallic catalysts. *Korean Journal of Chemical Engineering* **1997,** *14* (5), 399-406.
35. Gustafson, J.; Westerström, R.; Resta, A.; Mikkelsen, A.; Andersen, J. N.; Balmes, O.; Torrelles, X.; Schmid, M.; Varga, P.; Hammer, B.; Kresse, G.; Baddeley, C. J.; Lundgren, E., Structure and catalytic reactivity of Rh oxides. *Catalysis Today In Press, Corrected Proof*.

36. Medvedev, V. K.; Suchorski, Y.; Voss, C.; de Bocarme, T. V.; Bar, T.; Kruse, N., Oxygen-induced reconstruction and surface oxidation of rhodium. *Langmuir* **1998,** *14* (21), 6151-6157.
37. Campbell, C. T., Transition metal oxides: extra thermodynamic stability as thin films. *Physical Review Letters* **2006,** *96* (6), 066106/1-4.
38. Seriani, N.; Mittendorfer, F., Platinum-group and noble metals under oxidizing conditions. *J. Phys.-Condes. Matter* **2008,** *20* (18), 11.
39. Somorjai, G. A., SURFACE RECONSTRUCTION AND CATALYSIS. *Annu. Rev. Phys. Chem.* **1994,** *45*, 721-751.
40. Tian, H. C.; Liu, L.; Wen, Y. H., Shape changes and melting characteristics of cubic Pt nanoparticle:A molecular dynamics study. *Acta Phys. Sin.* **2009,** *58* (6), 4080-4084.
41. Hopstaken, M. J. P. Elementary Reaction Kinetics and Lateral Interactions in the Catalytic Reaction between NO and CO on Rhodium Surfaces. Eindhoven University of Technology, Eindhoven, The Netherlands, 2000.
42. Kim, Y. J.; Thevuthasan, S.; Herman, G. S.; Peden, C. H. F.; Chambers, S. A.; Belton, D. N.; Permana, H., Chemisorption geometry of NO on Rh(111) by X-ray photoelectron diffraction. *Surf. Sci.* **1996,** *359* (1-3), 269-279.
43. Loffreda, D.; Simon, D.; Sautet, P., Molecular and dissociative chemisorption of NO on palladium and rhodium (100) and (111) surfaces: A density-functional periodic study. *Journal of Chemical Physics* **1998,** *108* (15), 6447-6457.
44. Oh, S. H.; Fisher, G. B.; Carpenter, J. E.; Goodman, D. W., COMPARATIVE KINETIC-STUDIES OF CO-O2 AND CO-NO REACTIONS OVER SINGLE-CRYSTAL AND SUPPORTED RHODIUM CATALYSTS. *Journal of Catalysis* **1986,** *100* (2), 360-376.
45. Zaera, F.; Gopinath, C. S., Evidence for an N2O intermediate in the catalytic reduction of NO to N-2 on rhodium surfaces. *Chem. Phys. Lett.* **2000,** *332* (3-4), 209-214.
46. Hopstaken, M. J. P.; Niemantsverdriet, J. W. In *Reaction between NO and CO on rhodium (100): How lateral interactions lead to auto-accelerating kinetics*, The 46th international symposium of the american vacuum society, Seattle, Washington (USA), AVS: Seattle, Washington (USA), 2000; pp 1503-1508.

Chapter 6. $Rh_{1-x}Pd_x$ Nanoparticle Composition Dependence in CO Oxidation by Oxygen

Bimetallic 15 nm Pd-core Rh-shell $Rh_{1-x}Pd_x$ nanoparticle catalysts of five different compositions and supported on p-type Si wafers have been synthesized, characterized using TEM, SEM, and XPS, and studied in CO oxidation by O_2. The catalysts exhibited composition-dependent activity enhancement (synergy) in CO oxidation in O_2. The observed synergy is due to spillover of O atoms from Rh onto CO-covered Pd reaction sites in reaction conditions.

6.1. Introduction

Bimetallic catalysts are frequently utilized for industrial applications and they are important model systems for furthering the understanding of catalytic mechanisms and processes. These catalysts often exhibit increased activity, favorable selectivity, and reduced rates of deactivation [1-9]. For example, one recent study by Stamenkovic et al. on a $Pt_3Ni(111)$ single crystal in the oxygen reduction reaction demonstrated a 10-fold enhancement in catalytic activity over the corresponding Pt(111) surface[1]. This effect was determined to be a result of compositional oscillation in the top three layers of the catalysts. Another study by Gao et al. found that CO oxidation kinetics on AuPd(100) depend on whether Pd sites are isolated or contiguous, because of significant differences in CO binding on the two types of sites[2].

The studies by Stamenkovic and Gao both used bimetallic single crystals. Single crystals, however, are known to behave quite differently from nanoparticles[10]. Nanoparticle reactivity is often dependent on size and oxidation state[11], in part because small particles can oxidize much more easily than large particles and, especially, single crystals. In order to expand control and understanding of bimetallic nanoparticle catalysts there is a need for detailed studies on the roles of nanoparticle size, surface composition, and *in-situ* oxidation state on catalytic behavior.

Among the large number of possible nanoparticle compositions, Rh, Pt, and Pd-based mono-, bi-, and trimetallic nanocrystals with controlled composition, size, and shape are of special interest because of their role in three-way automotive exhaust catalysis[12]. Although CO oxidation has been studied extensively, many open questions remain regarding catalyst behavior in these systems, especially with regard to composition and oxidation state[13, 14] and how these factors affect catalyst deactivation[15], synergism[16], and surface segregation[17].

Previous work in our lab on 15 nm $Rh_{0.5}Pd_{0.5}$ bimetallic Pd-core Rh-shell nanoparticles supported on Si wafers used ambient pressure x-ray photoelectron spectroscopy (APXPS) to examine the dependence of surface composition and oxidation state on the local chemical environment[17]. This study found significant reversible changes in the catalyst composition when the nanoparticles were exposed to NO, CO, O_2, H_2, and mixtures of NO+CO, and CO+O_2. The catalytic reaction kinetics of these nanoparticles has not previously been studied in the CO + O_2 reaction, however.

In this chapter, the synthesis of near-monodisperse $Rh_{1-x}Pd_x$ (x = 0-1) nanocrystals at a constant size of 15 nm by a one-step polyol method is reported. The as-synthesized bimetallic nanocrystals have Rh-rich surfaces. The catalytic activity of the nanocrystals is investigated in the oxidation of CO by O_2 and models are proposed to explain the complex behavior in each reaction.

6.2. Experimental Details

6.2.1. Synthesis of $Rh_{1-x}Pd_x$ (x = 0.0 - 1.0) Nanoparticles

Rhodium(III) acetylacetonate ($Rh(acac)_3$, 97%), palladium(II) acetlacetonate ($Pd(acac)_2$, 99%), 1,4-butanediol (99%), and poly(vinylpyrrolidone) (PVP, *M*w = 55,000) were purchased from Sigma-Aldrich. All the solvents, including acetone, ethanol, hexane, and chloroform, were of analytical grade and were used without further purification.

Given amounts of $Rh(acac)_3$ and $Pd(acac)_2$ (0.1 mmol total) and 1 mmol PVP (monomer concentration) were added to 20 ml of 1,4 butanediol in a 50 ml three-necked flask at room temperature (Table 1). The stock solution was heated to 50°C using a Glas-Col electromantle (60 W, 50 ml) with a Cole-Parmer temperature controller (Diqi-sense®), and was evacuated at this temperature for 20 min to remove water and oxygen under magnetic stirring, resulting in an optically transparent orange-yellow solution. The flask was then heated to 220°C at a rate of 10°C min^{-1} and maintained at this temperature (± 2°C) for 1.5 h under Ar. During the reaction the color of the solution gradually turned from orange-yellow to black. When the reaction was complete an excess of acetone was poured into the solution at room temperature to form a cloudy black suspension. This suspension was separated by centrifugation at 4200 rpm for 6 min and the black product was collected by discarding the colorless supernatant. The precipitated $Rh_{1-x}Pd_x$ nanocrystals were washed with acetone once then re-dispersed in ethanol.

Sample	$Rh(acac)_3$ [mmol]	$Pd(acac)_2$ [mmol]	T [°C]	t [h]	a (nm)	Size [nm]
Rh	0.2	0	205	2	0.385	14.4 ± 1.4 [a]
$Rh_{0.8}Pd_{0.2}$	0.08	0.02	220	1.5	0.385	15.1 ± 2.9
$Rh_{0.6}Pd_{0.4}$	0.06	0.04	220	1.5	0.387	15.4 ± 2.4
$Rh_{0.5}Pd_{0.5}$	0.05	0.05	220	1.5	0.387	16.0 ± 1.9
$Rh_{0.4}Pd_{0.6}$	0.04	0.06	220	1.5	0.390	15.1 ± 2.0
$Rh_{0.2}Pd_{0.8}$	0.02	0.08	220	1.5	0.397	14.9 ± 2.0
Pd	0	0.1	220	0.5	0.395	15.6±2.4

[a] The standard deviation statistic from 100 nanocrystals.

Table 6.1 Synthetic Conditions, Lattice Constants, and Crystallite Sizes of PVP-capped $Rh_{1-x}Pd_x$ (x = 0-1) Nanocrystals.

The synthetic procedure used to produce Pd nanocrystals was the same as that used to synthesize $Rh_{1-x}Pd_x$ (x = 0.2-0.8) nanocrystals, except that 0.1 mmol $Pd(acac)_2$ was added to 20 ml of 1,4-butanediol in a 50 ml three-necked flask at room temperature for reaction at 220°C for 0.5 h (Table 1).

The synthetic procedure used for Rh nanocrystals was the same as that used to synthesize Pd nanocrystals, except that 0.2 mmol $Rh(acac)_3$ was added to 20 ml of 1,4-butanediol in a 50 ml three-necked flask at room temperature and evacuated at 140°C for 20 min, followed by reaction at 205°C for 2 h (Table 1).

6.2.2.Nanoparticle Deposition

The $Rh_{1-x}Pd_x$ nanocrystals were washed several times by repeated cycles of precipitation and dispersion. Precipitation was performed by adding 1 ml of the nanocrystal solution to 4 ml of hexane. The supernatant was decanted and the remaining precipitated nanoparticles were dispersed by sonication in 1 ml of ethanol (in early wash cycles) or chloroform (in later wash cycles) to remove the impurities and excess PVP. Monolayers of $Rh_{1-x}Pd_x$ nanocrystals were formed by placing drops of $Rh_{1-x}Pd_x$ nanocrystal chloroform solution onto the water subphase of a LB trough (Nima Technology, M611) at room temperature[18]. The surface pressure was monitored with a Wilhelmy plate, which was adjusted to zero prior to spreading the nanocrystals. A typical surface pressure was 11 mN/m, which resulted in nanoparticle surface coverage of 15-30%. The resulting surface layer was compressed by moving the mobile barrier at a rate of 15 cm^2/min. At different stages of compression, the $Rh_{1-x}Pd_x$ layers at the water-air interface were carefully transferred onto continuous carbon-coated copper grids using the Langmuir-Schäffer horizontal liftoff method. The $Rh_{1-x}Pd_x$ nanocrystals were deposited onto Si wafers (1 cm × 1 cm) by lift-up of the substrates at a rate of 1 mm/min. This 2D sample geometry was used in order to maximize similarity to those used in our previous APXPS studies[17].

6.2.3.Nanoparticle Characterization

The size, shape, and lattice structure of the $Rh_{1-x}Pd_x$ nanocrystals were analyzed using a Philips FEI Tecnai 12 transmission electron microscope (TEM) and Philips CM200/FEG high-resolution TEM (HRTEM), operated at 100 kV and 200 kV, respectively. The samples were prepared by placing a drop of the nanocrystal solution in ethanol onto a continuous carbon-coated copper TEM grid. Powder X-ray diffraction (XRD) patterns were recorded on a Bruker D8 GADDS diffractometer using Co-K_α radiation (λ = 1.79 Å). Lattice parameters of the nanocrystals were calculated with the least-squares method. X-ray Photoelectron Spectroscopy (XPS) experiments were performed on a Perkin-Elmer PHI 5300 XPS spectrometer with a position-sensitive detector and a hemispherical energy analyzer in an ion-pumped chamber (evacuated to 2×10^{-9} Torr). The Al-K_α (1486.6 eV) X-ray source of the XPS spectrometer was operated at 350 W with a 15 kV acceleration voltage. XPS was also carried out in UHV at the Advanced Light Source Beamline 9.3.2 for energy-dependent (and therefore depth-dependent) composition analysis. This system has been described previously[17]. The binding energy (BE) for the samples was calibrated by setting the measured BE of the broad C 1s, which is dominated by carbon from the PVP capping agent, to 285 eV. The elemental ratio was calculated from the integrated peak areas of the Rh 3d, Pd 3d, and O 1s core levels. The morphological changes of the $Rh_{1-x}Pd_x$ nanocrystals, Rh thin films, and Pd thin films before and after reaction were observed with a Zeiss Gemini Ultra-55 analytical scanning electron microscope (SEM). The total number of surface sites was calculated from coverage determined by a minimum of ten SEM images taken from randomly selected locations on each sample and taking into account the lattice parameters determined from XRD. This calculation is purely geometric and does not account for site blocking by strongly-bound capping agent molecules or other species.

6.2.4.Reaction Setup

CO oxidation reactions were performed in a laboratory scale batch reactor with continuous gas recirculation between 160 and 200 °C. Samples were loaded into quartz reactors with a type-K thermocouple touching the reactor near the sample. Prior to the reaction, the manifold was filled with 40 Torr CO (Praxair, UHP), 100 Torr O_2 (Praxair, UHP), and a balance of He (Praxair, UHP) initially at atmospheric pressure, all regulated by mass flow controllers. Gas composition was analyzed with a HP 5890 Series II gas chromatograph (GC) equipped with a thermal conductivity (TCD) detector. Turnover frequency (TOF, reported as product molecules/site/sec) was calculated by extrapolating the conversion data to the initial time and by correcting the $Rh_{1-x}Pd_x$ surface area using the method described in Section 6, above.

6.3. Characterization

Panels a-g of Figure 6.1 display TEM images of the $Rh_{1-x}Pd_x$ (x = 0-1) nanocrystals. The bimetallic nanocrystals are faceted, but show a mix of various shapes in 2D projection, such as hexagons, pentagons, triangles, and cubes. All the bimetallic nanocrystals have an average crystallite size near 15 nm, with standard size distributions of around 15% (Table 6.1). Panels h-k of Figure 6.1 depict the typical HRTEM images of $Rh_{0.5}Pd_{0.5}$ nanocrystals. The $Rh_{0.5}Pd_{0.5}$ nanocrystals are composed of (111) twinned pentagons (Figure 6.1h), (111) twinned hexagons (Figure 6.1i), (100)-oriented single-crystalline cubes and crystalline irregular particles. XRD measurements determined that all the bimetallic nanocrystals have a face-centered cubic *(fcc)* structure with lattice parameters lying between 0.385 and 0.397 nm (Table 6.1).

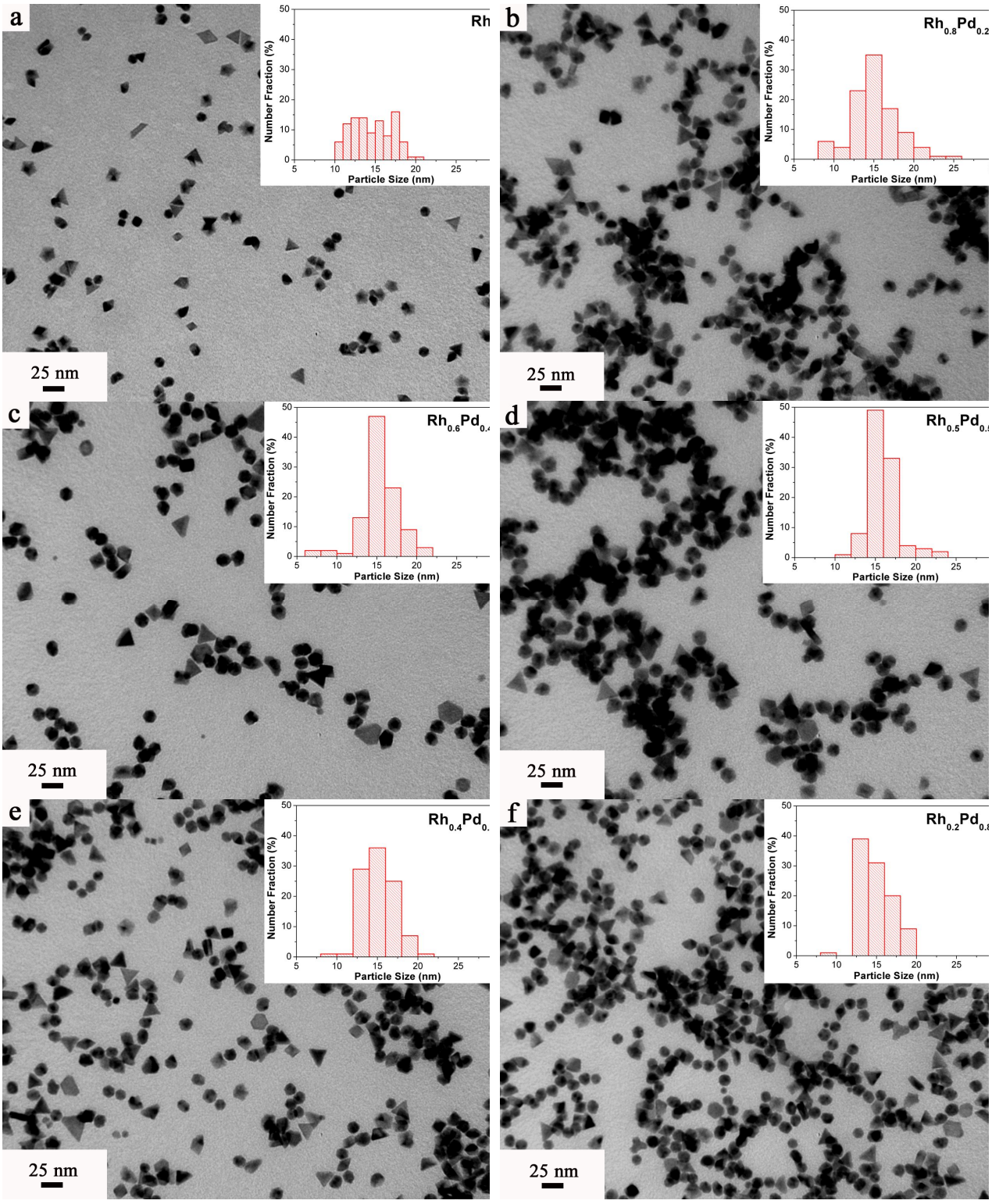
a
Rh
Number Fraction (%)
Particle Size (nm)
25 nm
b
Rh0.8Pd0.2
Number Fraction (%)
Particle Size (nm)
25 nm
c
Rh0.6Pd0.4
Number Fraction (%)
Particle Size (nm)
25 nm
d
Rh0.5Pd0.5
Number Fraction (%)
Particle Size (nm)
25 nm
e
Rh0.4Pd0.6
Number Fraction (%)
Particle Size (nm)
25 nm
f
Rh0.2Pd0.8
Number Fraction (%)
Particle Size (nm)
25 nm

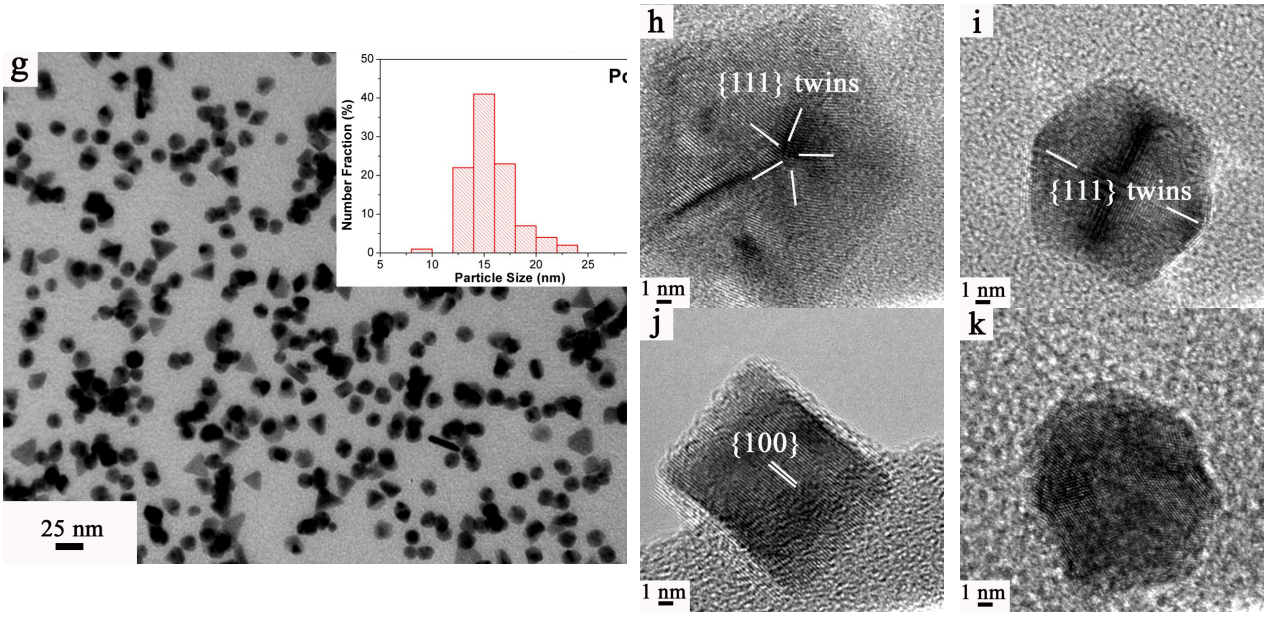

Figure 6.1 TEM images and size distribution histograms (insets) of $Rh_{1-x}Pd_x$ nanocrystals: (a) x = 0; (b) x = 0.2; (c) x = 0.4; (d) x = 0.5; (e) x = 0.6; (f) x = 0.8; (g) x = 1. (h-k) HRTEM images of $Rh_{0.5}Pd_{0.5}$ nanocrystals.

The surface compositions and core-shell structure of the bimetallic nanocrystals were measured experimentally by XPS. Two systems were used - one system with an Al K-α source with X-Ray Photon Energy of 1486.6 eV (photoelectron mean free path ≈ 1.6 nm) and another system with a tunable synchrotron source set to 645 eV (photoelectron mean free path ≈ 0.7 nm). As shown in Figure 6.2, the atomic fraction of Pd is significantly lower at the surface of the bimetallic nanoparticles than in the bulk. This demonstrates that the as-synthesized nanoparticles have clear core-shell geometry, with Pd as the core and Rh as the shell. As previously reported, however, changes in the local chemical environment dramatically affect the surface composition and oxidation state of the nanocrystals by inducing selective phase-segregation of the nanoparticle components[17].

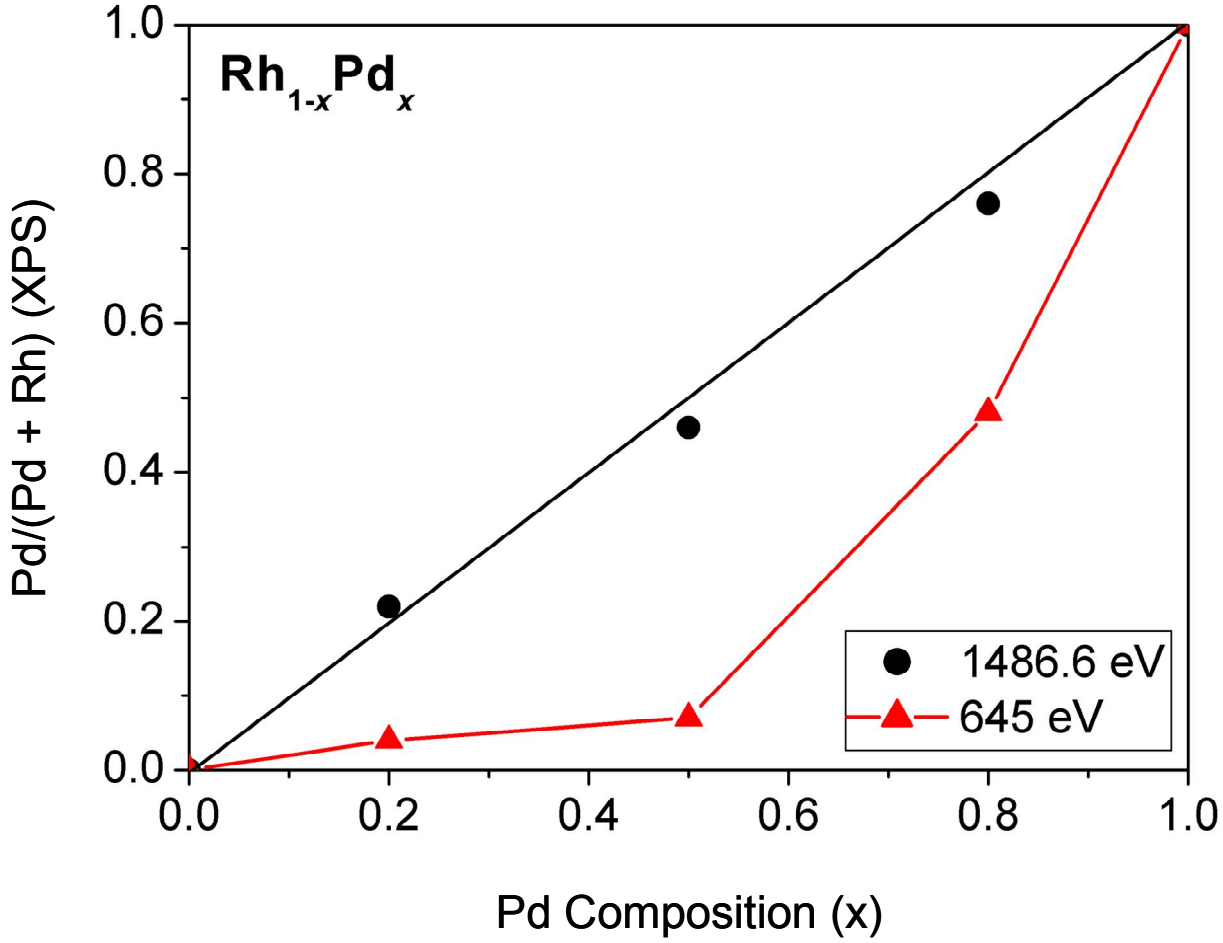

Figure 6.2 Pd atomic fraction of the $Rh_{1-x}Pd_x$ nanocrystals in UHV determined at X-ray energies of 1486.6 eV and 645 eV by XPS versus as-synthesized total Pd composition. The Pd core-Rh shell structure of the nanoparticles is clearly demonstrated by these results.

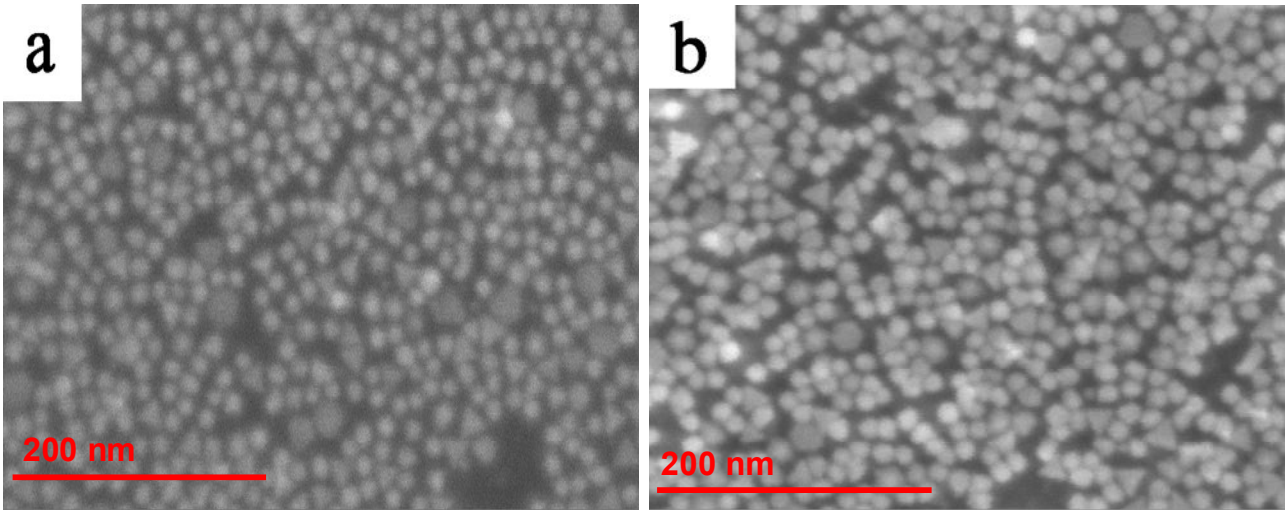

Figure 6.3 SEM images of $Rh_{0.6}Pd_{0.4}$ nanocrystals (a) before and (b) after CO oxidation.

6.4. Results

CO oxidation tests in 40 Torr CO, 100 Torr O_2 and 620 Torr He revealed that all the bimetallic nanocrystals are active for CO oxidation between 170 - 210°C. SEM measurements before and after reaction showed that no severe aggregation occurred, as shown in Figure 6.3. The turnover frequency was strongly dependent on nanoparticle composition, as shown at 180°C and 190°C in Figure 6.4a. The maximum turnover frequency was 1.34 molec $site^{-1}$ s^{-1} at 190°C on the $Rh_{0.6}Pd_{0.4}$ nanocrystals. Turnover frequencies were also compared to a theoretical linear-combination of pure Rh and pure Pd nanocrystals, calculated as $TOF_{Linear\text{-}Combination} = (TOF_{Rh} * (1\text{-}x)) + (TOF_{Pd} * x)$. The maximum measured enhancement was 5.0x at 180°C for the $Rh_{0.2}Pd_{0.8}$ nanocrystal versus a comparable theoretical linear combination of the pure nanoparticles. The enhancement factor decreased with increasing temperature for all samples.

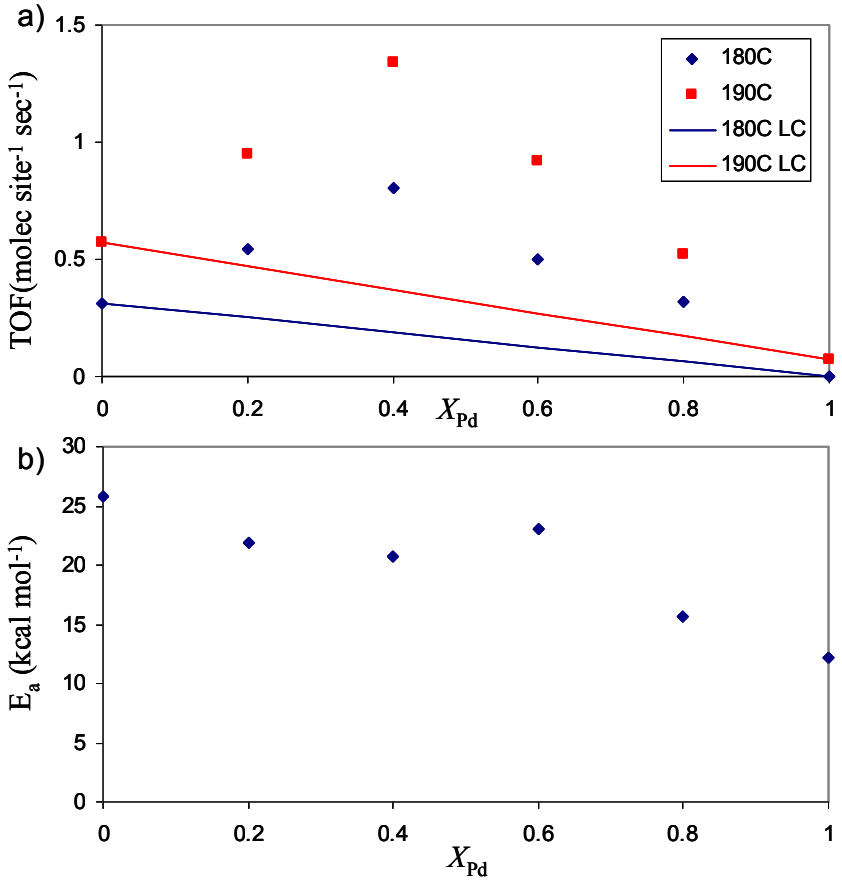

Figure 6.4 a) Turnover frequency at 180°C and 190°C and b) activation energy as a function of Pd molar fraction for $Rh_{1-x}Pd_x$ nanocrystals in 100 torr O_2, 40 torr CO, 620 torr He. Solid lines represent theoretical linear combination of pure Rh and Pd nanocrystal activity.

The apparent activation energies are reported in Figure 6.4b. Apparent activation energy was also strongly dependent on nanoparticle composition. It decreased with increased Pd molar fraction, from a maximum of 25.7 kcal mol^{-1} for pure Rh to a minimum of 12.2 kcal mol^{-1} for pure Pd nanoparticles. This trend is consistent with studies on pure Rh and Pd nanoparticles [19, 20].

6.5. Discussion

Figure 6.4a shows enhancements too large to be explained simply by complete coverage of the nanoparticle surface with Rh, which indicates that the synergetic effect must be due to interaction between Rh and Pd or their adsorbates. Our data is consistent with previous studies, which found synergistic behavior in Rh-Pd catalysts prepared by sequential impregnation and co-impregnation [7, 16, 21, 22] and lower ignition temperature for Rh nanoparticle catalysts as compared to Pd nanoparticle catalysts studied in similar conditions [22-24]. Previous studies also determined that synergism does not occur in physical mixtures in this system [22, 25].

One mechanism, which was originally proposed for Rh-Pt by Oh and Carpenter[25] and later extended to Rh-Pd by Araya and Diaz[7], is that surface oxygen from RhO_x species may react with CO adsorbed on reduced Pt atoms. This mechanism can be extended, however, by recent work by Gao et al. on a AuPd (100) system in CO oxidation, for which isolated Pd atoms at the

surface were found to become blocked by adsorbed CO because they cannot effectively adsorb O_2[2]. In our case, APXPS on a similar $Rh_{0.5}Pd_{0.5}$ system by our group found that at 300°C in 100 mTorr O_2, Rh is almost entirely oxidized while Pd is comparatively very metallic and an excess of O_2 causes Rh to segregate preferentially to the catalyst surface[17]. It is possible, then, that the preferential adsorption of CO on isolated Pd atoms, which effectively blocked reaction in Gao et al.'s study, may lead directly to the synergetic increase in reaction rate observed here because isolated Pd on the Rh-dominated surface ensures an adequate supply of adsorbed CO for the reaction while the oxidation of Rh, as found in APXPS, indicates that oxygen dissociatively adsorbs on Rh. In this model, the reaction rate is increased by reaction at Pd sites between oxygen spillover from Rh and the CO-covered Pd site, as diagrammed in Figure 6.5. In this case, the synergetic effect is heavily dependent on the distribution of Rh and Pd in the top layers.

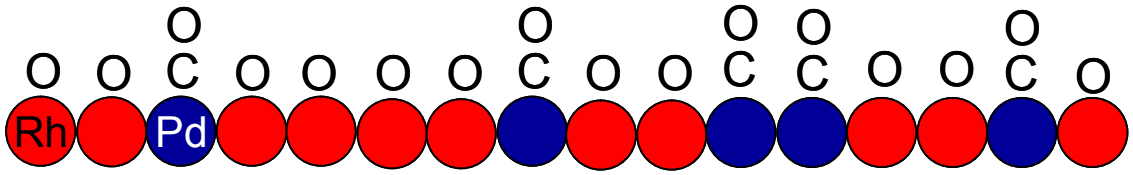

Figure 6.5 Cartoon representation of proposed behavior of CO/O_2 reaction on $Rh_{1-x}Pd_x$ bimetallic core-shell nanoparticle catalysts. CO adsorbs preferentially on Pd sites while O_2 dissociatively adsorbs preferentially on Rh sites.

Another compelling piece of evidence is found in the differences between the measured enhancements in this study and similar studies by Yoon et al.[22] and Araya and Weissman[16]. Although each study used different conditions, the differences in the conditions seem closely related to the measured enhancement. Our study, as previously stated, was carried out in P_{O2}/P_{CO} = 2.5 at 180°C and 190°C, while Weissman et al.'s study was carried out at in P_{O2}/P_{CO} = 5 at 135°C and Yoon et al.'s study was in P_{O2}/P_{CO} = 1 at 180°C. Weissman et al.'s study, which had the highest P_{O2}/P_{CO} ratio, also found the highest synergetic enhancement, while Yoon et al.'s study, with the lowest P_{O2}/P_{CO} ratio, found the lowest synergetic enhancement, and the present study, with an intermediate P_{O2}/P_{CO} ratio, found an intermediate synergetic enhancement. It is important to note that this correlation is independent of reaction order because these enhancements are relative to linear combinations of pure Pd and pure Rh catalyst activity. Although it is always difficult to compare studies by different groups in different conditions, if the correlation between synergy and oxygen is real, this indicates that at high oxygen pressures, the increased isolation of Pd sites in the ever more Rh-dominated surface (as shown by APXPS[17]) does not decrease the reaction rate – a finding that is to be expected if the model proposed above is correct. Further studies focused on the role of oxidation state and surface segregation in synergetic catalysis may shed more light on the true mechanism underlying these effects.

6.6. Conclusions

15 nm $Rh_{1-x}Pd_x$ Pd-core Rh-shell nanocrystals were synthesized, characterized, and studied in catalytic CO oxidation. A simple model based on available literature was proposed to help explain the observed catalytic behavior. The nanocrystals were found to exhibit significant composition-dependent synergetic effects in CO oxidation. This observed synergy appears to be related to preferential adsorption of CO on isolated Pd atoms or islands on the bimetallic catalyst surface and spillover of oxygen adsorbates from Rh to CO-covered Pd reaction sites. These

results demonstrate unique and desirable synergetic behavior in bimetallic core-shell catalysts and will hopefully lead to greater understanding of the many complex factors governing reactivity in these systems.

6.7. References

1. Stamenkovic, V. R.; Fowler, B.; Mun, B. S.; Wang, G. F.; Ross, P. N.; Lucas, C. A.; Markovic, N. M., Improved oxygen reduction activity on Pt3Ni(111) via increased surface site availability. *Science* **2007,** *315* (5811), 493-497.
2. Gao, F.; Wang, Y. L.; Goodman, D. W., CO Oxidation over AuPd(100) from Ultrahigh Vacuum to Near-Atmospheric Pressures: CO Adsorption-Induced Surface Segregation and Reaction Kinetics. *Journal of Physical Chemistry C* **2009,** *113* (33), 14993-15000.
3. Giraldo, S. A.; Pinzon, M. H.; Centeno, A., Behavior of catalysts with rhodium in simultaneous hydrodesulfurization and hydrogenation reactions. *Catalysis Today* **2008,** *133*, 239-243.
4. Shen, Q.; Li, L. D.; Hao, Z. P.; Xu, Z. P., Highly active and stable bimetallic Ir/Fe-USY catalysts for direct and NO-assisted N2O decomposition. *Applied Catalysis B-Environmental* **2008,** *84* (3-4), 734-741.
5. Zhang, J. G.; Wang, H.; Dalai, A. K., Development of stable bimetallic catalysts for carbon dioxide reforming of methane. *Journal of Catalysis* **2007,** *249* (2), 300-310.
6. Zhang, Y. W.; Huang, W. Y.; Habas, S. E.; Kuhn, J. N.; Grass, M. E.; Yamada, Y.; Yang, P.; Somorjai, G. A., Near-monodisperse Ni-Cu bimetallic nanocrystals of variable composition: Controlled synthesis and catalytic activity for H-2 generation. *Journal of Physical Chemistry C* **2008,** *112* (32), 12092-12095.
7. Araya, P.; Diaz, V., Synergism in the reaction of CO with O-2 on bimetallic Rh-Pd catalysts supported on silica. *Journal of the Chemical Society-Faraday Transactions* **1997,** *93* (21), 3887-3891.
8. Granger, P.; Delannoy, L.; Leclercq, L.; Leclercq, G., On the effect of deactivation on the kinetics of CO oxidation by NO over Pt-Rh catalysts. *Journal of Catalysis* **1998,** *177* (1), 147-151.
9. Lim, B.; Jiang, M. J.; Camargo, P. H. C.; Cho, E. C.; Tao, J.; Lu, X. M.; Zhu, Y. M.; Xia, Y. A., Pd-Pt Bimetallic Nanodendrites with High Activity for Oxygen Reduction. *Science* **2009,** *324* (5932), 1302-1305.
10. Frank, M.; Andersson, S.; Libuda, J.; Stempel, S.; Sandell, A.; Brena, B.; Giertz, A.; Bruhwiler, P. A.; Baumer, M.; Martensson, N.; Freund, H. J., Particle size dependent CO dissociation on alumina-supported Rh: a model study (vol 279, pg 92, 1997). *Chem. Phys. Lett.* **1999,** *310* (1-2), 229-230.
11. Grass, M. E.; Zhang, Y. W.; Butcher, D. R.; Park, J. Y.; Li, Y. M.; Bluhm, H.; Bratlie, K. M.; Zhang, T. F.; Somorjai, G. A., A Reactive Oxide Overlayer on Rhodium Nanoparticles during CO Oxidation and Its Size Dependence Studied by In Situ Ambient-Pressure X-ray Photoelectron Spectroscopy. *Angewandte Chemie-International Edition* **2008,** *47* (46), 8893-8896.

12. Schlatter, J. C.; Taylor, K. C., PLATINUM AND PALLADIUM ADDITION TO SUPPORTED RHODIUM CATALYSTS FOR AUTOMOTIVE EMISSION CONTROL. *Journal of Catalysis* **1977,** *49* (1), 42-50.
13. Gao, F.; Cai, Y.; Gath, K. K.; Wang, Y.; Chen, M. S.; Guo, Q. L.; Goodman, D. W., CO Oxidation on Pt-Group Metals from Ultrahigh Vacuum to Near Atmospheric Pressures. 1. Rhodium. *Journal of Physical Chemistry C* **2009,** *113* (1), 182-192.
14. Gustafson, J., Westerstrom, R., Resta, A., Mikkelsen, A., Andersen, J.N., Balmes, O., Torrelles, X., Schmid, M., Varga, P., Hammer, B., Kresse, G., Baddeley, C.J., Lundgren, E., Structure and catalytic reactivity of Rh oxides. *Catalysis Today* **2009**.
15. Cortes, J.; Valencia, E.; Aguila, G.; Orellana, E.; Araya, P., Time Decay of the Activity of the Reduction Reaction of NO by CO on a Pd/Al2O3 Catalyst. *Catalysis Letters* **2008,** *126* (1-2), 63-71.
16. Araya, P.; Weissmann, C., FTIR study of the oxidation reaction of CO with O-2 over bimetallic Pd-Rh/SiO2 catalysts in an oxidized state. *Catalysis Letters* **2000,** *68* (1-2), 33-39.
17. Tao, F.; Grass, M. E.; Zhang, Y. W.; Butcher, D. R.; Renzas, J. R.; Liu, Z.; Chung, J. Y.; Mun, B. S.; Salmeron, M.; Somorjai, G. A., Reaction-Driven Restructuring of Rh-Pd and Pt-Pd Core-Shell Nanoparticles. *Science* **2008,** *322* (5903), 932-934.
18. Song, H.; Kim, F.; Connor, S.; Somorjai, G. A.; Yang, P. D., Pt nanocrystals: Shape control and Langmuir-Blodgett monolayer formation. *J. Phys. Chem. B* **2005,** *109* (1), 188-193.
19. Choi, K. I.; Vannice, M. A., CO OXIDATION OVER PD AND CU CATALYSTS .3. REDUCED AL2O3-SUPPORTED PD. *Journal of Catalysis* **1991,** *131* (1), 1-21.
20. Oh, S. H.; Eickel, C. C., INFLUENCE OF METAL-PARTICLE SIZE AND SUPPORT ON THE CATALYTIC PROPERTIES OF SUPPORTED RHODIUM - CO-O2 AND CO-NO REACTIONS. *Journal of Catalysis* **1991,** *128* (2), 526-536.
21. Araya, P.; Diaz, V.; Cortes, J., Reducibility of bimetallic Pd-Rh catalysts and its relation with synergism in the oxidation reaction of CO with O-2. *Journal of Chemical Research-S* **1998,** (4), 194-195.
22. Yoon, K. J.; Kang, H. K.; Yie, J. E., Synergism and kinetics in CO oxidation over palladium-rhodium bimetallic catalysts. *Korean Journal of Chemical Engineering* **1997,** *14* (5), 399-406.
23. Araya, P.; Berrios, J. P.; Wolf, E. E., Activity and infrared studies during carbon monoxide oxidation over bimetallic palladium-rhodium/silica catalysts. *Applied Catalysis A: General* **1992,** *92* (1), 17-27.
24. Santra, A. K.; Goodman, D. W., Catalytic oxidation of CO by platinum group metals: from ultrahigh vacuum to elevated pressures. *Electrochimica Acta* **2002,** *47* (22-23), 3595-3609.
25. Oh, S. H.; Carpenter, J. E., PLATINUM RHODIUM SYNERGISM IN 3-WAY AUTOMOTIVE CATALYSTS. *Journal of Catalysis* **1986,** *98* (1), 178-190.

Chapter 7. $Rh_{1-x}Pd_x$ Nanoparticle Composition Dependence in CO Oxidation by NO

Bimetallic 15 nm Pd-core Rh-shell $Rh_{1-x}Pd_x$ nanoparticle catalysts have been synthesized and studied in CO oxidation by NO. The catalysts exhibited composition-dependent activity enhancement (synergy) in CO oxidation in high NO pressures. The observed synergy is caused by favorable adsorption of CO on Pd in NO-rich conditions. After many hours of oxidation of CO by NO, the Pd-rich bimetallic catalysts deactivated and product formation was proportional to Rh molar fraction. The deactivation is caused by the adsorption of nitrogen atoms on Pd sites.

7.1. Introduction

In the years since the introduction of the three-way catalytic convertor in the 1970s for NO_x reduction and the oxidation of carbon monoxide from automobile exhaust, there has been an intensive effort to understand the fundamental mechanisms underlying these catalytic systems[1]. Despite these efforts, however, efforts to find an appropriate catalyst with high activity for NO_x removal have been met with limited success because of catalyst poisoning from strongly-bound oxygen adsorbates left on the surface from NO dissociation[2]. Rhodium is acknowledged to be the best catalyst for this reaction, with intense efforts devoted to understanding its behavior[3-13]. However, in recent years much research has also been aimed at understanding the role of Pd in the reaction[1-3, 14-19] because of the relatively high cost of rhodium catalysts, palladium's improved resistance to sintering, and because new improvements in gasoline purification have helped reduce the significance of previous problems with Pd site poisoning by sulfur and lead[15]. Pd has been found to have lower activity than Rh for the reaction of NO with CO[16] and has also been shown to suffer from deactivation[14]. The origin of this deactivation has not been definitively identified.

Current developments in the synthesis of structured bimetallic nanoparticle systems have also enabled the study of unique new catalyst systems that were not possible in the past[20]. These new systems can sometimes improve upon the catalytic performance of previous monometallic systems[21-25]. It has become apparent that these new catalyst systems may provide pathways to increase reactivity and decrease deactivation under the right conditions. The use of a combination of Rh and Pd has been studied for the oxidation of CO by O_2[21, 25-27], as well as in Chapter 6 of this work, but there has been limited progress on the study of the oxidation of CO by NO[28, 29]. Recently, this system was shown to be of particular interest in ambient pressure XPS experiments conducted by our group at the Advanced Light Source at Lawrence Berkeley National Laboratory, which clearly demonstrated surface-segregation behavior for Pd core-Rh shell nanoparticles in this reaction[20]. This work established the surface state of the system in reaction conditions, but did not include kinetic studies. These kinetic studies are necessary in order to correlate the surface condition of the core-shell nanoparticle structures with real catalytic behavior. The understanding of the kinetic behavior of these core-shell Rh-Pd nanoparticle catalysts in the NO + CO reaction is important to the understanding both of the reaction itself, but also of the behavior of complex core-shell nanoparticle systems in general.

In this Chapter, we report the catalytic activity of $Rh_{1-x}Pd_x$ nanocrystals for the oxidation of CO by NO and models are proposed to explain the complex behavior in each reaction.

7.2. Experimental Details

The synthesis and characterization of the $Rh_{1-x}Pd_x$ nanoparticles used in this study are identical to that which was presented in Sections 6.2 and 6.3 of this work. The NO + CO reactions were performed in the chamber described in Section 6.4. The reaction was run from 220 - 260°C on the $Rh_{1-x}Pd_x$ nanocrystals in batch mode in 8 Torr CO, 8-120 Torr NO, and 632-744 Torr He, such that the total pressure was always 760 Torr. This temperature range was chosen to ensure adequate turnover for the nanocrystal samples without significant morphological change or particle aggregation. Turnover frequency was calculated independently for formation of each product, CO_2, N_2, and N_2O.

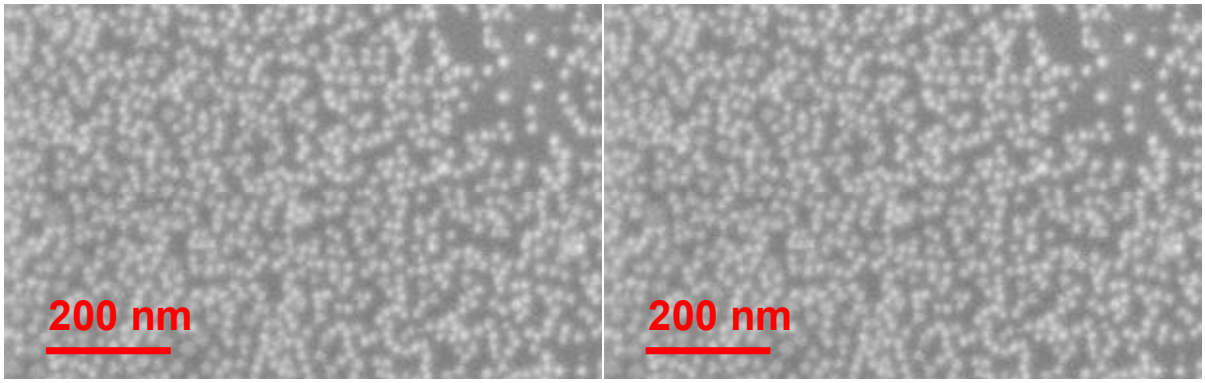

Figure 7.1 SEM of $Rh_{0.5}Pd_{0.5}$ a) before and b) after reaction in 8 torr NO, 8 torr CO, 744 torr He at 260°C. No significant morphological change is observed after reaction at this temperature.

7.3. Results

NO reduction by CO was carried out in 8 Torr NO, 8 Torr CO, and 744 Torr He carrier gas. The nanocrystals were stable in reaction at 260°C, as shown by SEM in Figure 7.1, but underwent significant morphological change at 275°C. Consequently, the reaction temperature was kept at 260°C and below for all experiments presented here.

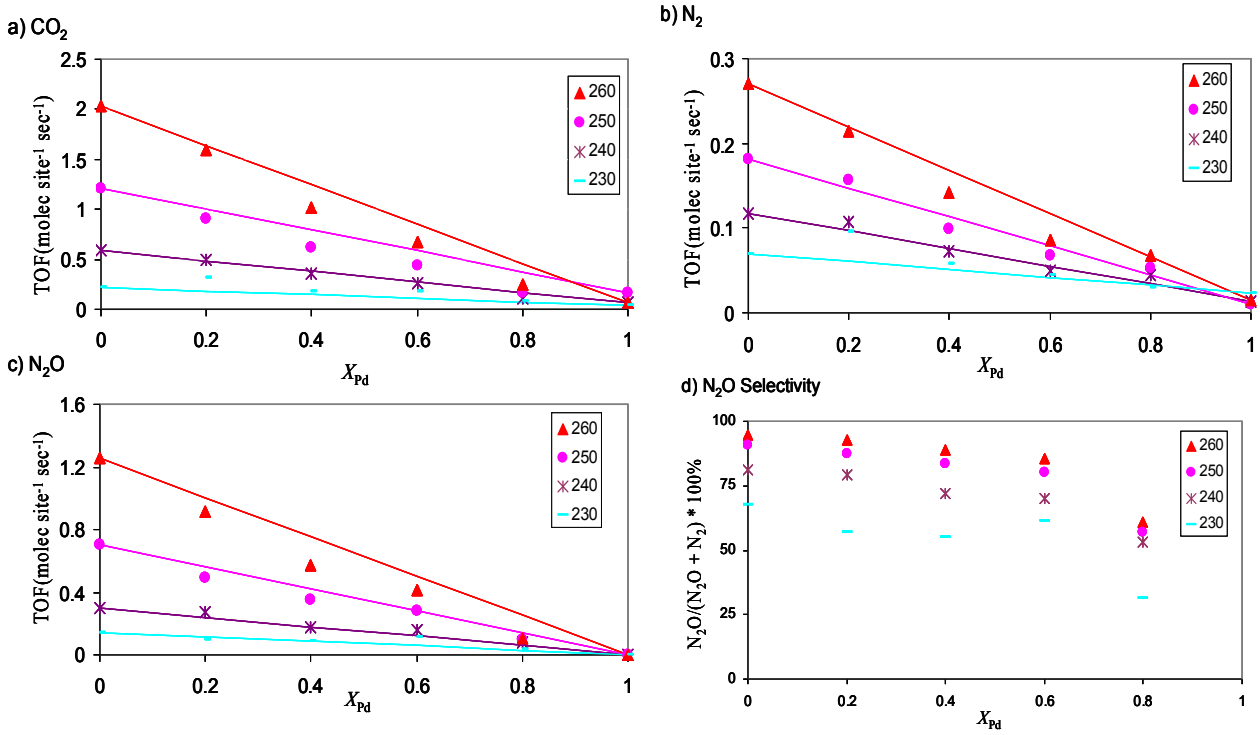

Figure 7.2 Turnover frequency for formation of a) CO_2, b) N_2, and c) N_2O products and Selectivity towards N_2O as a function of Pd molar fraction for $Rh_{1-x}Pd_x$ nanocrystals in 8 torr NO, 8 torr CO, 744 torr He from 230 – 260°C. Solid lines represent theoretical linear combination of pure Rh and Pd nanocrystal activity.

Turnover frequencies versus Pd molar fraction at 230°C, 240°C, 250°C, and 260°C for the formation of CO_2, N_2, and N_2O are presented in Figures 7.2 a, b, and c, respectively. Turnover frequency decreased with increased Pd molar fraction and increased with temperature for all products. At high temperature, the bimetallic nanocrystals underperformed relative to a theoretical linear combination of pure Rh and pure Pd nanocrystals, based on the performance of the Rh and Pd nanocrystals studied here. Selectivity towards N_2O, defined as $S = TOF_{N2O}/(TOF_{N2O} + TOF_{N2}) *100\%$, is presented in Figure 7.2d and is found to decrease with increased molar fraction of Pd in this temperature range.

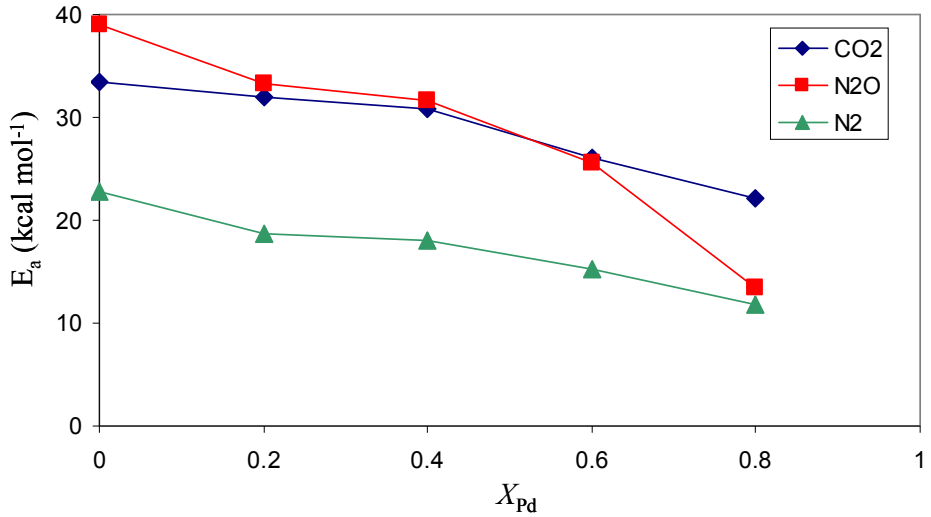

Figure 7.3 Activation energy for formation of CO_2, N_2O, and N_2 products as a function of Pd molar fraction for $Rh_{1-x}Pd_x$ nanocrystals in 8 torr NO, 8 torr CO, 744 torr He from 230 – 260°C. The low activity of the pure Pd nanocrystals made determination of an accurate activation energy difficult for those samples.

Experimentally measured activation energies for the formation of the CO_2, N_2O, and N_2 products in 8 Torr NO, 8 Torr CO, and 744 Torr He are presented in Figure 7.3. Activation energy was found to decrease with increased Pd molar fraction for all products. No activation energies are presented for the 100% Pd nanocrystals due to extremely low turnover frequencies for all products and all temperatures in the reaction on this catalyst in these conditions. These results compare relatively well to previous studies on Rh and Pd nanoparticle catalysts, such as studies by Granger et al., who found higher turnover rates and activation energies on Rh/Al_2O_3 catalysts as compared to Pd/Al_2O_3 catalysts[16]. No synergism was observed in these conditions with the $Rh_{1-x}Pd_x$ nanocrystals.

The reaction between NO and CO was also carried out under a majority of NO, in 80 Torr NO, 8 Torr CO, and 672 Torr He and a stepped temperature ramp from 230 -260°C in 10°C increments with 3 hours at each step. Figure 7.4a demonstrates that at 230°C, prior to deactivation, the Pd-rich catalysts were more active for CO_2 production than the Rh-rich catalysts or an identical catalyst in 8 Torr NO. For example, the $Rh_{0.2}Pd_{0.8}$ catalysts produced eleven times more CO_2 in 80 Torr NO than in 8 Torr NO at 230°C. Interestingly, N_2O and N_2 production were not significantly enhanced.

After 3 hours at both 230°C and 240°C, the Pd-rich nanoparticles deactivated. The deactivation was relatively abrupt and exhibited a strong dependence on the composition of the bimetallic catalyst. The catalyst activity after deactivation was typically similar to a linear combination of Rh and Pd monometallic catalyst for all three products. Although decreasing the temperature in reaction did not restore the pre-deactivation activity, heating the sample to 150°C in UHV for one hour was found to restore the catalyst.

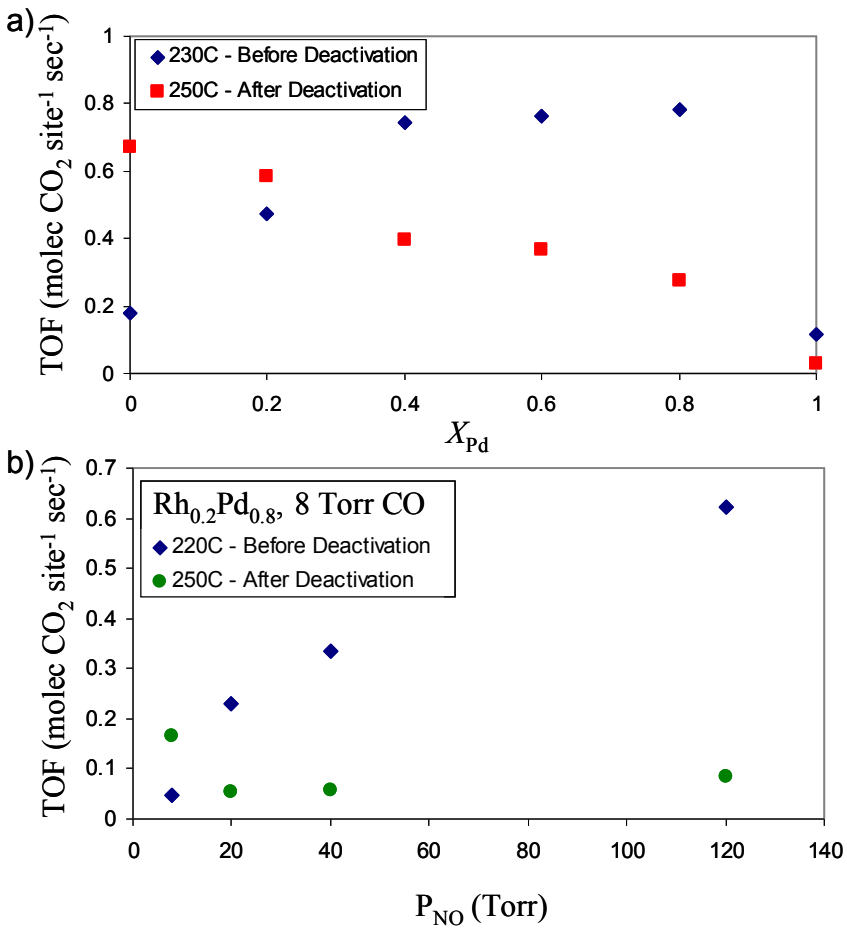

Figure 7.4 a) TOF of CO_2 as a function of Pd molar fraction for $Rh_{1-x}Pd_x$ nanocrystals at 230°C before deactivation and 250°C after deactivation in 80 Torr NO, 8 Torr CO, and 672 Torr He. b) TOF of CO_2 as a function of NO pressure for $Rh_{0.2}Pd_{0.8}$ nanocrystals in 8 Torr CO and a total pressure of 760 Torr equalized with He. Deactivation plays a significant role in the behavior of Pd-rich $Rh_{1-x}Pd_x$ bimetallic nanocrystals at elevated NO pressures.

The role of NO pressure in the activity of the Pd-rich nanocatalysts was further investigated using a stepped temperature ramp from 220 -250°C in 10°C increments with 3 hours at each step, a fixed CO pressure of 8 Torr, and NO pressures ranging from 20 – 120 Torr. The turnover frequency of CO_2 is presented in Figure 7.4b for each condition. Interestingly, at 220°C, prior to deactivation, the turnover frequency was strongly dependent on P_{NO}, whereas the turnover frequency was virtually independent of P_{NO} at 250°C, after deactivation. N_2O and N_2 production followed similar trends to the 80 Torr NO condition discussed above. Again, heating the sample to 150°C in UHV for one hour was found to restore the catalyst activity.

7.4. Discussion

In their monometallic state, these two metals have very different catalytic behavior in this reaction. The Rh nanoparticles were very active, had a moderate decrease in elevated pressures of NO, and did not undergo significant deactivation. These results are consistent with previous studies on Rh catalysts in this reaction, which found that supported Rh nanoparticles show

decreased activity with increased NO pressure at 538K[30] and that Rh shows very little deactivation for this reaction[31]. The Pd nanoparticles, however, were significantly less active in all conditions and deactivated at elevated pressure of NO. These results, again, are consistent with previous studies on Pd catalysts in this reaction, which found that the activity of Pd is positive order in NO[32], and the deactivation behavior of Pd is quite significant[14, 15].

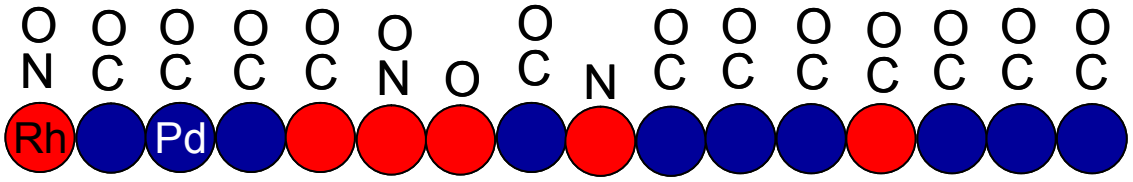

Figure 7.5 Cartoon representation of proposed behavior of CO/NO reaction on $Rh_{1-x}Pd_x$ bimetallic core-shell nanoparticle catalysts in $P_{NO} = P_{CO}$ conditions. In these conditions, Rh is reduced and Pd preferentially segregates to the surface. No synergy occurs because the surface is predominantly CO-covered in this regime.

The behavior of the bimetallic catalysts in the $P_{NO} = P_{CO}$ condition is fairly similar to the behavior of a linear combination of monometallic catalyst. No synergy is observed and the catalyst activity is slightly worse than an equivalent linear combination of monometallic catalyst, perhaps due to Pd-enrichment in the surface layers in this condition, which is the most reducing condition in this study. This observation is consistent with APXPS data, which showed that Pd is slightly enriched on the surface and Rh is almost completely metallic when $P_{NO} = P_{CO}$ at 300°C[20]. The metallic nature of the Rh surface indicates that NO is not rapidly dissociated by Rh in these conditions. The proposed surface in the $P_{NO} = P_{CO}$ condition is diagrammed in Figure 7.5.

In the $P_{NO} > P_{CO}$ condition, however, the bimetallic catalysts showed markedly different behavior. The observed synergy and subsequent deactivation indicate that the Rh and Pd catalyst components are interacting in important ways, as was observed in CO oxidation. The model we propose is that prior to deactivation, isolated Pd atoms serve as preferential adsorption sites for CO, as previously postulated for the CO oxidation reaction in Chapter 6, while high pressure of NO favors dissociative adsorption of NO on Rh. The CO_2 formation step in the reaction occurs when oxygen adsorbates spillover from Rh to Pd and react with CO molecules adsorbed on Pd. N_2O and N_2 formation were not significantly enhanced in this regime, which indicates that the presence of Pd does not play a significant role in those reaction steps for these catalysts. In this model, diagrammed in Figure 7.6 (top), Pd effectively acts as a promoter, facilitating adsorption of CO while Rh dissociates NO.

This model is well-supported by existing literature. It is known that the efficient dissociative adsorption of NO on monometallic Rh is self-inhibited at high NO coverages, which limits the coverage of CO on the surface and thus the reaction rate[11]. It is also known that NO adsorption is relatively unfavorable on Pd[33], which may enable CO to adsorb even in NO-rich conditions. Additionally, infrared spectroscopy on Rh/Al_2O_3 and Pd/Al_2O_3 by Granger et al., found that the reaction rate is highest when the coverage of NO is much greater than CO but not high enough to be inhibiting, and that CO adsorbs preferentially on 10 wt.% Pd/Al_2O_3, which has a crystallite size comparable to the nanoparticle size in the present study[16]. We also know from our APXPS experiments that Rh atoms segregate to the surface and oxidize in NO, even after previous exposure to CO[20]. Although it is possible for NO to adsorb molecularly on Rh, the strong Rh oxidation observed in APXPS implies that a significant portion of NO is dissociatively adsorbed. Together, this data supports the notion that CO adsorption on Pd sites in the bimetallic catalyst in combination with oxygen spillover from NO molecules dissociatively adsorbed on Rh

sites in high pressure of NO is likely to increase the CO_2 production of the catalyst prior to deactivation.

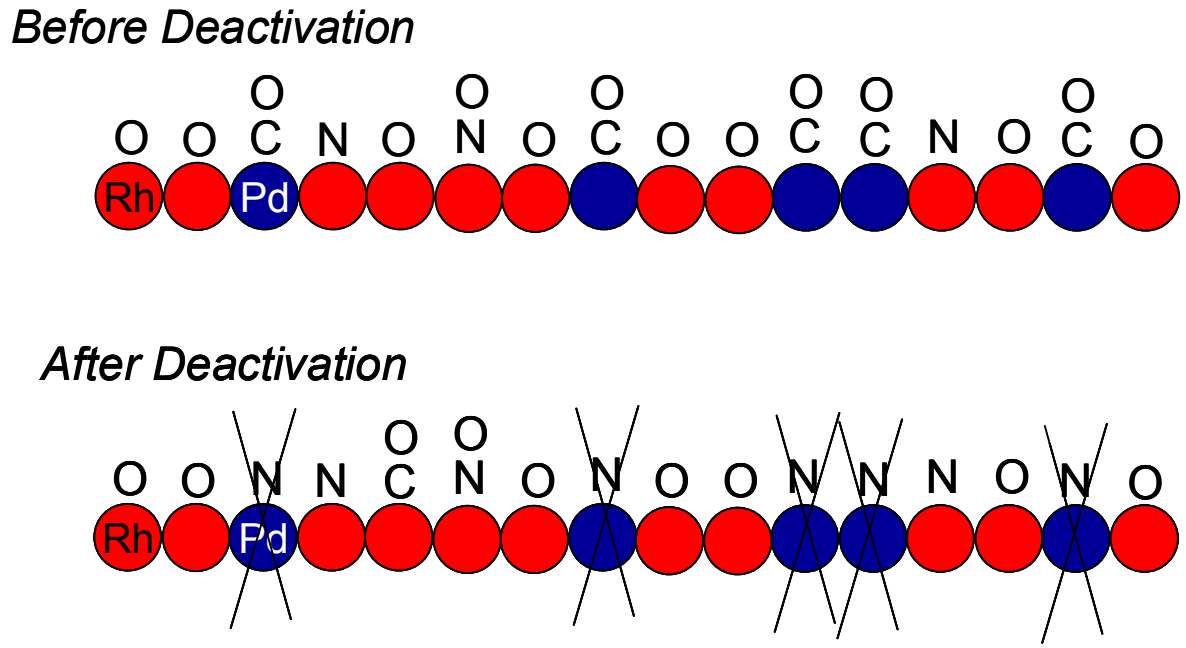

Figure 7.6 Cartoon representation of proposed behavior of CO/NO reaction on $Rh_{1-x}Pd_x$ bimetallic core-shell nanoparticle catalysts in $P_{NO} >> P_{CO}$ conditions. In these conditions, Rh oxidizes and segregates preferentially to the surface. On a monometallic Rh catalyst, the reaction is known to be self-inhibited by high coverage of NO. On this surface, however, prior to deactivation (top), Pd provides adsorption sites for CO. The surface is eventually deactivated (bottom) by the diffusion of N-adsorbates across the surface to Pd sites, with which they form strong N-Pd surface adsorbate bonds, poisoning the Pd sites and effectively leaving the catalyst with only Rh sites available for reaction. The activity of this pseudo-monometallic surface then mirrors that of a monometallic Rh catalyst, for which the reaction rate is self-inhibited by the high coverage of NO.

The cause of deactivation on the Pd-rich bimetallic catalysts is also of considerable interest. In this case, the most probable explanation is that Pd is eventually poisoned by spillover of N atoms from Rh. This model is supported by the work of Vesecky, Rainer, and Goodman, who used Temperature Programmed Desorption (TPD) to show that high surface area Pd catalysts and Pd (100) single crystals are poisoned by stable adsorbed nitrogen atoms, and that free surface oxygen is removed so quickly by CO to form CO_2 that it is unlikely to play a role in the catalyst deactivation[34]. This explanation for deactivation seems more likely than previously suggested mechanisms, such as reaction inhibition by carbon deposition on the surface[14] or self-inhibited NO adsorption on the Rh surface[11] because deactivation was not observed on the pure-Rh catalyst despite identical reaction conditions, and because the sample activity was closely correlated with the Rh molar fraction after deactivation. The importance of nitrogen in this deactivation is further supported by the observation that N_2O and N_2 production were not significantly enhanced prior to catalyst deactivation. This indicates that adsorbed nitrogen is not effectively removed from the catalyst surface.

In this scenario for deactivation, diagrammed in Figure 7.6 (bottom), once Pd is poisoned the catalytic activity is dominated by the availability of Rh sites on the catalyst surface because Pd can no longer act as a promoter. Figure 7.4a supports this notion, as the catalyst activity increased with Rh molar fraction in a roughly linear fashion at 250°C, after deactivation. If this is

indeed the case, the 150°C UHV heating step may restore activity by removing adsorbed nitrogen from the catalyst surface.

There are several outstanding considerations which must be taken into consideration in examining the simple synergetic and deactivation models suggested here. First, much of our model is predicated on our previous results in APXPS, but there is a pressure gap between that study, which was carried out at tenths of a Torr [20], and this study, which was carried out in tens of Torr of reaction gases mixed with He for a total pressure of one atmosphere. Since the entropic contribution of the Gibbs Free Energy increases as $kT \cdot \log P$, this pressure gap leads to an energy difference which ranges from 0.09 eV at 27°C and 0.18 eV at 300°C. Although this is a dramatic improvement from the 0.28 and 0.54 eV energy differences at 27°C and 300°C between reaction at atmosphere and analysis at 10^{-8} Torr, as required for traditional XPS or Auger analysis, further improvement is necessary. We are currently building a reactor capable of measuring kinetics in conditions identical to those used in APXPS which will enable even more precise study of the role of surface segregation and oxidation in catalysis.

In summary, NO reduction by CO is known to be an exceedingly complex reaction dependent on many subtle factors, such as stable islands of adsorbed N on Rh[19, 34-36] and the oxidation state of the metals[3, 37, 38]. Although the model proposed here is consistent with our kinetic data, further studies are needed to fully understand the initial catalyst behavior and subsequent deactivation of bimetallic Pd-core Rh-shell $Rh_{1-x}Pd_x$ nanocrystals.

7.5. Conclusions

15 nm $Rh_{1-x}Pd_x$ Pd-core Rh-shell nanocrystals were synthesized, characterized, and studied in the catalytic oxidation of CO by NO. Simple models based on available literature were proposed to help explain the observed catalytic behavior. Although no synergy was observed in the NO/CO reaction when $P_{NO} = P_{CO} = 8$ Torr, the Pd-rich bimetallic catalysts were very active at 80 Torr NO prior to undergoing deactivation. Pd enhances the reaction by ensuring adequate adsorption of CO in the high NO coverage regime. After many hours on stream, Pd is eventually poisoned by adsorbed N and reactivity is dominated by the availability of Rh surface sites. These results demonstrate unique and desirable synergetic behavior in bimetallic core-shell catalysts and will hopefully lead to greater understanding of the many complex factors governing reactivity in these systems.

7.6. References

1. Rainer, D. R.; Vesecky, S. M.; Koranne, M.; Oh, W. S.; Goodman, D. W., The CO+NO reaction over Pd: A combined study using single-crystal, planar-model-supported, and high-surface-area Pd/Al2O3 catalysts. *Journal of Catalysis* **1997,** *167* (1), 234-241.
2. Pisanu, A. M.; Gigola, C. E., NO decomposition and NO reduction by CO over Pd/[alpha]-Al2O3. *Applied Catalysis B: Environmental* **1999,** *20* (3), 179-189.
3. Almusaiteer, K.; Chuang, S. S. C., Dynamic behavior of adsorbed NO and CO under transient conditions on Pd/Al2O3. *Journal of Catalysis* **1999,** *184* (1), 189-201.
4. Araya, P.; Gracia, F.; Cortes, J.; Wolf, E. E., FTIR study of the reduction reaction of NO by CO over Rh/SiO2 catalysts with different crystallite size. *Applied Catalysis B-Environmental* **2002,** *38* (2), 77-90.

5. Avalos, L. A.; Bustos, V.; Unac, R.; Zaera, F.; Zgrablich, G., Toward a realistic model for the kinetics of the NO plus CO reaction on rhodium surfaces. *Journal of Molecular Catalysis a-Chemical* **2005,** *228* (1-2), 89-95.
6. Bustos, V.; Gopinath, C. S.; Unac, R.; Zaera, F.; Zgrablich, G., Lattice-gas study of the kinetics of catalytic conversion of NO-CO mixtures on rhodium surfaces. *Journal of Chemical Physics* **2001,** *114* (24), 10927-10931.
7. Herman, G. S.; Peden, C. H. F.; Schmieg, S. J.; Belton, D. N., A comparison of the NO-CO reaction over Rh(100), Rh(110) and Rh(111). *Catalysis Letters* **1999,** *62* (2-4), 131-138.
8. Hopstaken, M. J. P. Elementary Reaction Kinetics and Lateral Interactions in the Catalytic Reaction between NO and CO on Rhodium Surfaces. Eindhoven University of Technology, Eindhoven, The Netherlands, 2000.
9. Hopstaken, M. J. P.; Niemantsverdriet, J. W. In *Reaction between NO and CO on rhodium (100): How lateral interactions lead to auto-accelerating kinetics*, AVS: 2000; pp 1503-1508.
10. Peden, C. H. F.; Belton, D. N.; Schmieg, S. J., STRUCTURE SENSITIVE SELECTIVITY OF THE NO-CO REACTION OVER RH(110) AND RH(111). *Journal of Catalysis* **1995,** *155* (2), 204-218.
11. Permana, H.; Ng, K. Y. S.; Peden, C. H. F.; Schmieg, S. J.; Belton, D. N., EFFECT OF NO PRESSURE ON THE REACTION OF NO AND CO OVER RH(111). *Journal of Physical Chemistry* **1995,** *99* (44), 16344-16350.
12. Permana, H.; Ng, K. Y. S.; Peden, C. H. F.; Schmieg, S. J.; Lambert, D. K.; Belton, D. N., Adsorbed species and reaction rates for NO-CO over Rh(111). *Journal of Catalysis* **1996,** *164* (1), 194-206.
13. Renzas, J. R.; Zhang, Y.; Huang, W. Y.; Somorjai, G. A., Rhodium Nanoparticle Shape Dependence in the Reduction of NO by CO. *Catalysis Letters* **2009**.
14. Cortes, J.; Valencia, E.; Aguila, G.; Orellana, E.; Araya, P., Time Decay of the Activity of the Reduction Reaction of NO by CO on a Pd/Al2O3 Catalyst. *Catalysis Letters* **2008,** *126* (1-2), 63-71.
15. Cortes, J.; Valencia, E.; Herrera, J.; Araya, P., Mechanism and kinetics parameters of the reduction reaction of NO by CO on Pd/Al2O3 catalyst. *Journal of Physical Chemistry C* **2007,** *111* (19), 7063-7070.
16. Granger, P.; Dhainaut, F.; Pietrzik, S.; Malfoy, P.; Mamede, A. S.; Leclercq, L.; Leclercq, G., An overview: Comparative kinetic behaviour of Pt, Rh and Pd in the NO+CO and NO+H-2 reactions. *Topics in Catalysis* **2006,** *39* (1-2), 65-76.
17. Holles, J. H.; Davis, R. J.; Murray, T. M.; Howe, J. M., Effects of Pd particle size and ceria loading on NO reduction with CO. *Journal of Catalysis* **2000,** *195* (1), 193-206.
18. Kobal, I.; Kimura, K.; Ohno, Y.; Matsushima, T., Angular and velocity distributions of desorbing molecules in steady-state NO plus CO reaction on Pd(110). *Surf. Sci.* **2000,** *445* (2-3), 472-479.
19. Vesecky, S. M.; Chen, P. J.; Xu, X. P.; Goodman, D. W., EVIDENCE FOR STRUCTURE SENSITIVITY IN THE HIGH-PRESSURE CO+NO REACTION OVER PD(111) AND PD(100). *J. Vac. Sci. Technol. A-Vac. Surf. Films* **1995,** *13* (3), 1539-1543.
20. Tao, F.; Grass, M. E.; Zhang, Y. W.; Butcher, D. R.; Renzas, J. R.; Liu, Z.; Chung, J. Y.; Mun, B. S.; Salmeron, M.; Somorjai, G. A., Reaction-Driven Restructuring of Rh-Pd and Pt-Pd Core-Shell Nanoparticles. *Science* **2008,** *322* (5903), 932-934.

21. Araya, P.; Diaz, V., Synergism in the reaction of CO with O-2 on bimetallic Rh-Pd catalysts supported on silica. *Journal of the Chemical Society-Faraday Transactions* **1997,** *93* (21), 3887-3891.
22. Araya, P.; Diaz, V.; Cortes, J., Reducibility of bimetallic Pd-Rh catalysts and its relation with synergism in the oxidation reaction of CO with O-2. *Journal of Chemical Research-S* **1998,** (4), 194-195.
23. Basile, F.; Fornasari, G.; Trifirò, F.; Vaccari, A., Rh-Ni synergy in the catalytic partial oxidation of methane: surface phenomena and catalyst stability. *Catalysis Today* **2002,** *77* (3), 215-223.
24. Oh, S. H.; Carpenter, J. E., PLATINUM RHODIUM SYNERGISM IN 3-WAY AUTOMOTIVE CATALYSTS. *Journal of Catalysis* **1986,** *98* (1), 178-190.
25. Yoon, K. J.; Kang, H. K.; Yie, J. E., Synergism and kinetics in CO oxidation over palladium-rhodium bimetallic catalysts. *Korean Journal of Chemical Engineering* **1997,** *14* (5), 399-406.
26. Araya, P.; Berrios, J. P.; Wolf, E. E., Activity and infrared studies during carbon monoxide oxidation over bimetallic palladium-rhodium/silica catalysts. *Applied Catalysis A: General* **1992,** *92* (1), 17-27.
27. Araya, P.; Weissmann, C., FTIR study of the oxidation reaction of CO with O-2 over bimetallic Pd-Rh/SiO2 catalysts in an oxidized state. *Catalysis Letters* **2000,** *68* (1-2), 33-39.
28. Mergler, Y. J.; Ramsaransing, D. R. G.; Nieuwenhuys, B. E., AN INFRARED SPECTROSCOPIC STUDY OF CO AND NO ADSORPTION ON BIMETALLIC PD-RH/SIO2 CATALYSTS. *Recueil Des Travaux Chimiques Des Pays-Bas-Journal of the Royal Netherlands Chemical Society* **1994,** *113* (10), 431-438.
29. Araya, P.; Ferrada, C.; Cortes, J., ACTIVITY DURING REDUCTION OF NO BY CO OVER BIMETALLIC PALLADIUM RHODIUM/SILICA CATALYSTS. *Catalysis Letters* **1995,** *35* (1-2), 175-181.
30. Oh, S. H.; Fisher, G. B.; Carpenter, J. E.; Goodman, D. W., COMPARATIVE KINETIC-STUDIES OF CO-O2 AND CO-NO REACTIONS OVER SINGLE-CRYSTAL AND SUPPORTED RHODIUM CATALYSTS. *Journal of Catalysis* **1986,** *100* (2), 360-376.
31. Cortes, J.; Valencia, E., Monte Carlo studies (MCLH simulations) of the CO-NO reaction on disordered substrates and their relation with experiments. *J. Phys. Chem. B* **2004,** *108* (9), 2979-2986.
32. Muraki, H.; Shinjoh, H.; Fujitani, Y., REDUCTION OF NO BY CO OVER ALUMINA-SUPPORTED PALLADIUM CATALYST. *Industrial & Engineering Chemistry Product Research and Development* **1986,** *25* (3), 419-424.
33. Loffreda, D.; Simon, D.; Sautet, P., Molecular and dissociative chemisorption of NO on palladium and rhodium (100) and (111) surfaces: A density-functional periodic study. *Journal of Chemical Physics* **1998,** *108* (15), 6447-6457.
34. Vesecky, S. M.; Rainer, D. R.; Goodman, D. W. In *Basis for the structure sensitivity of the CO+NO reaction on palladium*, 1996; pp 1457-1463.
35. Zaera, F.; Sales, J. L.; Gargiulo, M. V.; Ciacera, M.; Zgrablich, G., On the formation of nitrogen islands on rhodium surfaces. *Journal of Physical Chemistry C* **2007,** *111* (21), 7795-7800.
36. Zaera, F.; Gopinath, C. S., Effect of coverage and temperature on the kinetics of nitrogen desorption from Rh(111) surfaces. *Journal of Chemical Physics* **2002,** *116* (3), 1128-1136.

37. Chuang, S. S. C.; Tan, C. D., Mechanistic studies of the NO-CO reaction on Rh/Al2O3 under net-oxidizing conditions. *Journal of Catalysis* **1998,** *173* (1), 95-104.
38. Gustafson, J., Westerstrom, R., Resta, A., Mikkelsen, A., Andersen, J.N., Balmes, O., Torrelles, X., Schmid, M., Varga, P., Hammer, B., Kresse, G., Baddeley, C.J., Lundgren, E., Structure and catalytic reactivity of Rh oxides. *Catalysis Today* **2009**.

Chapter 8. Rh Thin-Film Nanocatalysts as Chemical Sensors – The Hot Electron Effect

Ultra-thin film 5 nm Rh/TiO_x and Rh/GaN catalytic metal-semiconductor Schottky nanodiodes were fabricated using DC Magnetron Reactive Sputtering, Rapid Thermal Annealing, and Electron Beam Evaporation. The diode barrier heights were characterized in different gas mixtures using Current-Voltage measurement and Thermionic Emission theory. Barrier heights were found to vary with the local gas composition for Rh/TiO_x nanodiodes, but did not vary with gas composition for Rh/GaN nanodiodes. The nanodiodes were also studied during the oxidation of CO by O_2 and during the oxidation of CO by NO using chemicurrent measurements and gas chromatography. Hot electron chemicurrent was determined from the current *in situ* during reaction and the thermoelectric current measured in oxidizing conditions. Similar activation energies were measured from both chemicurrent and gas chromatography, which indicates a correlation between hot electron chemicurrent and catalytic activity.

8.1. Introduction

In the 1970s and 1980s, experimental[1] and theoretical[2, 3] work by Kasemo and Norskov, respectively, demonstrated that energy released from exothermic chemi- and physisorption processes is not necessarily directly dissipated through phonon modes. Kasemo showed that Cl_2 adsorption on Na can generate photons and electrons via either surface chemiluminescence or exoelectron emission. In these processes, a newly formed reaction product relaxes through the decay of an excited electronic state to the ground state rather than through phonon modes. This can cause either the emission of the excited electron into the vacuum via exoelectron emission or the generation of a photon with energy $h\upsilon$ equivalent to the electronic relaxation energy, which is known as surface chemiluminescence[4]. In order for exoelectron emission to take place, the electron must have energy greater than the workfunction of the metal. Metal workfunctions are of the order of 3-5.5 eV. Either or both of these processes have now been shown to occur in a range of reactions involving the adsorption of a very electronegative atom or molecule, such as Cl_2 or O_2, onto a very electropositive metal with a low work function, such as Na, Mg, or K[5].

Nienhaus et al. demonstrated a new approach to the study of electronic excitations from chemical adsorption by pioneering the use of thin film metal-semiconductor Schotty diodes for the detection of hot electrons. In the first published work using this approach, Ag and Cu were evaporated on both n-type and p-type Si(111) to form Schottky diodes[6]. These diodes were able to detect the adsorption of atomic hydrogen and deuterium on the metal surfaces as currents with transient magnitudes as high as 700 pA for atomic fluxes of the order of 10^{12} atoms cm^{-2} sec^{-1} prior to saturation of the surface, which occurred gradually over the course of 30-60 minutes[6]. These hot electron-induced currents are now known as *chemicurrent*. This work was the first to directly demonstrate adsorption-induced nonadiabatic energy dissipation at transition metal surfaces.

The key innovation in Nienhaus et al.'s work was that the current was generated by the ballistic transport emission of excited, or hot, electrons over the metal-semiconductor Schottky barrier rather than into the vacuum. Whereas exoelectron emission into the vacuum requires a hot electron energy, and consequently an exothermic adsorption energy, larger than the metal workfunction, this new approach instead only requires that the hot electron have energy greater than the Schottky barrier and that the thickness of the metal between the surface where hot

electrons are generated and the metal-semiconductor interface be less than the mean free path of the hot electron through the metal, which is typically about 10 nm for a hot electron with energy 2 eV above the Fermi level with a lifetime on the order of 10 fs[7].

The next major innovation in this field was by Ji and Somorjai. Ji et al. used Pt/TiO_2[8] and Pt/GaN[9] metal-semiconductor Schottky diodes, referred to as nanodiodes, to detect hot electrons generated by catalytic CO oxidation, an exothermic catalytic reaction. In the absence of deactivation and at temperatures high enough for significant turnover, reactants continually adsorb on the catalytic metal surface. In this way, the measured chemicurrent is not limited by eventual surface saturation over time. Many catalytic reactions are also highly exothermic, which makes them promising candidates for hot electron generation. Park and Renzas, et al. later further extended this approach to the detection of hot electrons on nanoparticle surfaces using Pt nanoparticles deposited on Au/TiO_2 diodes[10]. Very recently, the catalytic nanodiode approach was used independently by two different groups to successfully detect hot electrons generated by the hydrogen oxidation reaction[11, 12]. There has also been a tremendous amount of recent theoretical work on these systems because of their implications regarding the validity of the Born-Oppenheimer Approximation with respect to reactions on metal surfaces and non-adiabatic systems in general[13-19].

In this work, we present both the first detection of hot electrons generated from CO oxidation by oxygen on a Rh nanodiode surface and the first detection of hot electrons generated from the oxidation of CO by NO. The effect of the local chemical environment on the nanodiode Schottky barrier height is determined and a clear difference is demonstrated between the current measured in reaction and the thermoelectric current measured with the same barrier height. Correlation between hot electron flux and reaction turnover rate is shown, and results are compared to previous work on Pt-based catalytic nanodiodes.

8.2. Experimental Details

8.2.1. Fabrication of Rh/TiO_x Nanodiodes

The design of the TiO_x catalytic nanodiodes used in this work is similar to that described in Chapter 2 and is also shown in Figure 8.1. First, p-type (100) silicon wafers with 500 nm thermally grown silicon oxide were cleaned with a standard piranha etch. Then, a 4 x 4 mm^2, 150 nm titanium oxide film was deposited onto the wafer using reactive direct current magnetron sputtering through an aluminum shadow mask. The wafer was then subjected to Rapid Thermal Annealing at 350°C in oxygen for 5 minutes to improve TiO_x crystallinity and oxygen content. Ohmic contacts consisted of 10 nm Ti and 75 nm Au thin films deposited using an electron beam evaporator. Finally, a catalytic 5 nm Rhodium thin film was deposited to form the Schottky interface. All film thicknesses were determined during evaporation using a calibrated quartz crystal microbalance.

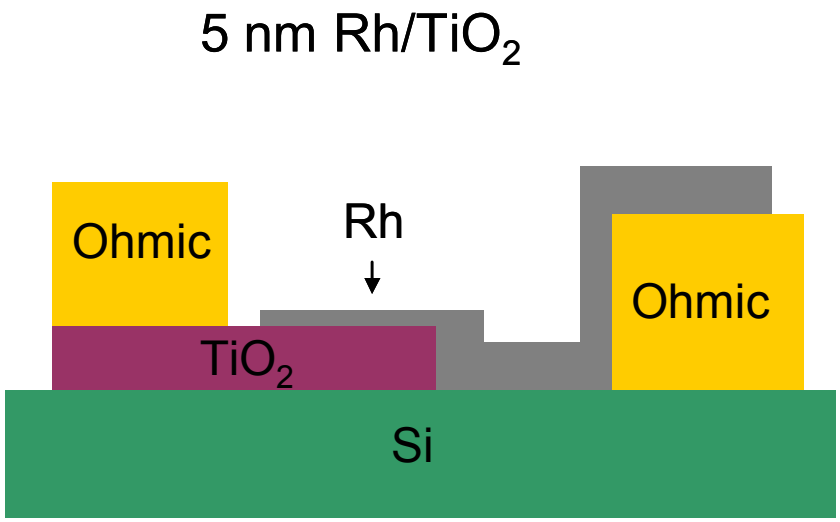

Figure 8.1 Schematic detailing design of Rh/TiO_x catalytic nanodiode. A thick Rh layer (30 nm) is used over the TiO_2 and ohmic pad step edges to ensure electrical continuity between the ohmic pad and the Rh thin film.

8.2.2. Fabrication of Rh/GaN Nanodiodes

The design of the Rh/GaN nanodiodes is presented in the schematic in Figure 8.2. 6 m Si-doped GaN formed by MOCVD on a Sapphire substrate (TDI Inc.) were cleaned in 7:1 Buffered Oxide Etch solution and rinsed in DI water. An insulating 150 nm SiO_2 layer was deposited first just in the area used by the contact pad between Rh and the chamber's current measurement wires so as to ensure that current flow was through the Rh Schottky contact. Ohmic contacts were defined by depositing 30 nm Ti and 125 nm Al using electron beam evaporation through an aluminum metal shadow mask. The ohmic structures were then heated to 800°C in nitrogen for 1 minute using Rapid Thermal Annealing. A 30 nm Rh layer was then deposited on the ohmic pad and overlapping onto the GaN surface. Lastly, a thin 5 nm Rh layer was deposited directly on the GaN surface, partially overlapping the 30 nm Rh layer. The 5 nm Rh layer serves as the primary detector for hot electrons, whereas the 30 nm Rh layer is used as a contact pad to avoid damaging the delicate 5 nm layer. All film thicknesses were determined during evaporation using a calibrated quartz crystal microbalance.

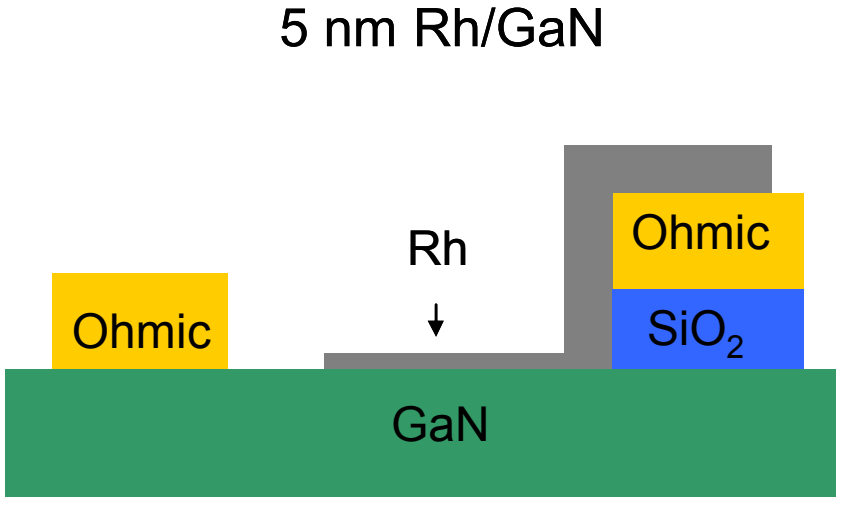

Figure 8.2 Schematic detailing design of Rh/GaN catalytic nanodiode. Rh layer is very thin (~ 5 nm) at active interface, while a thicker Rh layer is used to ensure electrical continuity between the thin film and the ohmic contact.

8.2.3. Reactor and Current Measurement Setup

All electrical and catalytic measurements were taken on the same system – a 1 L stainless steel batch reactor connected to a gas manifold, HP 5890 Series II gas chromatograph (GC), and recirculation pump. The GC uses two separate columns to measure reaction products, in a setup detailed in Section 2.1. Samples were mounted on a ceramic heater (Momentiv) with temperature measured by a type-K thermocouple at the surface of a piece of clean Si wafer on the same heater. Electrical contact was made between the device contact pads and BNC electrical feedthroughs using gold wire. Current-Voltage curves were measured with a Keithley 2400 Sourcemeter and currents were measured with a Keithley 6487 picoammeter.

8.3. Device Characterization

The catalytic nanodiodes were characterized using standard Current-Voltage (IV) curves measured at room temperature before and after every change in chemical environment. These curves were calculated using the thermionic emission equation, as described previously[20]. Schottky barrier height is very important for hot electron measurement. The barrier height must be both high enough to minimize thermoelectric current and low enough to enable transport of hot electrons into the semiconductor. In this case, the measured barrier heights are significantly lower than the adsorption energy at moderate coverage of NO, CO, and O_2 on Rh(111), which are approximately 1.3 eV[21], 1.3 eV[22], and 2.4 eV[23], respectively.

The Schottky barrier heights of the Rh/TiO_x diodes were measured to be ~0.85-0.95 eV, whereas the Rh/GaN diode barrier heights were much lower, ~0.65 eV. The lower barrier heights of the Rh/GaN diodes are likely due to local inhomogeneities in the relatively large Rh/GaN contact area. These inhomogeneities tend to lower the measured effective barrier height[24]. Figures 8.3 and 8.4 show the Schottky barrier heights measured as a function of the local gas environment for the Rh/TiO_x and Rh/GaN devices, respectively. The partial pressures of each gas are equivalent to those used during reaction, except for the CO condition on the Rh/GaN device, which was measured at 40 Torr CO, which was the partial pressure used in CO oxidation by O_2, but larger than the CO partial pressure used for the NO+CO reaction. It was found that the barrier heights in reaction conditions were very similar to barrier heights measured in only the oxidizing gas. This indicates that the reaction conditions are relatively oxidizing. As a result, the thermoelectric current in reaction was assumed to be the same as in the corresponding oxidizing condition.

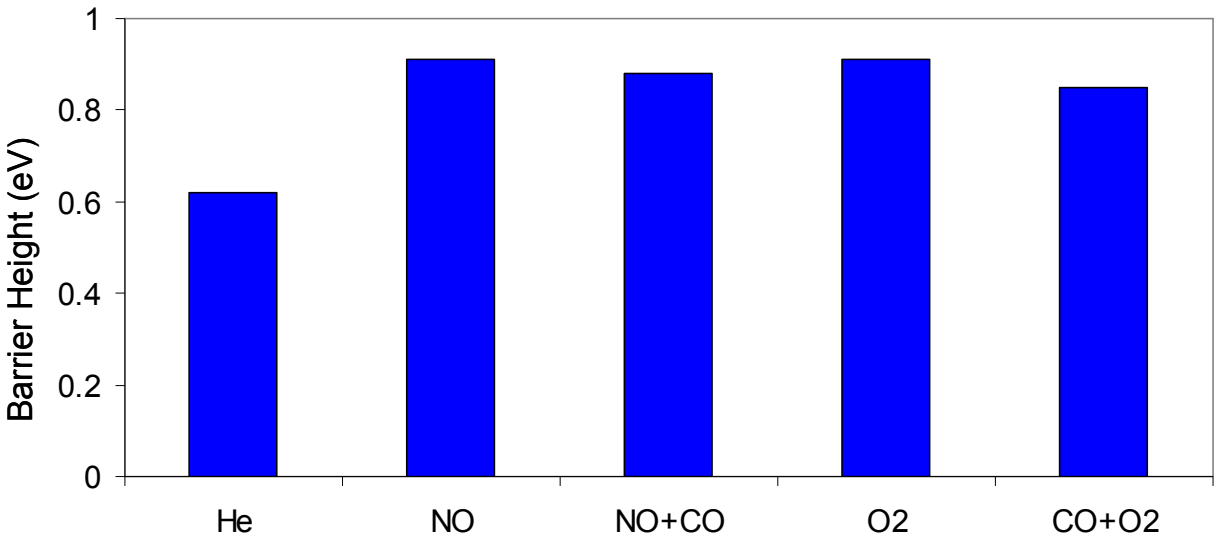

Figure 8.3 Change of Rh/TiO_x Nanodiode Schottky Barrier Height with Local Gas Environment. The barrier height is lower in reducing conditions, such as after heating in He, and higher in oxidizing conditions.

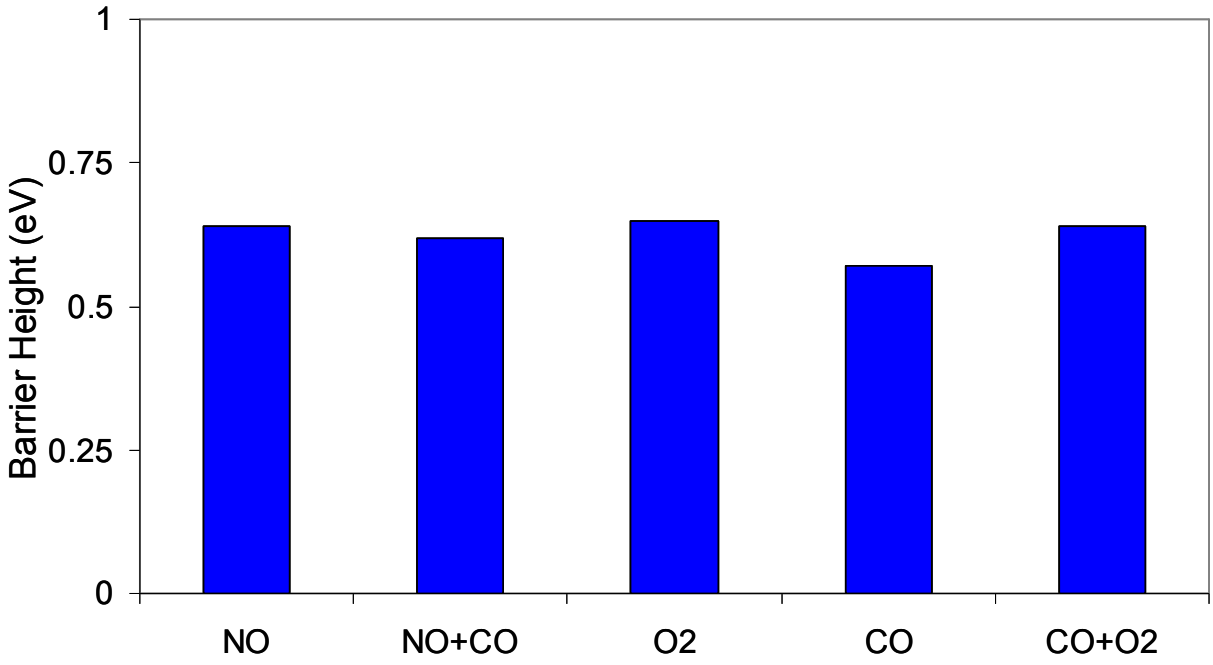

Figure 8.4 Change of Rh/GaN Nanodiode Schottky Barrier Height with Local Gas Environment.

Chemicurrent was measured as the difference between the thermoelectric current and the current in reaction, as shown for the Rh/TiO_x catalytic nanodiode in the $CO+O_2$ reaction in Figure 8.5. Thermoelectric current was measured in a mixture of He and the oxidizing gas of the reaction. This improved device stability, particularly for the TiO_x-based devices. This approach is similar to that which was used to study the hydrogen oxidation reaction on Pt/TiO_x nanodiodes[11]. As expected, the extra current due to hot electrons is in the negative direction, which is the direction of in which electrons are being transported from the metal to the semiconductor.

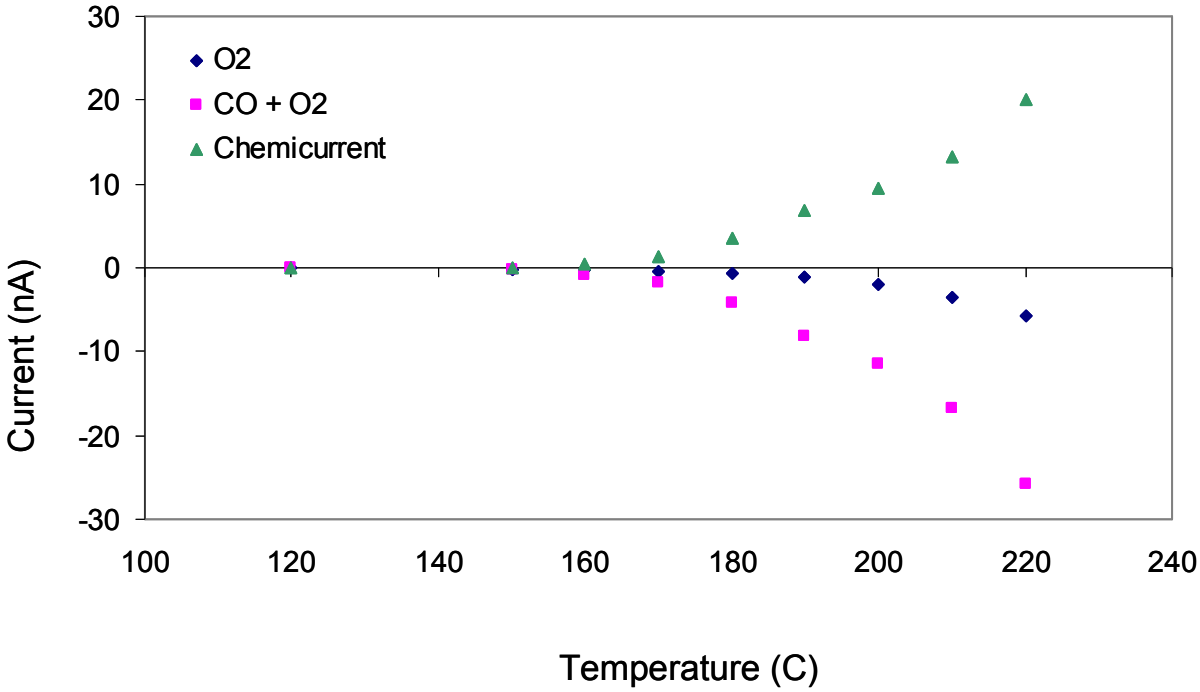

Figure 8.5 Current versus Temperature as measured on Rh/TiO_x nanodiode in O_2, during the $CO+O_2$ reaction, and as chemicurrent, which is the difference between the current in O_2 and in reaction at a given temperature.

8.4. CO Oxidation Results

8.4.1. Rh/TiO_x Nanodiode

The Rh/TiO_x catalytic nanodiodes were run from 160-190°C in 20 Torr CO, 100 Torr O_2, and 640 Torr He. The temperature range was chosen because very little chemicurrent was detected at lower temperatures and the reaction turnover was too high to measure accurately in our setup at higher temperatures. Turnover frequency (TOF) is the production of CO_2 molecules per site per second. Turnover frequency and chemicurrent for the oxidation of CO by O_2 on the Rh/TiO_x nanodiode are shown in Figure 8.6. The turnover frequency of the Rh/TiO_2 diodes was 32.2 molec. $site^{-1}$ sec^{-1} at 190°C. Activation energy, as calculated from these GC measurements, was 35.8 kcal/mol. The chemicurrent measurements are reported as the difference in the thermoelectric current measured in a non-reactive environment and in reaction, and activation energy can be calculated from these measurements as well. Both of these calculations are done in the same manner as in previous reports[9, 20]. In this case, the measured chemicurrent at 190°C was 6.9 nA, and the activation energy, as calculated from these chemicurrent measurements, was 34.5 kcal/mol, which is remarkably similar to the activation energy calculated from GC measurements. The chemicurrent yield, defined as the number of measured electrons per reaction event in the 5 nm Rh thin film region, was 8.2×10^{-6} hot electrons/event at 190°C.

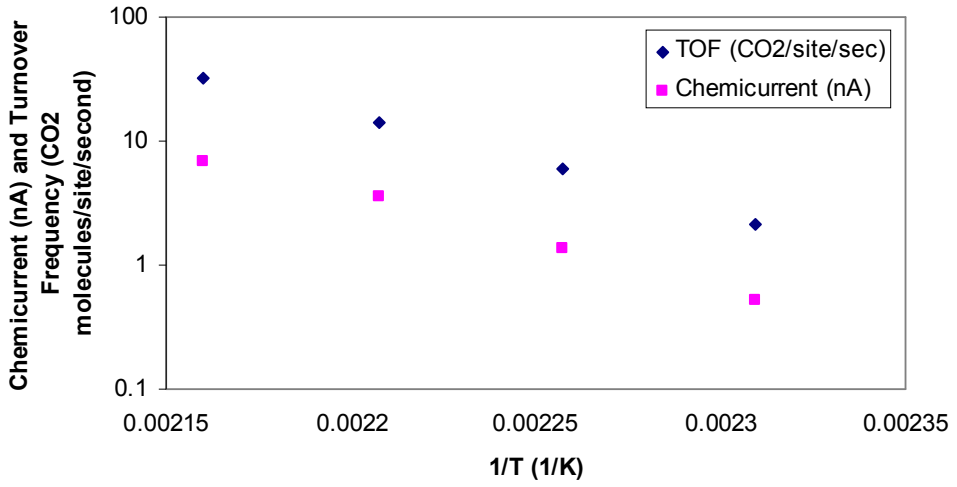

Figure 8.6 Log plot comparing chemicurrent and turnover frequency versus temperature for the Rh/TiO_x catalytic nanodiode during CO oxidation by O_2.

8.4.2. Rh/GaN Nanodiode

5 nm Rh/GaN catalytic nanodiodes were run in 40 Torr CO, 100 Torr O_2, and 620 Torr He from 180-220°C. Turnover frequency and chemicurrent for the oxidation of CO by O_2 on the Rh/GaN nanodiode are shown in Figure 8.7. TOF at 220°C was 102.2 molec. $site^{-1}$ sec^{-1} and the chemicurrent was 36.9 nA. The activation energy calculated from GC measurements was 34.9 kcal/mol, whereas the activation energy calculated from chemicurrent was 27.7 kcal/mol. The chemicurrent yield at 220°C was 1.2 x 10^{-5} electrons/event.

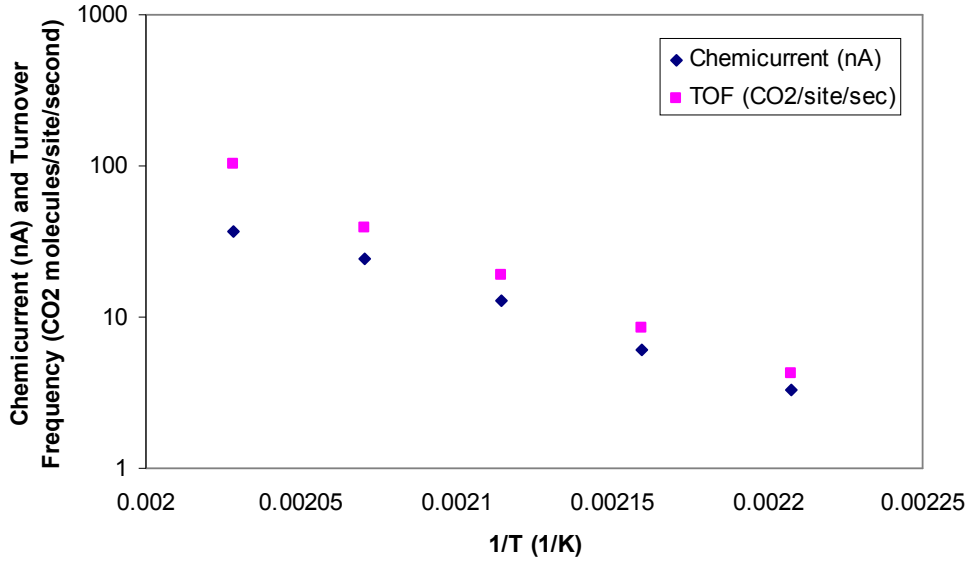

Figure 8.7 Log plot comparing chemicurrent and turnover frequency versus temperature for the Rh/GaN catalytic nanodiode during CO oxidation by O_2.

8.5. NO/CO Results

8.5.1. Rh/TiO_x Nanodiode

The NO+CO reaction was carried out in 8 Torr NO, 8 Torr CO, and 744 Torr He on 5 nm Rh/TiO_x catalytic nanodiodes. GC and chemicurrent measurements were taken from 190-220°C, and are presented in Figure 8.8. At 220°C, the measured TOF, calculated as the production of CO_2, was 0.54 molec. $site^{-1}$ sec^{-1}, and the measured chemicurrent was 7.9 nA. The activation energies were 26.1 and 25.4 kcal/mol as calculated from GC and chemicurrent, respectively, and the chemicurrent yield at 220°C was 5.5 x 10^{-4} electrons/event.

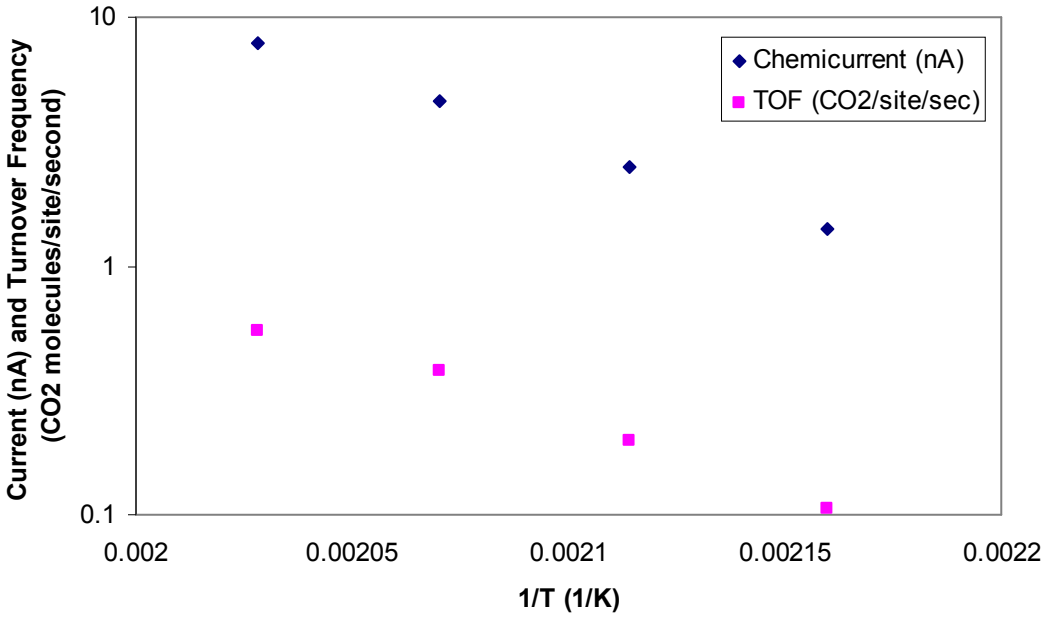

Figure 8.8 Log plot comparing chemicurrent and turnover frequency versus temperature for the Rh/TiO_x catalytic nanodiode during CO oxidation by NO.

8.5.2. Rh/GaN Nanodiode

Rh/GaN catalytic nanodiodes were run in 8 Torr NO, 8 torr CO, and 744 Torr He from 200 - 250°C. Arrhenius plots of GC and chemicurrent data are presented in Figure 8.9. TOF of CO_2 at 220°C was 2.13 molec. $site^{-1}$ sec^{-1}, and chemicurrent was 17.9 nA. Activation energies were 32.8 and 31.7 kcal/mol as calculated from GC and chemicurrent measurements, respectively. The chemicurrent yield was 2.8 x 10^{-4} electrons/event at 220°C.

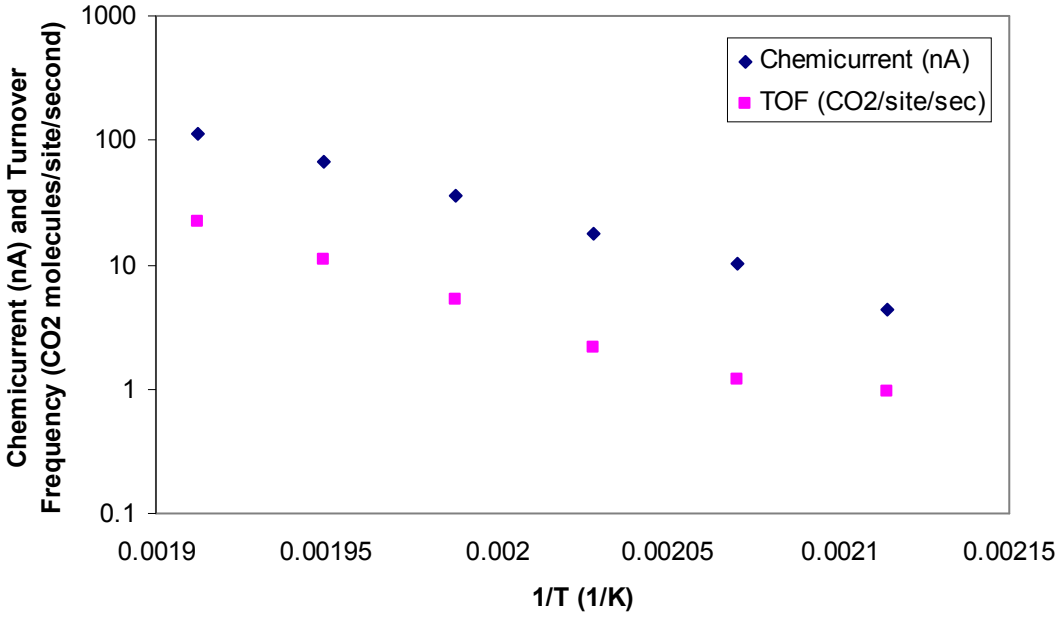

Figure 8.9 Log plot comparing chemicurrent and turnover frequency versus temperature for the Rh/GaN catalytic nanodiode during CO oxidation by NO.

8.6. Discussion

Turnover frequency and chemicurrent have been measured on Rh thin film TiO_x and GaN devices in both the CO oxidation and NO/CO reactions. TiO_x-supported Rh thin film nanodiodes demonstrated higher turnover and similar chemicurrent yield as compared to the GaN-supported nanodiodes. Chemicurrent yield was higher for the NO/CO reaction. There was also a clear correlation between the activation energy measured from chemicurrent and traditional GC measurements for both reactions on both devices. This correlation implies a direct relationship between the reaction on the surface and hot electron production and transport across the Schottky barrier, as has been demonstrated previously on Pt-based TiO_x and GaN nanodiodes[11, 20, 25]. The activation energy for the CO oxidation reaction is higher on the Rh-based diodes than was measured on the Pt-based nanodiodes[20], as is expected based on single-crystal studies, from which Rh(111) is known to have a higher activation energy than Pt(111) for this reaction[26]. Although the role of Rh thin film thickness in chemicurrent yield has not been studied here, previous work by Ji et al. showed a significant decrease in chemicurrent yield with increasing metal thickness[27].

Although the Schottky barrier height always increased when O_2 and NO gases were added to the chamber and decreased when CO was added or the device was heated in He, the change in barrier height between reaction conditions and the oxidizing thermoelectric condition was minimal, especially for the GaN-based devices, as shown in Figure 8.4. This difference in device stability dictated the use of only 20 Torr CO in the Rh/TiO_2 CO oxidation experiment, as opposed to the 40 Torr CO used with the GaN devices. In reducing conditions, the effect of these barrier height changes on thermoelectric current was significant enough to interfere with chemicurrent measurement.

A large decrease in the otherwise-consistent chemicurrent yield measurements typically occurred at high temperature. This effect dictated the upper limit of the temperature range available for chemicurrent measurement on each device. The lower limit of the temperature range was determined by GC sensitivity. There are many possible reasons for the change in yield, including current saturation or barrier height change due to oxidation-state dependent changes in the workfunction of the Rh thin film[28], adsorbate-induced changes in the metal workfunction[29], interfacial effects at the metal-semiconductor interface (especially in GaN)[30], and, particularly in the case of the TiO_x-based devices, oxidation and reduction of the supporting semiconductor[31]. In spite of this, it is notable that the reaction rate and chemicurrent remain proportional at low temperatures for both the TiO_x and GaN-based catalytic nanodiodes in both CO oxidation and the NO/CO reaction. This indicates that there is a relationship between hot electron chemicurrent measured on the catalytic nanodiode and the activity of the catalyst in reaction.

	Rh/TiO_x in CO/O_2 (20 Torr CO/100 Torr O_2)	Rh/GaN in CO/O_2 (40 Torr CO/100 Torr O_2)	Rh/TiO_x in NO/CO (8 Torr NO/8 Torr CO)	Rh/GaN in NO/CO (8 Torr NO/8 Torr CO)
Chemicurrent (nA)	6.9 at 190°C	36.9 at 220°C	7.9 at 220°C	17.9 at 220°C
TOF (CO_2/site/sec)	32.2 at 190°C	102.2 at 220°C	0.54 at 220°C	2.13 at 220°C
E_a from Chemicurrent (kcal/mol)	34.5	27.7	25.4	31.7
E_a from TOF (kcal/mol)	35.8	34.9	26.1	32.8
Yield (hot electrons/ event)	8.2 x 10-6 at 190°C	1.2 x 10-5 at 220°C	5.5 x 10-4 at 220°C	2.8 x 10-4 at 220°C

Table 8.1 Summary of results on each type of device in both the CO/O_2 reaction and the NO/CO reaction.

It is notable that the measured hot electron yields are much higher in the NO/CO reaction than in the CO/O_2 reaction (Table 8.1). This discrepancy may indicate that there may be a mechanistic difference in the manner in which hot electrons are generated in these two reactions. There is also no clear trend in activation energies for each sample in the two reactions. This finding implies that the metal-support interaction may play an important role in determining reaction kinetics in catalytic nanodiodes, perhaps in part because of the very small metal film thicknesses used in these devices.

8.7. Conclusions

Chemicurrent proportional to the catalytic reaction turnover rate has been successfully measured on Rh thin film nanodiodes for the first time. Hot electron current was also measured in the oxidation of CO by NO for the first time. Chemicurrent was found to be strongly correlated to catalytic turnover frequency for both Rh/TiO_x and Rh/GaN devices in both the CO + O_2 reaction and the NO + CO reaction. The measurement of thermoelectric current in oxidizing conditions to account for an apparent change in barrier height in reducing conditions was also successfully demonstrated in this work as an appropriate extension of the technique used previously in hydrogen oxidation studies. It was found that, as in studies on Pt, the chemicurrent yield was higher for GaN-based devices than for TiO_x-based devices for the oxidation of CO by oxygen. In the reaction of NO with CO, however, the chemicurrent yield was found to be higher for TiO_x devices, which indicates that semiconductor crystallinity and surface roughness are not the only factors in determining chemicurrent yield, as had been previously thought. The extension of the hot electron chemicurrent measurement technique using catalytic nanodiodes to the Rh and the NO + CO system is an important step towards the understanding of the role of hot electrons in catalysis and of the degree to which these effects apply to a wide range of catalytic systems.

8.8. References

1. Kasemo, B.; Walldén, L., Spontaneous emission of photons and electrons during chemisorption of chlorine on sodium. *Solid State Communications* **1974,** *15* (3), 571-574.
2. Nørskov, J. K.; Newns, D. M.; Lundqvist, B. I., Molecular orbital description of surface chemiluminescence. *Surf. Sci.* **1979,** *80*, 179-188.
3. Norskov, J. K., Dynamical aspects of electronic structure during adsorption. *Journal of Vacuum Science and Technology* **1981,** *18* (2), 420-426.
4. Nienhaus, H., Electronic excitations by chemical reactions on metal surfaces. *Surface Science Reports* **2002,** *45* (1-2), 3-78.
5. Nienhaus, H.; Gergen, B.; Weinberg, W. H.; McFarland, E. W., Detection of chemically induced hot charge carriers with ultrathin metal film Schottky contacts. *Surf. Sci.* **2002,** *514* (1-3), 172-181.
6. Nienhaus, H.; Bergh, H. S.; Gergen, B.; Majumdar, A.; Weinberg, W. H.; McFarland, E. W., Electron-hole pair creation at Ag and Cu surfaces by adsorption of atomic hydrogen and deuterium. *Physical Review Letters* **1999,** *82* (2), 446-449.
7. Campillo, I.; Silkin, V. M.; Pitarke, J. M.; Chulkov, E. V.; Rubio, A.; Echenique, P. M., First-principles calculations of hot-electron lifetimes in metals. *Physical Review B* **2000,** *61* (20), 13484-13492.
8. Ji, X. Z.; Zuppero, A.; Gidwani, J. M.; Somorjai, G. A., The catalytic nanodiode: Gas phase catalytic reaction generated electron flow using nanoscale platinum titanium oxide Schottky diodes. *Nano Lett.* **2005,** *5* (4), 753-756.
9. Ji, X. Z.; Zuppero, A.; Gidwani, J. M.; Somorjai, G. A., Electron flow generated by gas phase exothermic catalytic reactions using a platinum-gallium nitride nanodiode. *Journal of the American Chemical Society* **2005,** *127* (16), 5792-5793.

10. Park, J. Y.; Lee, H.; Renzas, J. R.; Zhang, Y. W.; Somorjai, G. A., Probing hot electron flow generated on Pt nanoparticles with Au/TiO2 Schottky diodes during catalytic CO oxidation. *Nano Lett.* **2008,** *8* (8), 2388-2392.
11. Hervier, A.; Renzas, J. R.; Park, J. Y.; Somorjai, G. A., Hydrogen Oxidation-Driven Hot Electron Flow Detected by Catalytic Nanodiodes. *Nano Lett.* **2009,** *9* (11), 3930-3933.
12. Karpov, E. G.; Nedrygailov, II, Solid-state electric generator based on chemically induced internal electron emission in metal-semiconductor heterojunction nanostructures. *Applied Physics Letters* **2009,** *94* (21).
13. Shenvi, N.; Roy, S.; Tully, J. C., Nonadiabatic dynamics at metal surfaces: Independent-electron surface hopping. *Journal of Chemical Physics* **2009,** *130* (17).
14. Wodtke, A. M.; Tully, J. C.; Auerbach, D. J., Electronically non-adiabatic interactions of molecules at metal surfaces: Can we trust the Born-Oppenheimer approximation for surface chemistry? *International Reviews in Physical Chemistry* **2004,** *23* (4), 513-539.
15. Maximoff, S. N.; Head-Gordon, M. P., Chemistry of fast electrons. *Proceedings of the National Academy of Sciences of the United States of America* **2009,** *106* (28), 11460-11465.
16. Trail, J. R.; Bird, D. M.; Persson, M.; Holloway, S., Electron-hole pair creation by atoms incident on a metal surface. *Journal of Chemical Physics* **2003,** *119* (8), 4539-4549.
17. Trail, J. R.; Graham, M. C.; Bird, D. M.; Persson, M.; Holloway, S., Energy loss of atoms at metal surfaces due to electron-hole pair excitations: First-principles theory of "chemicurrents". *Physical Review Letters* **2002,** *88* (16).
18. Gadzuk, J. W., On the detection of chemically-induced hot electrons in surface processes: from X-ray edges to schottky barriers. *J. Phys. Chem. B* **2002,** *106* (33), 8265-8270.
19. Kharlamov, F. V.; Kharlamov, V. F., Transmission of hot electrons through a metal-semiconductor interface. *Semiconductors* **2009,** *43* (1), 42-46.
20. Park, J. Y.; Renzas, J. R.; Hsu, B. B.; Somorjai, G. A., Interfacial and Chemical Properties of Pt/TiO2, Pd/TiO2, and Pt/GaN Catalytic Nanodiodes Influencing Hot Electron Flow. *The Journal of Physical Chemistry C* **2007,** *111* (42), 15331-15336.
21. Loffreda, D.; Simon, D.; Sautet, P., Molecular and dissociative chemisorption of NO on palladium and rhodium (100) and (111) surfaces: A density-functional periodic study. *Journal of Chemical Physics* **1998,** *108* (15), 6447-6457.
22. Nieuwenhuys, B. E., ADSORPTION AND REACTIONS OF CO, NO, H-2, AND O2 ON GROUP-VIII METAL-SURFACES. *Surf. Sci.* **1983,** *126* (1-3), 307-336.
23. Peterlinz, K. A.; Sibener, S. J., Absorption, Adsorption, and Desorption Studies of the Oxygen/Rh(111) System Using O2, NO, and NO2. *The Journal of Physical Chemistry* **1995,** *99* (9), 2817-2825.
24. Chand, S.; Kumar, J., Simulation and analysis of the I - V characteristics of a Schottky diode containing barrier inhomogeneities. *Semiconductor Science and Technology* **1997,** (7), 899.
25. Park, J. Y.; Renzas, J. R.; Contreras, A. M.; Somorjai, G. A., The genesis and importance of oxide-metal interface controlled heterogeneous catalysis; the catalytic nanodiode. *Topics in Catalysis* **2007,** *46* (1-2), 217-222.
26. Nakao, K.; Watanabe, O.; Sasaki, T.; Ito, S.-i.; Tomishige, K.; Kunimori, K., CO oxidation on Pd(1 1 1), Pt(1 1 1), and Rh(1 1 1) surfaces studied by infrared chemiluminescence spectroscopy. *Surf. Sci.* **2007,** *601* (18), 3796-3800.

27. Ji, X. Z.; Somorjai, G. A., Continuous hot electron generation in Pt/TiO2, Pd/TiO2, and Pt/GaN catalytic nanodiodes from oxidation of carbon monoxide. *J. Phys. Chem. B* **2005,** *109* (47), 22530-22535.
28. Kim, S. Y.; Baik, J. M.; Yu, H. K.; Kim, K. Y.; Tak, Y.-H.; Lee, J.-L., Rhodium-oxide-coated indium tin oxide for enhancement of hole injection in organic light emitting diodes. *Applied Physics Letters* **2005,** *87* (7), 072105-3.
29. Ho, P.; White, J. M., Adsorption of NO on Rh(100). *Surf. Sci.* **1984,** *137* (1), 103-116.
30. Cao, X. A.; Pearton, S. J.; Dang, G.; Zhang, A. P.; Ren, F.; Van Hove, J. M., Effects of interfacial oxides on Schottky barrier contacts to n- and p-type GaN. *Applied Physics Letters* **1999,** *75* (26), 4130-4132.
31. Walton, R. M.; Dwyer, D. J.; Schwank, J. W.; Gland, J. L., Gas sensing based on surface oxidation/reduction of platinum-titania thin films I. Sensing film activation and characterization. *Appl. Surf. Sci.* **1998,** *125* (2), 187-198.